University of New Mexico
UNM Digital Repository

Optical Science and Engineering ETDs | Engineering ETDs

6-26-2015

Pulsed laser induced breakdown in solid state materials and air

Zhanliang Sun

Follow this and additional works at: https://digitalrepository.unm.edu/ose_etds

Recommended Citation
Sun, Zhanliang. "Pulsed laser induced breakdown in solid state materials and air." (2015). https://digitalrepository.unm.edu/ose_etds/41

This Dissertation is brought to you for free and open access by the Engineering ETDs at UNM Digital Repository. It has been accepted for inclusion in Optical Science and Engineering ETDs by an authorized administrator of UNM Digital Repository. For more information, please contact disc@unm.edu.

Zhanliang Sun

Candidate

Optical Science and Engineering - Physics

Department

This dissertation is approved, and it is acceptable in quality and form for publication:

Approved by the Dissertation Committee:

Wolfgang Rudolph, Chair

Francisco Elohim Becerra Chavez

Paul Schwoebel

David Cremers

Pulsed laser induced breakdown in solid state materials and air

by

Zhanliang Sun

B.S., Applied Physics, Harbin University of Sci. & Technology, 2002
M.S., Optics, Tsinghua University, 2006
M.S., Optical Sci. & Engineering, University of New Mexico, 2010

DISSERTATION

Submitted in Partial Fulfillment of the
Requirements for the Degree of

Doctor of Philosophy
Optical Science and Engineering

The University of New Mexico

Albuquerque, New Mexico

May, 2015

©2015, Zhanliang Sun

Dedication

To my Lord, Christ Jesus, for His encouragement and comfort.

No discipline seems pleasant at the time, but painful.
Later on, however, it produces a harvest of righteousness
and peace for those who have been trained by it.
– Hebrews 12: 11

Let us not become weary in doing good,
for at the proper time we will reap a harvest
if we do not give up.
– Galatians 6: 9

Acknowledgments

I would like to thank my advisor, Professor Wolfgang Rudolph, for his support, guidance and patience.

I am thankful to my dissertation committee members: Dr. Francisco Elohim Becerra Chavez, Dr. Paul Schwoebel and Dr. David Cremers.

I would also like to thank Dr. Luke Emmert, who kindly support me through this journey. Many thanks to Dr. Jinhai Chen and Dr. Zhenwei Wang. From them, I learned a lot of experimental skills. I want to thank Prof. Detlev Ristau (Laser Zentrum Hannover e.V., Hannover, Germany) and Prof. Carmen S. Menoni (Colorado State University, Fort Collins, CO, USA) and their respective groups for the high-quality samples. Many thanks to our research projects collaborators, Dr. David Cremers (Applied Research Associates, Inc. Albuquerque, NM, USA) and Dr. Matthias Lenzner (Lenzner Research LLC, Tucson, AZ, USA).

Thanks to the rest of our group for helpful discussion: Vasudevan Nampoothiri, Mark Mero, Duy Nguyen, Reed Weber, Cristina Rodriguez, Xuerong Zhang, Ben Oliker, Behshad Roshanzadeh, Yejia Xu, Ahmad Mansoori.

I am grateful for my wife, Lucy Cheng, for her support. Also, gratitude to my parents, for their encouragement for my graduate study abroad.

Pulsed laser induced breakdown in solid state materials and air

by

Zhanliang Sun

B.S., Applied Physics, Harbin University of Sci. & Technology, 2002

M.S., Optics, Tsinghua University, 2006

M.S., Optical Sci. & Engineering, University of New Mexico, 2010

Ph.D., Optical Sci. & Engineering, University of New Mexico, 2015

Abstract

Laser induced breakdown is important in applications ranging from laser machining to laser induced breakdown spectroscopy to laser induced damage.

Laser induced breakdown in dielectric materials results from a combination of multiphoton absorption (MPA), tunneling and avalanche ionization. Aspects of these processes have been studied through measurements of the laser induced damage threshold (LIDT) and its dependence on pulse duration, polarization and wavelength. At long pulse durations ($>$ 1 ns), relaxation of conduction band electrons during the pulse is responsible for the increased LIDT compared to scaling derived from sub-picosecond pulses. Linear polarization produces lower LIDT than circular polarization for MPA order of $m = 3$ and 4 with femtosecond and picosecond pulses. Laser damage tests with two-color pulse pairs show that the damage threshold depends on the order of the pulse pair. The measured difference between single-pulse

and multiple-pulse MPA of sapphire and fused silica coefficients was explained with the creation of laser induced defects.

Measurements of damage and ablation thresholds of dielectrics and metals for different numbers of pulses show the effect of laser induced material modifications, also called material incubation. A phenomenological incubation model based on changes of (i) absorption coefficient and (ii) critical energy is introduced and successfully explained the dependence of the ablation threshold on the number of pulses for metals and dielectrics.

We explore LIDTs of bulk metals using the plasma emission method. Nickel alloy shows good agreement between the crater size method and the plasma emission method.

The transient electron temperature in a femtosecond air plasma (filament) was determined from absorption and optical diffraction experiments. The electron temperature and plasma density decay on similar time scales of a few hundred picoseconds. Comparison with plasma theory reveals the importance of inelastic collisions that lead to energy transfer to vibrational degrees of freedom of air molecules during the plasma cooling.

Contents

List of Figures

List of Tables

List of Tables

Glossary

AOI	angle of incidence
ASE	amplified stimulation emmission
BDS	Boulder Damage Symposium
CB	conduction band
CPA	chirped pulse amplification
cw	continuous wave
EBE	electron beam evaporation
F_{th}	damage or ablation threshold fluence
FROG	frequency-resolved optical gating
fs	femtosecond ($= 1 \times 10^{-15}$ sec)
FWHM	full width at half maximum
HWP	half-wave plate
IBS	ion beam sputtering
IR	infrared

LG	Laguerre-Gaussian
LIB	laser induced breakdown
LID	laser induced damage
LIDT	laser induced damage threshold
LIPSS	laser induced periodic surface structures
MPA	multiphoton absorption
MPI	multiphoton ionization
ms	nanosecond ($= 1 \times 10^{-3}$ sec)
ns	nanosecond ($= 1 \times 10^{-9}$ sec)
PD	photodiode
PLD	pulsed-laser deposition
PMT	photon multiplier tube
ps	picosecond ($= 1 \times 10^{-12}$ sec)
PTM	photo-thermal microscopy
QWP	quarter-wave plate
S	pulse number or number of pulses
sec	second
SEM	scanning electron microscope
SH	second harmonic

TH	third harmonic
THGU	third harmonic generation unit
THz	terahertz ($= 1 \times 10^{12}$ Hz)
UV	ultroviolet
VB	valence band
ZTD	zero time delay

Chapter 1

Introduction

1.1 Research background and motivation

This dissertation deals with the interaction of laser pulses with solids and gaseous media near and above the threshold for laser induced breakdown.

Since the discovery of lasers in the 1960s, laser induced breakdown (LIB) has become an important research topic. LIB can happen in different kind of media– solid, liquid or gas. In solid media, LIB can lead to a modification of the material properties, to material damage, ie. laser induced damage (LID), or even to complete material removal, ie. laser induced ablation. In gas media, with high power lasers, LIB can lead to a production of plasmas.

The first reports of bulk laser induced breakdown or damage were by Bruma [1] and Hercher [2] in papers at the 1964 spring meeting of the Optical Society of America. Some papers on LID came out later in that year [3,4]. The principal conclusions of these initial reports are as follows [5]: (1) Linear absorption plays no major role in the failure of the illuminated materials. (2) The damage process is highly nonlinear.

(3) Electron avalanche breakdown may be initiated by defects and/or impurities. (4) The LID threshold and morphology depend on beam spot size for a given energy density. LID quickly became an important area in the study of laser-matter interactions. Even after 50 years, this area is still a very active field, see proceedings of the SPIE Laser Damage Conference in Boulder starting in 1970.

LID and laser ablation are closely related phenomena with importance for micro- and nano-structuring.

Laser micromachining presents several attractive features, especially when performed with ultrafast (femtosecond) lasers [6]. For transparent materials, it is a maskless technology which allows rapid device prototyping, has intrinsic three-dimensional capabilities and can produce both photonic and microfluidic devices. For these reasons it is ideally suited for the fabrication of complex microsystems with unprecedented functionalities [7]. This technology is also applied to process biological materials [8] .

Furthermore, the material ejected from a dielectric following femtosecond-laser excitation can potentially be used for thin-film deposition. The deposition rate is typically much smaller than that for nanosecond lasers, but film production by femtosecond (fs) lasers does possess several attractive features. First, the strong-field excitation makes it possible to produce films of materials that are transparent to the laser light. Second, the highly localized excitation reduces the emission of larger material particulates. Third, lasers with ultrashort pulses are shown to be particularly useful tools for the production of nanocluster films. The first film of a dielectric, ZnO, was produced by Okoshi *et al.* [9] and by Millon *et al.* [10]. Today, more than 20 dielectric materials have been deposited as thin films by femtosecond pulsed-laser deposition (PLD) [11] .

On the other hand, LID will limit the development of high power laser systems.

Year	2008	2009	2010	2011	2012	2013
Coating type	HR	HR	AR	HR	Polarizer	Polarizer
Wavelength (nm)	1064	786	355	193	1064 "P"	"S"
Reflectivity (%)	> 99.5	> 99.5	< 0.25	> 97	< 5	> 99
Incident angle (°)	0	0	0	0	56.4	56.4
Num. of samples	35	27	29	12	26	31
Max. F_{th} (J/cm^2)	130	1.1	50	1.9	30	43
F_{th} Max./Min.	> 100	5	60	70	6	4

Table 1.1: BDS thin film damage competition coating specifications and statistics. The last row shows the ratios of the damage thresholds between the best and the worst samples.

In 2008, a thin film damage competition was organized at the Boulder Damage Symposium (BDS). Since then, the competition was held every year with thin film optical samples contributed from different institutions (see Table 1.1). An overview for damage competition from 2008 through 2011 [12–15] can be found in Reference [16]. In each competition [16–18], it was observed that a wide range of laser induced damage thresholds (LIDT) [1] exists between the worst and best samples ranging from a factor of 4 for the 1064-nm thin film polarizer to over 100 for the 1064-nm nanosecond mirrors. Other trends were observed, such as the impact of surface preparation, coating material selection, and deposition method with often very different results observed depending on the wavelength, pulse length, and coating type of the various competitions. The large spread of the results, see last row in Table 1.1, exemplifies the need for fundamental research in this field which will ultimately give guidance to coating improvements.

The samples in our studies are high quality (dense, durable, high damage threshold) thin dielectric films. These films are normally hundred nm thick. The LID study with thin films makes the analysis simpler because of the absence of a lot of

[1] Normally, there is a threshold fluence in laser damage. Below this value, damage probability is zero. Above this value, damage probability starts to increase.

nonlinear processes, such as self-focusing and self-phase modulation, that occur in bulk materials [19].

The second topic of my dissertation is concerned with air plasmas excited by femtosecond lasers. Theses plasmas have found interesting applications as laser filaments and as objects for fundamental research related to high laser intensity-matter interactions.

In 1995, Braun *et al.* discovered an intriguing phenomenon [20]. By launching infrared pulses with femtosecond durations and gigawatt (GW) powers in the atmosphere, the beam became confined to a long-living, self-confined tube of light capable of covering several tens of meters, i.e. many linear diffraction lengths along the propagation axis [20].

The mechanism supporting this "light bullet" results from the balance between Kerr focusing, which increases the local optical index with the wave intensity and self-induced ionization (plasma) [21]. When an ultrashort pulse self-focuses and couples with a self-induced plasma channel, its spatial profile exhibits a narrow extent along the optical path. This picture classically refers to what is commonly called a femtosecond "filament". The term *filament* (or *filamentation*) here is used to describe the part of the self-guided propagation during which the pulse generates a column of weakly ionized plasma in its wake [22].

Such laser induced air plasmas aroused a great interest and became a field of intense research activity [21–23]. They have found applications that range from lighting control and triggering of discharges [24], to remote sensing [25], to few-cycle pulse generation [26, 27].

1.2 Open questions

1.2.1 Interaction of laser pulses with solids

LID is a process triggered by energy deposition into materials from lasers. For dielectrics, rate equations were used to describe such energy transfer processes. The electrons are moved from the valence band (VB) to the conduction band (CB) through nonlinear processes. There are mainly three processes, multiphoton absorption (MPA), tunneling ionization and avalanche ionization [28,29]. Damage will happen when the electron density in the CB reaches a critical value, N_{crit}. At that point, the plasma frequency coincides with the laser frequency. There is a resonance absorption of laser energy. As a result, the material is quickly damaged.

While the fundamental mechanisms leading to N_{crit} in the CB and to subsequent laser damage were identified early on [30,31], it remained a challenge to predict laser induced damage thresholds (LIDTs) of dielectric materials reliably and to identify scaling laws for ns and ps pulse induced damage.

The main reason was the unknown role that material defects played in the damage initiation and the subsequent degree of randomness [32]. Another reason was that early experimental studies did not always clearly distinguish experimentally between multiple-pulse (S-on-1) and single-pulse (1-on-1) damage. [2] This is partly true also for early fs damage studies. These two testing methodologies give different results. The threshold for S-on-1 damage is lower than the threshold for 1-on-1 damage. This effect is called incubation. It comes from the accumulation of electrons in some mid-gap states between the CB and the VB. Electrons can stay in those defects long relative to time separation between pulses. As for the defects, we differentiate

[2] A single-pulse (1-on-1) damage test requires the sample to be moved after each exposure of one pulse. In a multiple-pulse (S-on-1) damage test, the sample is exposed under S multiple laser shots with the same fluency and then is moved to the next test site.

between the native and laser induced defects.

Validity of LID model for longer pulses

The LID model using rate equations [28] has explained the 1-on-1 [33] and S-on-1 [34] results in thin films with sub-ps pulses. For longer pulses, the mid-gap defect states can be occupied and electrons can be excited from those states, like in multiple-pulse damage. The question exists whether the model is still applicable for longer pulses, such as ps and ns pulses. To answer that question, we measured LIDTs of thin films with 375 ps and 13 ns pulses. Material parameters for the defect states were modeled using rate equations. The validity of the model for these long pulses was checked.

Clarity between single-pulse and the multiple-pulse MPA coffeicients

Because of the defect states, the MPA coefficient is expected to change within a train of pulses. For fused silica, the differences between effective MPA coefficient from multiple pulses [35,36] and single pulse [37–39] measurements were not differentiated. It is important to clarify the difference between the single-pulse and the multiple-pulse MPA coffeicients. The direct measurement of MPA on hundred nm thick films is impossible because the signal is too weak. To study the effect of laser pulses on MPA, we measured the transmission through tens to hundred μm thick fused silica and sapphire plates as a function of incident intensity.

LIDTs dependence on the order of the pulse sequence

Once the electrons are excited from the VB to the CB, free carrier absorption and subsequent impact ionization can produce an avalanche like electron increase in the CB. This will quickly bring damage to the material. The relative role of avalanche

and multiphoton ionization is still not clear. In recent studies on sapphire plates, contrary conclusions were drawn [40, 41]. Using a two-color ultrashort pulse pair, we studied the LIDTs by varying the order of the pulse sequence. The results showed a dependence on the input pulse color in impact ionization.

Role of polarization in LID of thin films

An interesting aspect of MPA concerns the role of linear and circular polarization [42]. There is still no clear understanding of the role to predict the polarization dependence in LID for dielectric materials. LID tests (1-on-1) on thin dielectric films performed with 30-ps pulses 40 years ago didn't show a clear dependence on the polarization [43]. Femtosecond pulses are more likely to probe intrinsic material properties [44]. Also, the coating technology has been improved a lot to reduce the effect of impurities. It would be very helpful to measure the difference of LID between linear and circular polarization. This will provide experimental data for further theoretical exploration. We measured the polarization dependence of LIDT with fs and ps pulses on thin films using 1-on-1 and S-on-1 tests. The polarization dependence in thin films LID was presented with clear difference between linear and circular polarizations.

Characterization of LID processes using surface structures

Ripples are often observed after the interaction of solid materials with short laser pulses [45]. They can be on the material surface or at the bottom of the ablation craters. Their direction can be either parallel or perpendicular to the input polarization direction. Theoretical models have been developed to explained the formation of the ripples [46]. Typically, ripples are considered as a result of interaction between the input laser pulses and surface plasma wave [45, 47]. However, many aspects of ripple generation are still unclear [46]. By carefully examining the spots illuminated

with multiple pulses, we identified and captured several distinctive structures. The damage process was revealed by the structure change on the illuminated surface. A line structure was found before the generation of ripples. This structure provides experimental evidence of the trigger for the formation of ripples.

Verification of agreement between two LIDT measurement methods

The determination of LIDT is usually performed by inspecting the illuminated spots under a microscope or by detecting changes of the scattering pattern by a probe laser. For single pulse damage, the threshold can also be obtained from the dependence of the crater size on the incident fluence [48]. The advantage using the crater size method is that the experiment could be conducted well above the damage threshold. For multiple-pulse damage, the method using crater size to get the threshold is not a priori clear and justified. Note the incubation itself becomes radius dependent.

It is important to check whether the LIDTs obtained from these two methods are in agreement or not. To do that, we conducted LID tests on thin dielectric films with both methods.

Model of material incubation

It is well established that the critical fluence for damage, F_{th}, depends on the number S of pulses exciting one and the same spot (S-on-1 test). This phenomenon is often referred to as material incubation [49]. Different models have been used to describe this phenomenon [34, 50–52]. To cover a larger variety of materials - dielectrics, metals and possibly semiconductors – based on physical processes, we establish a phenomenological approach taking into account two major components of material incubation. This model will then be applied to assess the validity of the crater size method to determine multi-pulse thresholds $F_{th}(S)$ and to compare incubation in

metals and dielectric materials.

The surface roughness of metals does not allow the on-site scattering check for threshold measurements. Instead, the craters size method was used. We also explored methods for the determination of ablation thresholds of metals based on plasma emission.

1.2.2 Interaction of laser pulses with gaseous media

One interesting application is using air plasmas as a "wave guide" to transmit signals. A waveguide was generated with a 1.5 J femtosecond laser system [53]. It is very interesting to know whether the filaments can help guide waves or not with much lower energy (mJ) laser source. Evidence were found for enhanced backward scattering in the presence of filaments [54]. This could open doors for remote sensing applications. We explored the plasma wave guide properties. Two ideas were tested and examined: (a) backward scattering properties from a single filament and (b) wave guiding with multiple plasma channels.

Critical properties of such an air plasma/filament are the refractive index profile and its lifetime. To take full advantage of the potential these plasma channels offer for many applications their properties including the transient behavior must be known. Two key parameters of laser plasmas are the electron density N_e and electron temperature T_e. While the transient behavior of the electron density in air plasmas was measured with a fs probe in Reference [55] the transient electron temperature has not yet been determined with sub ns temporal resolution.

Using a pump-probe technique, we determined the transient electron temperature and electron density in an air plasma with picosecond resolution by measuring the real and imaginary parts of the time-dependent refractive index, applying the Drude model and simple plasma kinetics.

1.3 Dissertation outline

Chapter 1 is the introduction to the research background and the motivation of this work. Chapter 2 describes the experimental tools and techniques used in the dissertation research. Chapter 3 presents studies of material modification and optical damage.

Chapter 4 deals with material incubation under laser load.

Chapter 5 covers the study of transient processes in air plasmas and exploration of signal guiding and transmission.

Chapter 6 provides a summary of the dissertation and the outlook for future work.

The appendices give additional information about the work. A list of publications related to the work during my Ph.D. study is shown in Appendix N.

Chapter 2

Experimental tools and techniques

In this chapter, we will describe the experimental tools and techniques used in this work. We will describe the laser system, the data acquisition system, the technique for pulse duration measurement and the technique for beam size measurement.

2.1 Laser system

2.1.1 Femtosecond oscillator and amplifier

The laser system consists of a home-made femtosecond (fs) Ti:sapphire oscillator [6, 56] and a commercial fs Ti:sapphire amplifier. The oscillator parameters are listed in Table 2.1. A typical spectrum is shown in Figure 2.1.

The amplifier laser is a multi-pass amplifier using chirped pulse amplification (CPA) (Quantronix, model: Odin-II HE). The specifications of the amplifier are listed in Table 2.2. A typical output spectrum of the amplifier is shown in Figure 2.2. For the amplifier, the input oscillator spectrum was positioned optimally at 775 nm to ensure a maximum amplified pulse bandwidth. Since the gain profile of Ti:sapphire

Power (cw)	300 mW
Power (mode-locked)	300 mW
Repetition rate	100 MHz
Pulse energy	3 nJ
Peak wavelength	$\sim$ 775 nm
Bandwidth (FWHM)	$\sim$ 60 nm
Typical pulse width (FWHM)	20 fs
Shortest pulse width (FWHM)	9 fs

Table 2.1: Femtosecond oscillator parameters.

falls more steeply at wavelengths shorter than 800 nm than at wavelengths longer than 800 nm [57], and since gain saturation tends to redshift the spectrum (red wavelengths precede blue in the pulse), the optimum input spectrum is peaked shorter than 800 nm [6]. As a result, the amplifier spectrum is redshifted relative to the oscillator spectrum.

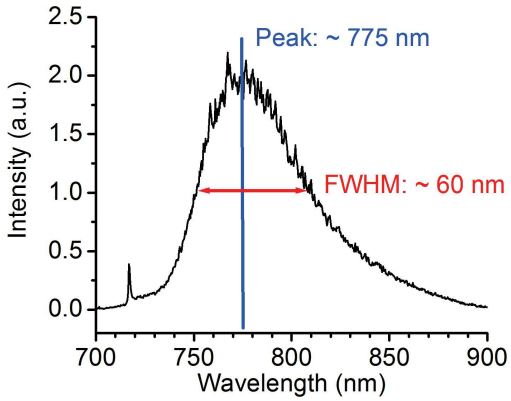

Figure 2.1: Typical spectrum for the fs oscillator output. The spectrum is peaking at 775 nm with a width (FWHM) of 60 nm.

Repetition rate	1.0 kHz
Pulse energy	2.2 mJ
Beam radius ($1/e^2$)	$\sim$ 7 mm
Center wavelength	$\sim$ 812 nm
Bandwidth (FWHM)	$\sim$ 40 nm
Typical pulse width (FWHM)	40 fs
Shortest pulse width (FWHM)	35 fs

Table 2.2: The specifications of the amplifier. The pulse width is tunable using the pulse compressor from 35 fs to 1 ps.

2.1.2 Third harmonic generator

A diagram of the third harmonic generation unit (THGU) is shown in Figure 2.3. It used two type-I BBO crystals to convert the fundamental frequency into the UV frequency [58]. BBO1 was for second harmonic generation (SHG). It was cut at θ=29.2^o, Φ=0^o. BBO2 was for sum frequency generation of the SH and fundamental wave. It was cut at θ=44.3^o, Φ=0^o. Before the fundamental IR beam was sent to the

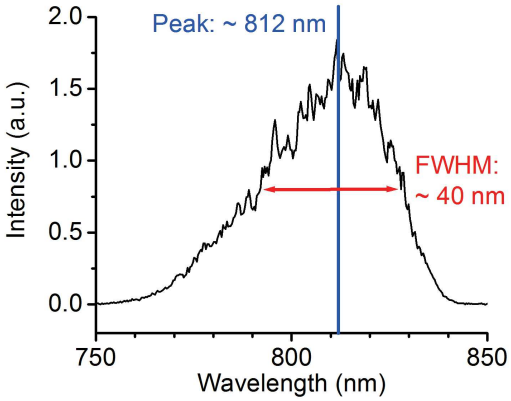

Figure 2.2: Typical spectrum for the fs amplifier output. The spectrum is peaking at 812 nm with a width (FWHM) of 40 nm.

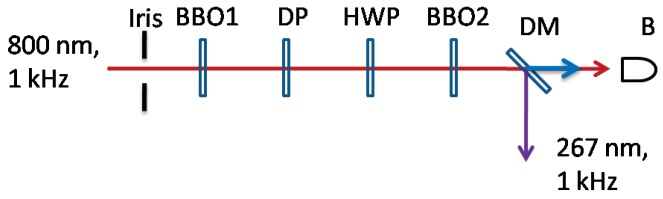

Figure 2.3: Optical layout of the third harmonic generation unit (THGU). BBO1: second harmonic (SH) generation BBO crystal (size: 10×10×0.2 mm^3), DP: delay plate (size: 12.5×20×1 mm^3), HWP: half-wave plate for IR, BBO2: BBO crystal for sum frequency generation of the SH and fundamental wave (size: 10×10×0.1 mm^3), DM: dichroic mirror (high reflection for UV, high transmission for fundamental wave and SH), B: beam blocker.

tripler, the beam size was reduced to half size ($w_{1/e^2} \approx 4$ mm) by a mirror telescope. The delay plate (DP) was a piece of Calcite window (cut at θ=60^o, Φ=0^o). It was used to compensate the walk off between the fundamental pulse and the second harmonic pulse produced by passing through the half-wave plate (HWP). The input IR pulse energy was 1.6 mJ. The output UV pulse energy was around 0.16 mJ. The energy conversion efficiency is about 10%. The efficiency is on a similar level as reported by literature [59] and by commercial laser manufacturers (e.g. Maximum 8% by Del Mar Photonics Tsunami).

2.2 Data acquisition system

In the experiment measuring the multiphoton absorption coefficients of sapphire and fused silica plates, we used two identical photodiodes to measure the reference signal and the transmission signal at the same time. The signals from a train of 1000 pulses were recorded for each pulse.

This was realized by using a data acquisition card and a LabVIEW program.

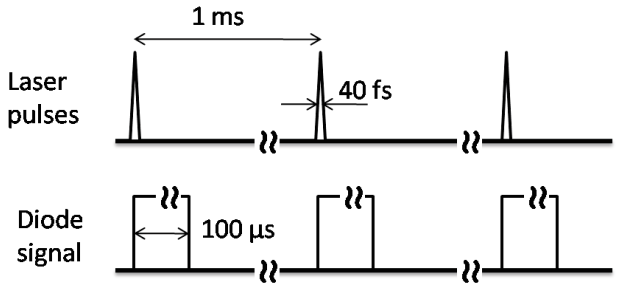

Figure 2.4: The response of photodiodes to the laser pulses. The width (FWHM) of the laser pulse is typically 40 fs. The repetition rate of the laser is 1 kHz. Therefore, the time separation between pulses is 1 ms. The diode signal is kept for 100 μs without significant change, and then is cleaned to zero before the next pulse arrives.

The name of the program is Pump and Probe Controller. It was first edited by Jan Vetterlein for pump-probe experiment [60]. More features were later added by Christian Karras. The program can be used for controlling step motors, reading photodiode values and saving data. It can acquire data from a maximum of four photodiodes. For motion control, it can work with three step motors at the same time.

The photodiodes are Si photodiodes from ThorLabs (model: FDS100, active area: 3.6 mm $\times$ 3.6 mm, wavelength range: 350-1100 nm). When an 800 nm laser pulse incidents on the photodiode, a signal will rise within 10 ns corresponding to the incoming intensity. The pulse width is typically 40 fs, which is much shorter than the diode response time. As a result, the photodiode integrates over the pulse width and gives the final voltage signal. This signal is then proportional to the pulse energy.

In the data acquisition process, these photodiodes were controlled by an electrical circuit to hold the signal for about 100 μs to be collected by the program. After that, all the signal was cleaned to zero before receiving the signal from the next pulse. Figure 2.4 demonstrates the response of the photodiodes to the laser pulses.

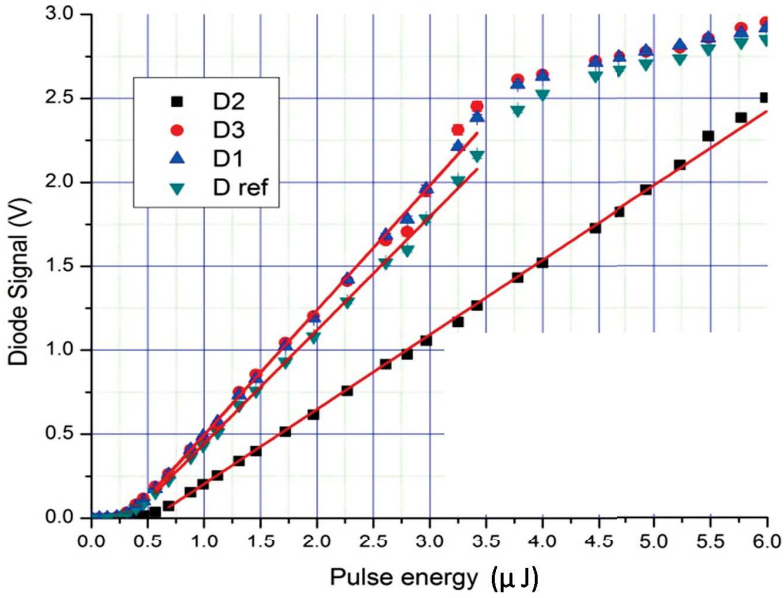

Figure 2.5: Calibration of the photodiodes. Here four identical diodes were calibrated with a power meter: D1, D2, D3 and D ref. The dots are experimental data. The red lines are the fit curves of the measurements. The fitting results for each diode are shown in Table 2.3.

The photodiodes were calibrated with a power meter (Ophir, model: PD 100 UV). The output voltage as a function of the input pulse energy is shown in Figure 2.5 (measurements accomplished by Christian Karras). From the calibration curves, we

Diode	A	Error	B	Error
D2	-0.241	0.005	0.444	0.003
D3	-0.244	0.015	0.741	0.013
D1	-0.249	0.006	0.744	0.006
D ref	-0.232	0.007	0.676	0.006

Table 2.3: Linear fit of calibration curves with equation $y = A + B * x$, x: Pulse energy (μJ), y: Diode signal (V).

can see that the linear response range is from 0 to 2.0 V. From the fit of each curve (results listed in Table 2.3), it was found that there was an offset of around -0.24 V for each diode.

2.3 Pulse duration measurement

In our lab, we have several setups available to measure the pulse duration. For the fs IR laser, the pulse duration can be checked with a commercial FROG (frequency-resolved optical gating) GRENOUILLE (model: 8-20-USB). In addition, we have two home-made auto-correlators for pulse width measurement. One uses the second harmonic generation with a BBO crystal as the nonlinear optical element. Another uses the self-diffraction method with a piece of 100-μm thick fused silica substrate [61]. The GRENOUILLE and second harmonic auto-correlator can only work for pulses at 700 - 1100 nm. The auto-correlator using self-diffraction can work for the pulse width measurement of UV pulses. For a review of different methods for measuring ultrashort laser pulses, please see reference [61].

2.4 Beam size measurement

In our experiments, we often need to measure the beam size to position the sample in the focal plane of laser. Unless mentioned otherwise, we used the knife edge method to measure the beam size. For a general description of this method, see reference [62]. For beams with a radius of a few ten μm, the knife edge need to be of high quality. The knife edge was made from a piece of 100-μm thick aluminum foil. We cut the foil with a razor blade to get the sharp and smooth edge. The edge was glued onto a 1-inch diameter glass window with tape for the convenient of mounting. Under an optical microscope, the edge can be checked.

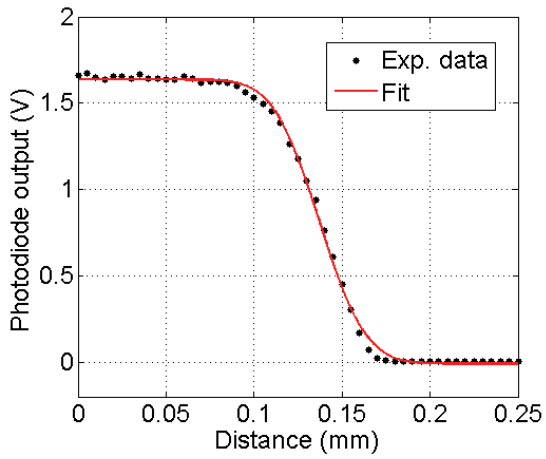

Figure 2.6: An example beam size measurement using the knife edge method. From the fit, the beam radius can be obtained. For the measurement shown here, the fitted w_{1/e^2} is 41.5 μm.

Another issue one needs to be pay attention to is avoiding using absorptive or reflective neutral density filters in the optical path for ultrashort pulse experiments. These filters can change the beam size at the sample position because of the thermal lens effect from absorbing the laser energy. These filters can be used before photodiodes when the beam profile is not a concern but just to reduce the pulse intensity.

Figure 2.6 shows an example data using knife edge method and the fit with the error function assuming Gaussian beam profile. w is the beam radius for intensity $I = I_0 \cdot 1/e^2$, where I_0 is the peak intensity. Using the pulse energy E, pulse duration τ, and w, we can calculate the peak intensity and peak fluence. Appendix A gives the transformations for a Gaussian pulse.

Chapter 3

Material modifications by laser pulses and optical damage

3.1 Introduction

3.1.1 Background

Laser induced damage (LID) study with bulk materials is often affected by nonlinear and propagation effects depending on the pulse duration and bulk geometry, including Brillouin scattering, self-focusing, and self-phase modulation [19]. Femtosecond pulses are more likely to probe intrinsic material properties [44], and thin films can minimize the impact of undesired effects associated with pulse propagation [49].

The topic of damage in thin optical films is very complex because it is at the interface of many areas, from material science to solid state physics to the engineering of the film deposition process. New challenges are presented by the need of ever more powerful lasers for high-quality optical coatings and the fact that such lasers are becoming available at new wavelengths in the IR and UV spectral regions [63].

To explain the LID in dielectric materials, Schaffer *et al.* used rate equations to predict the laser induced damage threshold (LIDT) [28]. This damage model can explain experimentally derived scaling laws relating the sub-ps 1-on-1 threshold fluence to the pulse duration and bandgap of the materials [33]. It can also predict S-on-1 damage by adding the consideration of mid-gap states [34]. However, the model was never applied to explain damage with pulses with duration of hundreds-ps and tens-ns. It is important to evaluate the validity of the model for different pulse durations.

For longer pulses, the occupation and re-excitation of mid-gap states need to be considered. With a pair of sub-ps pulses, the presence of an intermediate state was revealed. This is in agreement with former similar tests of HfO_2 films [64].

For the electron excitation in LID, three different photon ionization mechanisms were proposed: multiphoton absorption (MPA), avalanche and tunneling [28] (see detail explanation in 3.2).

In the past two decades, fused silica has often been studied with respect to these nonlinear absorption processes. However, the MPA coefficient produced by multiple pulses and single pulse was not differentiated [35, 36]. Because laser induced defects will be produced in the multiple pulse illumination, the incubation will trigger a change in the absorption behavior of subsequent pulses. The difference between single pulse and multiple pulses MPA coefficients needs to be clarified.

The role of avalanche ionization in LID is still under debate for dielectric materials according to the recent studies on sapphire plates [40, 41]. As for its role in thin film damage, no work was reported.

Among the study of the nonlinear physical processes, the role of circular and linear polarization in MPA is an interesting topic. Early work in theory suggested that a strong dominance of circular over linear polarization in MPI [65]. Later,

it was suggested that for high order of MPI, a reversal of this behavior might be expected [66]. Some experimental results are agree with the later theory [42, 67, 68]. Others do not agree the theoretical prediction [43, 69].

The latest results of thin films with circular and linear polarization was conducted using a 30 ps laser 40 years ago [43]. From those results, it is hard to tell how the damage behavior is affected by polarization because of the big error bars. Reducing the error bars will help clarify the LID dependence on polarization for thin film damage. Using shorter pulses of a few ps or fs durations, we observe more deterministic damage threshold values [63]. Also, the impact of impurities in today's high-quality films is smaller than what was observed in those earlier experiments. The polarization dependence can thus be studied today with better sensitivity.

The morphology change of films is a direct result of the laser illumination. Incubation affects the morphology of the craters in LID. Normally, laser induced periodic surface structures (LIPSS, often termed "ripples", see Figure 3.37 as an example) can be observed after the illumination of solids with ultra-short pulses [46]. In most of the experiments, ripples appeared after multi-pulse illumination of the samples. Ripples are in general explained by the interaction of incident laser pulses with surface electromagnetic waves [45, 47]. The roughness of the surface is considered as the trigger for the surface electromagnetic wave upon laser illumination. Experimentally, no work demonstrated the surface structure change before the ripples were formed. In our tests, we obtained different structures which would help to explain the formation of ripples. This provided experimental evidence of the trigger for the surface electromagnetic wave.

3.1.2 Chapter goals and contents

In this chapter, we will discuss modifications and damage of some dielectric materials with laser pulses. The samples are bulk materials and thin films.

In our study, we focused on dielectric films with thickness from 80 nm to 200 nm, which is the normal film thickness in coating manufacturing. Some tests were conducted on tens to hundred μm thick thin dielectric substrates. All the materials studied have wide band gaps.

Based on the literature review, here are the issues we are going to address in the following sections:

- Present the pulse laser induced damage (LID) model.
- Conduct damage tests on thin films with ns pulses and discuss the validity of the LID model from fs to ns pulses.
- Measure the transient relaxation in the thin films to prove the existence of the mid-gap states.
- Study the incubation effect on MPA coefficients of thin fused silica and sapphire plates by illuminating with a pulse train.
- Check the role of avalanche ionization through a two-color pulse pair LID test.
- Explore the polarization dependence of LIDTs with fs and ps pulses.
- Characterize the process of LID using the morphology change of the laser illuminated films.

Material	E_g (eV)	n	references
TiO_2 film	3.3	2.39	[33]
HfO_2 film	5.1	2.09	[33]
Sc_2O_3 film	5.7	1.97	[70, 71]
fused silica (SiO_2)	8.3	1.50	[33]
sapphire (Al_2O_3)	8.3	1.76	[41]

Table 3.1: The Properties of some selected dielectric materials (bulk and thin films). E_g: band gap energy, n: index of refraction at λ= 800 nm.

3.2 Pulsed LID model

LID is preceded by energy deposition into the sample. For pulsed laser excitation, the energy is transferred into the material through nonlinear absorption of the incident radiation. In wide-gap dielectric materials, the band gap between the valance band (VB) and the conduction band (CB) is bigger than the single photon energy for UV - IR lasers. Figure 3.1 shows the energy diagram of such materials [63]. The material is transparent to the light at low intensity. However, when the pulse intensity is high enough, especially with sub picosecond (ps) pulses, nonlinear absorption will be initiated [28]. Table 3.1 shows the properties of some selected dielectric materials (bulk and thin films) [33, 41, 70, 71].

3.2.1 Electron density rate equations

One channel for energy deposition is through multiphoton absorption (MPA) [29]. The electrons are at the low energy VB. With high laser pulse intensity, an electron can absorb several photons at the same time. This will promote it to the high energy CB. As a result, the material VB is "ionized". This process is called multiphoton ionization (MPI). Another channel of excitation is through tunneling ionization. This happens in the presence of a strong laser field leading to a Stark-effect induced

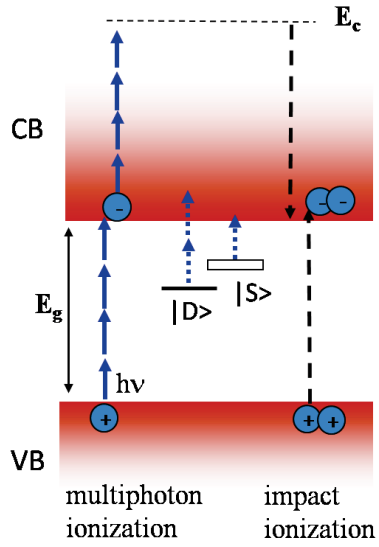

Figure 3.1: Typical energy diagram for a wide-gap dielectric material. CB: conduction band, VB: valence band, E_g: band gap energy, E_c: critical energy for impact ionization, $|S>$ and $|D>$ represent shallow and deep defects states [34]. Shallow defects are within $h\nu$ of the CB and deep defects have ionization energy $> h\nu$. These mid gap states can be intrinsic or laser induced in the material. Excitations of electons through multiphoton ionization and impact ionization are shown in this diagram.

benting of band structure, which enables tunneling from VB to CB. The interplay of MPA and tunneling is described by the Keldysh theory [30].

Once the electron is in the CB, it can continuously absorb photons. This type of absorption is called free carrier absorption. This process involves the interaction of electrons, photons and lattice. When an electron acquires enough energy, it can transfer its energy to another electron in the VB through a collision. As a result, the electron goes to the bottom of the CB and another electron is exited to CB. This is called impact ionization (or avalanche ionization) [29]. It can cause an avalanche-like increase in the CB electron density N.

Once the electrons are pumped into the CB, they relax back to VB or into trap

states after some time. All these processes can be expressed in a rate equation for N in the CB [49],

$$\frac{d}{dt}N(t) = K(I) + A(I, N) - L(N). \tag{3.1}$$

The first term on the right-hand side, K, is the direct photon ionization rate including MPA and tunneling ionization. The second term, A, describes the impact ionization. The third term, L, takes into account relaxation out of the CB. The change of electron density in the VB can often be neglected because the maximum removed electron density is several orders of magnitude smaller than a typical VB electron density.

3.2.2 Damage criterion

As N is building up through photon ionization, damage happens when it reaches a critical N_{crit} [28]. At that point, the plasma frequency coincides with the laser frequency, which makes the electron plasma highly absorptive. There is a resonant absorption of the input pulse energy. This leads to the damage of the material. From the Drude model (see Section 5.2) [72], $N_{crit} = \omega^2 m_e \epsilon_0 / e^2$, where $\omega = 2\pi c/\lambda$ is the optical frequency, e and m_e are the electron charge and mass, respectively, ϵ_0 is the permittivity of free space [49]. For $\lambda = 800$ nm, $N_{crit} = 1.74 \times 10^{21}$ cm^{-3} ($N_{crit} = 1.12 \times 10^{21}$ cm^{-3} for $\lambda = 1064$ nm).

3.2.3 Incubation in multiple pulse damage

For LID measurements, we differentiate 1-on-1 test and an S-on-1 test. In a 1-on-1 test, each spot on the sample is illuminated with a single pulse. In S-on-1 tests, each spot is illuminated with S pulses. It is well-established that the damage threshold for multiple pulse exposures (S-on-1 test) is lower than single-pulse illumination (1-on-1

test) [49]. This effect is called incubation. This phenomenon implies laser induced modifications to the material, which "weakens" it to the subsequent laser exposures.

Incubation is attributed to the accumulation of electrons in mid-gap states between the CB and the VB. The source of these mid-gap trap states are defects in the material, and we will distinguish native defects (intrinsic property of the material) and laser induced defects (produced after interaction with laser pulses). Examples of the native defects are point defects that can be expected in wide gap oxides such as interstitials and vacancies [73], some of which have also been detected directly using electron spin resonance [74]. For thin films, the material is nearly amorphous. Therefore, there is no grain boundary defects, which are normal in the crystal structure [75]. the Examples of the laser induced defects are polarons [76] and self-trapped excitons that may lead to color centers [77]. In addition, calculations show that surface and interface states create energy levels near the VB and CB band edge [78]. All these states, when occupied, provide additional excitation channels, lowering the laser induced damage threshold (LIDT).

Important properties of these mid-gap states are their density, trapping rate, lifetime, and photo ionization cross-section. Except for a few cases in bulk materials (e.g. fused silica and single crystals), little is known about the optical properties of defects, in particular in films. Measurements suggest that relaxation time of electrons out of the CB for fused silica is on the order of hundreds of fs [79].

The damage fluence measured as a function of pulse number, $F_{th}(S)$, in an S-on-1 experiment contains information about the properties of the native mid-gap states and the generation rate of laser induced defects. A plot of the $F_{th}(S)$ versus S is sometimes called the characteristic damage curve, and it reflects the nature of the incubation [49]. Combined with appropriate models, measured characteristic damage curves can provide insight into complex material properties following short pulse excitation. Normally, the models will consider the formation, occupation and

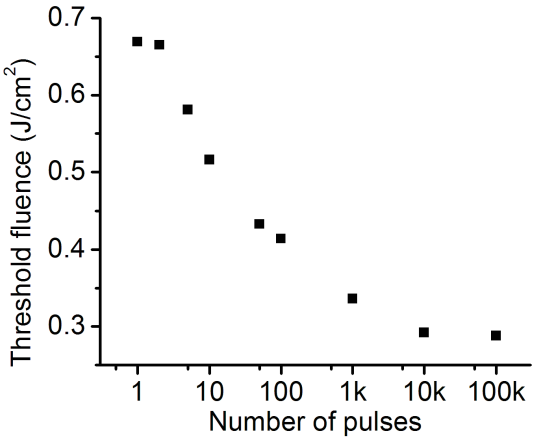

Figure 3.2: Typical incubation curve showing decreasing threshold fluence for larger pulse numbers. The data were taken with a 1-kHz, 55-fs Ti:sapphire laser and TiO_2 thin films.

re-excitation of mid-gap states and predict the CB electron density during the pulse train. An example of a characteristic damage curve is shown in Figure 3.2.

3.3 LID test with ns pulses and modeling

3.3.1 Introduction

Using the rate equation model, success has been achieved in the explanation of some LID tests with sub-ps pulses. By solving Equation 3.1, the damage model was able to explain experimentally derived scaling law relating the sub-ps 1-on-1 threshold fluence to pulse duration and material band gap [33, 80]. By adding additional equations for mid-gap states, the model can predict S-on-1 damage. Good agreement between the characteristic damage curve $F_{th}(S)$ and the model was obtained [34].

It is important to evaluate the validity of the model for longer (ps and ns) pulse

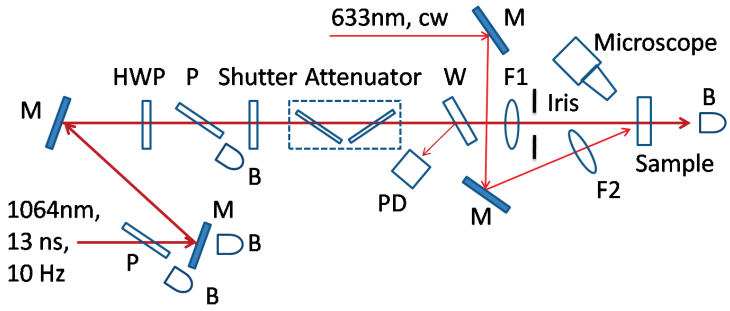

Figure 3.3: LID test setup with ns laser. P: thin film polarizer, angle of incidence (AOI) =56^o, M: mirror, HWP: half-wave plate, W: glass window, F1: focusing lens f=20 cm, F2: focusing lens f=10 cm, PD: photodiode, B: beam blocker.

durations. For longer pulses, the occupation and re-excitation of mid-gap states need to be considered even for the 1-on-1 test. The damage test with ns pulses was conducted on thin Sc_2O_3 films. It was found that the model can be applied to LID from fs to ns for nascent films [81].

3.3.2 Experimental setup

Figure 3.3 shows the damage setup with ns pulses. The laser pulses are provided by a Spectra-Physics Nd:YAG laser (Quanta-Ray GCR series 6300). The system includes both an oscillator and an amplifier. In the damage test, the amplifier was not used. The maximum pulse energy from the oscillator is 280 mJ. The repetition rate is 10 Hz. The average pulse duration (FWHM) is 13 ns (see Figure 3.4). The beam radius of laser output is around 4 mm (obtained by illuminating a preexposed photographic paper). The coarse adjustment of the laser energy was realized by a HWP and polarizer combination. After the beam passes through the HWP and the second thin film polarizer, the extinction ratio of the polarized beam is 127. Fine adjustment of the laser pulse energy was performed with a counter-rotation thin glass

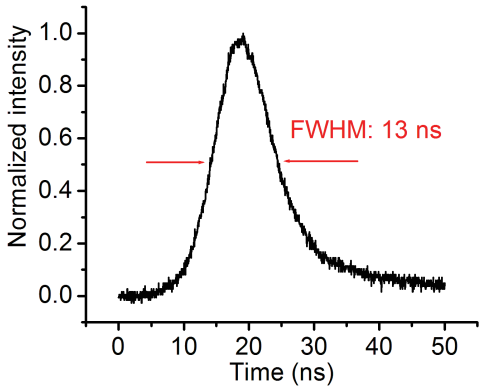

Figure 3.4: The shape of the Nd:YAG laser pulse taken by a fast InGaAs photodiode (Electro-Optics Technology, ET-3000, model: 30-2508). This is a single pulse event.

pair. The range of attenuation that could be obtained considering the geometrical constraints was from 0 to 30% of the input energy.

A mechanical shutter was used to choose the number of pulses incident on the sample. The shutter was connected to a digital signal generator, which provided the trigger. The signal generator was synchronized with the Q-switch output from the laser. The power supply voltage for the shutter is 13.3 V. The current is around 0.21 A.

The scattering change of the thin film was monitored by an on-site microscope. The amplification factor of the microscope is about 200. The working distance of the microscope is about 45 mm. In the experiment, the object plane is behind the sample surface so that the scattering change on the surface can be detected more easily. Because the Nd:YAG laser was blocked by the shutter after each damage event, a 1-mW cw He-Ne laser provided the illumination source for the scattering change.

The beam profile at the laser output was not Gaussian and showed modulation.

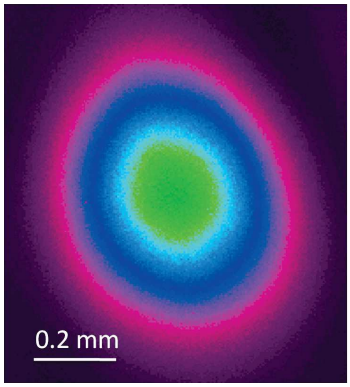

Figure 3.5: The far-field beam profile of the ns Nd:YAG laser. This image was taken in the focal plane of a f=2.0 m lens.

This could come from the disturbance of laser modes by the presence of apertures, refractive index gradients of optical elements used, imperfect optical surfaces and other perturbing influences. However, the profile was Gaussian in the far field without modulation. The image near focus with a f= 2.0 m lens is shown in Figure 3.5. The profile outside the focal plane was not Gaussian. It is important to place the sample in the focal plain.

The beam size at the focus of the lens was measured with a beam profiler. With Gaussian fit, the beam radii are $w_x = 20\mu$m and $w_y = 24\mu$m. A piece of white paper at the position of the sample was placed to optimize the sample location along the beam propagation direction. At the focal point, the fluorescence from the paper is the strongest. A similar test was done with a 100-μm thick metal foil. At the focal point, the plasma emission from the metal foil is the strongest. In the experiment, the distance from the lens to the sample was set to 20.9 cm with a f=20 cm lens.

In the experiment, hafnia (HfO_2, band gap: 5.1 eV [33], thickness: 216 nm)and scandia (Sc_2O_3, band gap: 5.7 eV [70], thickness: 130 nm and 200 nm) thin films were tested. Appendix B gives more information about the tested films. Amorphous films

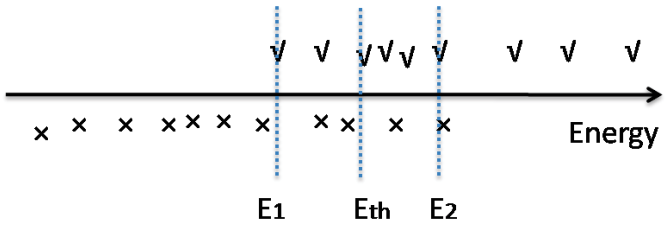

Figure 3.6: The status of the illuminated film spots, "yes" ("$\surd$", damaged) or "no" ("$\times$", not damaged), as a function of the pulse energy. E_1 to E_2 represent the energy range for the damage probability increasing from 0 to 1 [49]. $E_{th} \approx (E_1 + E_2)/2$ represents the threshold energy for 0.5 damage probability.

were deposited by ion beam sputtering (IBS). IBS produces high quality metal-oxide films free from micron-size inclusions or local absorbers, which is critical to isolate the contribution of point defects to laser breakdown. Details about the fabrication parameters can be found in [81]. From the study of the debris distribution after a damage event, the spacing between spots was set to 0.5 mm for single pulse tests and 1.0 mm for multiple pulse tests.

3.3.3 Results

In a typical damage test, the pulse energy is changed. The status of the illuminated film spot, "yes" (damaged) or "no" (not damaged), is recorded as a function of the pulse energy (see Figure 3.6). E_1 to E_2 represent the energy range for the damage probability increasing from 0 to 1 [49]. $E_{th} \approx (E_1 + E_2)/2$ represents the threshold energy for 0.5 damage probability and this is the value we will report in what follows unless stated otherwise. We use the corresponding fluence for E_{th} as the LIDT fluence, and the fluence range for $(E_1 - E_2)/2$ as the uncertainty range, also referred to as error bars in LIDT measurements.

Typical damage crater images are shown in Figure 3.7. The LIDTs as a function

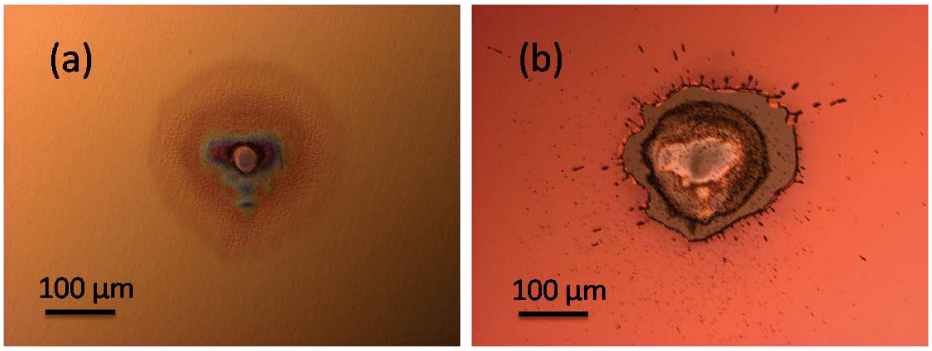

Figure 3.7: Typical damage craters produced with single ns pulses on (a) HfO_2 and (b) Sc_2O_3 films.

of the number of pulses for HfO_2 and Sc_2O_3 are shown in Figure 3.8. The threshold decreases with the number of pulses and is constant for $S > 5$.

In LID tests with ns pulses, the LIDT has much larger fluctuations comparing to fs pulse results. The error bars can be 30 to 70% of the LIDT values. For fs pulses, that ratio is only 1 to 3%. Studies with single ns pulse damage technique showed that the large range is related to the defects distribution inside the film [63]. It was found that the damage threshold of intrinsic material was higher than that of the

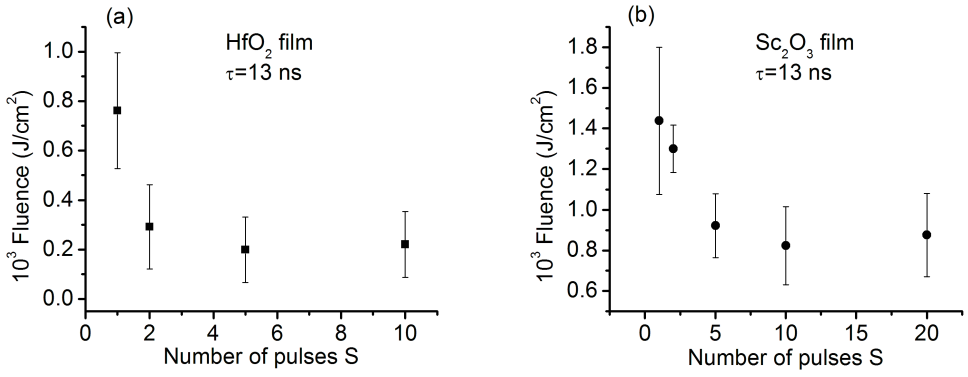

Figure 3.8: F_{th} vs S for ns pulses for (a) HfO_2 and (b) Sc_2O_3 films.

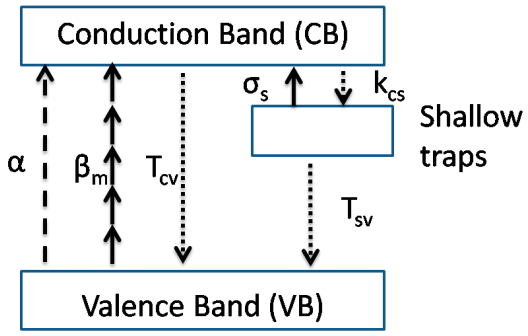

Figure 3.9: Excitation and relaxation processes in wide-gap dielectric material. The notation is explained in Table 3.2.

defects. This is one reason for the large uncertainty.

As a reference, the single pulse LIDT of bulk fused silica was also measured (1064 nm, 13 ns). The threshold fluence is 3050±600 J/cm^2. The high limit from literature is 3854±85 J/cm^2 (1064nm, 8 ns) [19, 82]. The longer the pulses (13 ns versus 8 ns), the higher the threshold fluence. However, our result is 20% lower and the uncertainty is bigger compared to the limit. This may come from the quality of the fused silica used in our tests. The defects in the sample are responsible for the uncertainty.

3.3.4 LIDT modeling

The LIDT of Sc_2O_3 is simulated with the model described in 3.2 by only considering the shallow trap states. Shallow traps reside near the CB band edge and are often visible as a tail in the band absorption edge [34]. The energy diagram and transition processes are shown in Figure 3.9. The rate equations for the electron density in the

Symbol	Description
I	Laser pulse intensity
α	Avalanche ionization coefficient
β_m	Multiphoton absorption coefficient
m	Order of MPA
T_{cv}	CB to VB relaxation time constant
k_{cs}	CB to shallow trap relaxation rate
$N_{s,max}$	Maximum density for shallow traps
σ_s	Absorption cross section of shallow trap
T_{sv}	Shallow trap life time

Table 3.2: Material parameters for modeling the processes sketched in Figure 3.9

Pulse duration	LIDT (J/cm^2)
40 fs	0.70 ± 0.06
375 ps	15.0 ± 2.6
13 ns	623 ± 174

Table 3.3: Average 1-on-1 LIDT fluences for Sc_2O_3 films with fs to ns pulses. In the test, several samples were tested. Listed are the average values. The test with 375 ps pulses was performed by our collaborators [81].

CB and the shallow defect population can be written as [34, 81]

$$\begin{aligned}\frac{dN}{dt} =&\alpha N(t)I(t) + \beta_m I(t)^m - \frac{N(t)}{T_{cv}} \\ &- N(t)k_{cs}(N_{s,max} - N_s(t)) + \sigma_s N_s(t)\frac{I(t)}{h\nu} \end{aligned} \tag{3.2}$$

$$\frac{dN_s}{dt} = N(t)k_{cs}(N_{s,max} - N_s(t)) - \sigma_s N_s(t)\frac{I(t)}{h\nu} - \frac{N_s(t)}{T_{sv}} \tag{3.3}$$

The parameters are listed in Table 3.2. In the simulation, the pulse temporal shape was assumed to be Gaussian. The band gap of Sc_2O_3 is 5.7 eV [70]. The MPA is a 5-photon process for 1064 nm light and 4-photon process for 800 nm light. Because in the model the fluence refers to intra-film, a factor ξ multiplies the external fluence [83]. ξ is the result of Fabry-Perot interference inside the film and depends

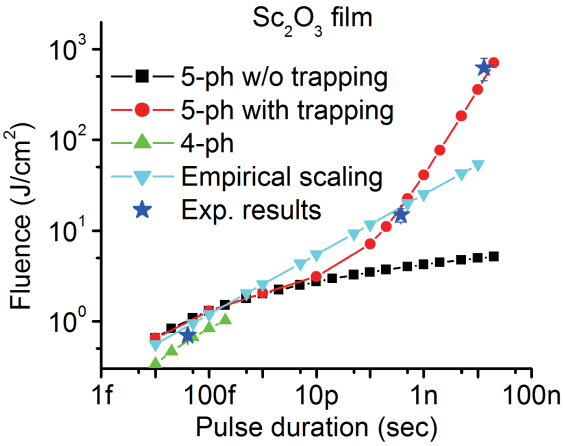

Figure 3.10: Comparison of experiment and modeling. For the results with 40 fs pulse a laser at 800 nm was used. The absorption is a 4-photon process. For the test with 375 ps (λ=1030 nm) and 13 ns (λ=1064 nm) pulses, the MPA is a 5-photon process. The results according to the empirical scaling law for sub-ps pulses [33] were presented also as a comparison.

on the incident wavelength and the film thickness. For an 800-nm laser, it is 0.56 and 0.65 for 130-nm and 200-nm thick films. For a 1064-nm laser, it is 0.54 and 0.59 for 130-nm and 200-nm thick films. The average results are listed in Table 3.3.

The simulation and the experimental results are shown in Figure 3.10. The parameters used in the fit are listed in Table 3.4 [81]. The band-to-band parameters (α and β_m) were taken from measured values for 4-photon and 5-photon materials, HfO_2 and Al_2O_3 respectively [84]. The remaining parameters for shallow traps were adjusted to achieve the best fit. The case without trapping means that there is no relaxation of electrons to the VB or mid-gap states. For short pulses, there is no difference for the two scenarios shown. The excitation is over before the electrons relax. The difference is quite obvious for longer pulse durations.

The results according to the empirical scaling law for sub-ps pulses [33] are pre-

Parameter	Value
α (4-photon)	10 cm^2/J
β_m (4-photon)	2.9 $\times 10^{25}$ cm^5fs^3/J^4
α (5-photon)	12 cm^2/J
β_m (5-photon)	2.3 $\times 10^{24}$ cm^7fs^4/J^5
T_{cv}	1.05 $\times 10^4$ fs (10.5 ps)
k_{cs}	1×10^{-22} cm^3/fs
$N_{s,max}$	3 $\times 10^{18}$ cm^{-3}
σ_s	1 $\times 10^{-22}$ cm^2
T_{sv}	1×10^{14} fs (0.1 s)

Table 3.4: Parameters used for the best fit of the LIDT model to experimental data for Sc_2O_3 films.

sented also as a comparison. $F_{th}(1) = (c_1 + c_2 E_g)\tau_p^{\kappa}$, where $c_1 = -0.16$, $c_2 = 0.074$, $E_g = 5.7$ [eV], and $\kappa = 0.33$. There is a deviation for long pulse durations (> 1 ns). For 13-ns pulse, the measured threshold is about 10 times of the predicted values. Obviously, this empirical scaling law is not applicable for long pulse damage.

Modeling and the experimental data show good agreement from fs to ns LID tests if a single shallow trap is included.

From the fit parameters, we can estimate the relaxation time from the CB to the shallow trap states. The relaxation time is shortest when the shallow traps are empty, $T_{cs,min} = (k_{cs} \cdot N_{s,max})^{-1}$=10 ps; note, the relaxation is bimolecular. As the shallow traps are filled, the relaxation takes longer. From the results, the effective relaxation time is longer than 10 ps. This is verified by the transient behavior measurements of Sc_2O_3 films using a pulse pair (see next section).

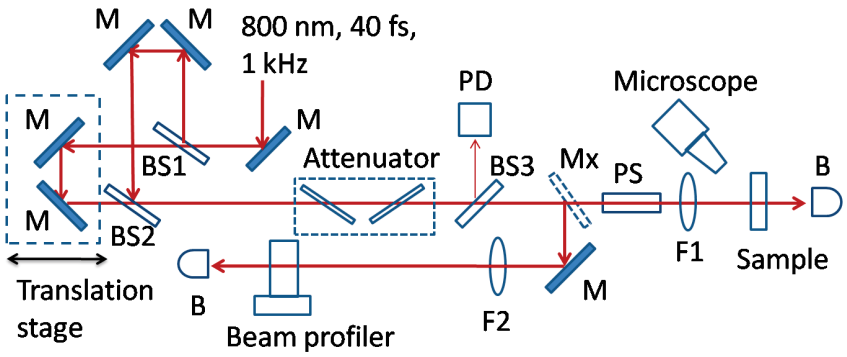

Figure 3.11: LID test with ultrashort pulse pairs. M: mirror, BS1, BS2, BS3: beam splitter (Tran./Refl.=50/50 for BS1 and BS2, 90/10 for BS3), PS: pulse stretcher, F1: focusing lens f=15 cm, F2: focusing lens f=2.0 m, PD: photodiode, B: beam blocker. Mirror Mx was mounted on a flip mount. It was used to overlap the two arms and was flipped down in damage tests.

3.4 Damage measurements with a pulse pair

Damage study on a thin HfO_2 film with a pair of pulses with adjustable delay revealed the presence of an intermediate state [64]. With the same method, two-pulse tests were conducted on the Sc_2O_3 films (thickness: 200 nm). Similar relaxation on a time scale of tens of ps to ns was observed. This is a verification of the presence of mid-gap states. These time constants agree with those that produced the best fit of the LIDT model with experiments from fs to ns, see previous section.

3.4.1 Experimental setup

The experimental setup is shown in Figure 3.11. The pulses from the laser were split in two equal parts at BS1. The delay between the two pulses can be tuned with the translation stage. We label the beam in one arm of the micrometer as the probe beam, the other beam as the pump beam. The maximum possible delay through

the translation stage is 0.5 ns. For delays larger than millisecond, the pump arm was blocked. Instead, an electronic pulse generator was used to change the delay between two successive pulses from the amplifier. Two pulses were delivered through the probe arm. The amplifier is running at 1 kHz. The separation between the two pulses must be integer times of 1 ms. There is no delay setting between 0.5 ns to 1 ms. Adjustment of pulse energy was realized by a pair of counter-rotating glass plates.

The spatial overlap of the beams from the two arms was accomplished through the following steps. First, overlap the two beams on the beam splitter (BS2). Insert a white card so that both beams can be observed. Tune BS1 to overlap the pump beam and the probe beam. Second, overlap the two arms in the far field using BS2. Couple the beams out with a flip mirror mount (Mx). Send them through a f=2.0-m lens into a beam profiler and adjust the overlap.

After finishing the spatial overlap, change the delay between the two arms. Near zero time delay, we can observe interference fringes from the beam profiler.

From the measurments for HfO_2 films (see Figure 3.12), the difference in damage fluence across the inaccessible region between 1 ns and 1 ms is about 25% with 50-fs pulses. In contrast, with the 1-ps pulses, the change is only a few percent. A simple predication is that there is no change for the region between 1 ns and 1 ms with 1-ps pulses in HfO_2 [64]. We stretched the fs laser pulses to ps for our experiments of Sc_2O_3 films. Before the beam is incident on the sample, it passes through a pulse stretcher, a 11-cm long glass block. Both end surfaces are AR coated. The pulse duration is stretched to 0.6 ps from 40 fs.

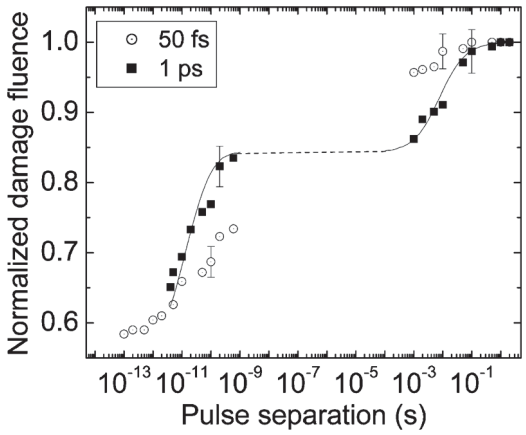

Figure 3.12: Normalized LIDT fluence versus the delay between the two pulses for HfO_2 films. The values are the fluence of the individual pulses normalized to the single pulse breakdown threshold. The solid line is a guide to the eye while the dashed section is the predicted behavior. This figure was taken from [64].

3.4.2 Results

The LIDT fluence changes with the delay between the two 0.6-ps pulses (see Figure 3.13). The minimum delay was 1.5 ps to avoid interference between pulses that

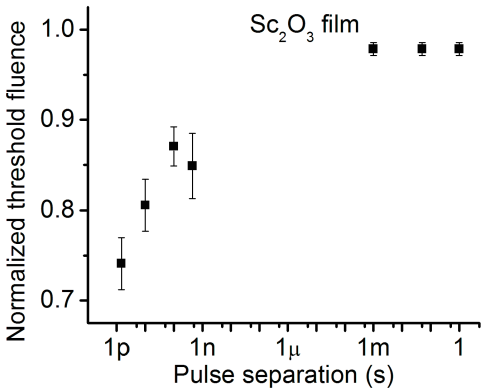

Figure 3.13: Normalized LIDT fluence versus the delay between the two 0.6-ps pulses for Sc_2O_3 films. The whole curve is normalized to the single pulse LIDT fluence, 1.39 J/cm^2.

would complicate data interpretation. Within ns range, we see a relaxation on a time scale of tens ps to ns. From the modeling, the effective relation time from the CB to the traps is longer than 10 ps because of the bimolecular relaxation. The observation is in agreement with the best fit of the model. The time scale is similar to what was observed in HfO_2 film [64].

There is a 13% difference between the ns and ms values from our 0.6-ps Sc_2O_3 results, while there is almost no difference for HfO_2 films with 1-ps pusles [64].

For HfO_2 films, there is a relaxation on a ms time scale. For Sc_2O_3 films, however, there is no observation of that. The LIDT did not recover completely to the single pulse threshold, but remained a few percent lower. This should come from long-lived laser induced material modifications. It has been observed such modification can last for minutes and longer [64].

3.5 MPA measurements on thin dielectric substrates

3.5.1 Introduction

Although there has been a lot of work published in the past two decades on optical breakdown and damage in wide band gap materials, several aspects of the physical mechanism are still unclear. The difficulty is the coexistence of different nonlinear processes in the material excitation. In recent publications, one can find advocates of three different mechanisms for the dominant excitation process: multiphoton [42,85], avalanche [39,86] or tunneling [87,88]. The relative role of these processes in LID of films is still under debate.

Because of the smallness of the signal, no direct measurements of MPA coefficients

in thin optical films exist. Most values were obtained for bulk materials or from fits to LIDT models.

In the past two decades, nonlinear absorption in fused silica has been broadly studied with different methods. In [33, 35, 89], MPA coefficients were determined through the fitting of optical breakdown threshold to the electron density rate equation derived by Stuart *et al.* [90]. In [42], ultrafast time-resolved imaging interferometry was applied to measure the free-electron density at different incident beam intensity. MPA coefficients were obtained from the fit of free-electron density as a function of pulse intensity. In [37–39], the transmission was measured at different pulse energy levels, from which the MPA coefficients were determined. Compared to the other methods, the transmission method is a direct way to get MPA coefficients. For sapphire, recent studies still show big differences in MPA coefficients [41, 85]. In [85], a six-photon absorption was observed with 60 fs pulses at 800 nm. However, the measurements with 40 fs pulses at 800 nm in [41] did not follow six-photon absorption.

Among previous studies, the MPA coefficient produced by multiple pulses [35,36] and single pulse [37–39] were not differentiated. Because laser induced defects will be produced in multiple pulse illumination, incubation will produce a change in the absorption behavior of subsequent pulses. Knowing the effect of these mid-gap states is quite important in understanding LID with a pulse train. The difference between single pulse and multiple pulses MPA coefficients needs to be clarified.

To determine the change of MPA coefficients with pulse number S in a train of pulses, we measured the transmission of a pulse train passing through thin fused silica and sapphire plates. Through the fit of the transmittance curve for different pulse number S, MPA coefficients were calculated as a function of S.

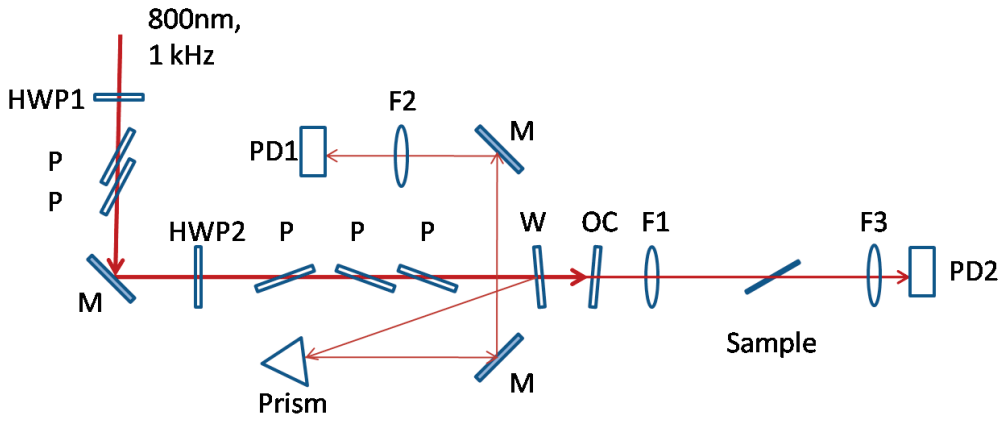

Figure 3.14: Experimental setup for MPA measurements on thin dielectric substrate. HWP1 and HWP2: half-wave plate, P: ultrafast polarizer, M: mirror, W: fused silica window, OC: ultrafast output coupler, F1: focusing lens f=15 cm, F2: focusing lens f=10 cm, F3: focusing lens f=6 cm, PD1 and PD2: photodiode. The reflection from the prism surface was used to reduced the pulse intensity.

3.5.2 Experimental setup

Fused silica and sapphire are dielectric materials with similar band gap, $E_g \approx 8.3$ eV [41]. The photon energy of a 800 nm laser is 1.55 eV. Therefore, for a 800 nm laser beam, the material is transparent for low intensity.

Figure 3.14 shows the experimental setup. The combination of a half-wave plate (HWP) and thin film polarizers (P) was used to attenuate the beam intensity. The first combination (HWP1+P+P) was a commercial attenuator from ALTECHNA. The second combination (HWP2+P+P+P) was assembled from individually purchased components. A glass window W picked a small part of the input beam and sent it to PD1 as the reference signal. The mirror OC was used to reduce the input laser intensity (T=13%). The beam was focused on the sample through lens F1. The transmitted beam was focused through lens F3 and collected by PD2. Both PD1 and PD2 were not placed at the focal point of the input beam. They were before the

focal point to avoid damage. The laser pulse duration before the sample was 40±2 fs. For the peak fluence of 1 J/cm^2, assuming a Gaussian pulse, the peak intensity is 23.5 TW/cm^2.

The samples are thin dielectric substrates from Valley Design Corporation. The thickness for fused silica (SiO_2) is 51 μm. The thickness for sapphire ($\alpha - Al_2O_3$) plates is 89 μm.

The polarization of the input beam before the sample was parallel to the optical table surface ("P"). In order to reduce the reflection and associated standing wave in the sample, the sample was placed at Brewster angle, θ_B. The refractive indexes of fused silica (n=1.45, $\theta_B = 55.4^o$)and sapphire (n=1.76, $\theta_B = 60.4^o$) are different at 800 nm (refractive index values are from Valley Design's website). In the setup, the angle of incidence (AOI) was set to 60^o for easy alignment purpose. The reflection caused by the AOI for fused silica is less than 2%. The reflection for sapphire can be neglected.

The beam radius near the focus was measured in vertical and horizontal directions with the knife edge method. Assuming the beam has a Gaussian profile, we obtained the minimum effective area and the sample position (see Appendix C) at which the fluence was the highest. At this position, $w_{hor} = 46.4\,\mu m$ and $w_{ver} = 19.3\,\mu m$. The reason w_{ver} and w_{hor} are not equal is because the knife edge was placed at θ_B. The effective area is 1.32×10^{-5}cm^2. To reach a peak fluence of 1 J/cm^2, the pulse energy needs to be 13.2 μJ. Since our laser is running at 1 kHz, the corresponding average power is 13.2 mW.

3.5.3 MPA results

In this experiment, the cross-calibration of the reference PD1 and the transmission PD2 is critical. Because the "P" light and the "S" light have different reflection

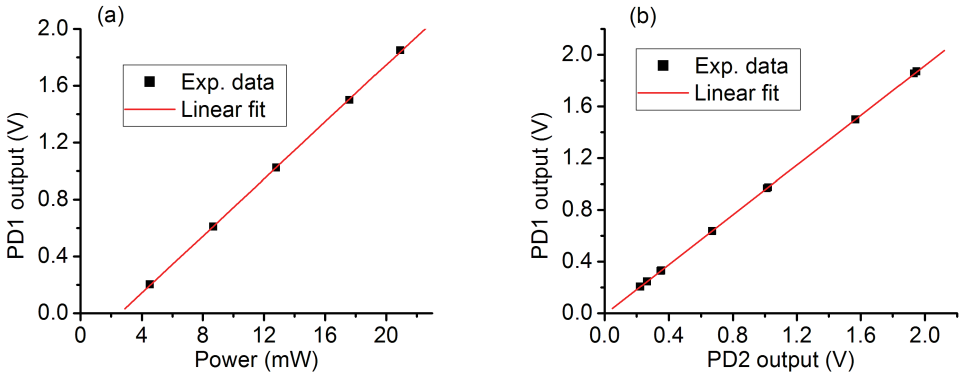

Figure 3.15: (a) Calibration curve of reference PD1. Each data point is an average over 3000 pulses. Notice that the fit curve does not pass through (0, 0). This is because there is an offset from the PDs output. (b) Cross-calibration of PD2 and PD1. Each data point is an average over 4000 pulses.

coefficients at the window and later surfaces, we improved the linear polarization by putting three thin film polarizers after the second HWP. The extinction ratio after the polarizers was greater than 1240. For each beam attenuator, the minimum output was limited to 1/10 of the maximum output to ensure good polarization property. The possible range of pulse energy at the sample was from 0.4 μJ to 20 μJ.

The reference PD1 is calibrated with a power meter before the sample. A calibration curve is shown in Figure 3.15 (a). A cross-calibration curve of the PD1 and PD2 is shown in Figure 3.15 (b), which was obtained with the sample removed. These PDs were silicon PDs and were specially designed for the experiment (see Chapter 2). They can resolve single pulses. The PDs were part of a sample-and-hold circuit that was reset after readout before the next pulse arrived.

The transmitted pulse energy can be calculated using the PD2 output and calibration Figure 3.15 (b) for each pulse. To cover the intensity range (Max/Min $\sim$ 50), we used neutral density filters to restrict PDs output to the range 0.2-2.0 V. Within this range, the transmittance error introduced by the cross-calibration is

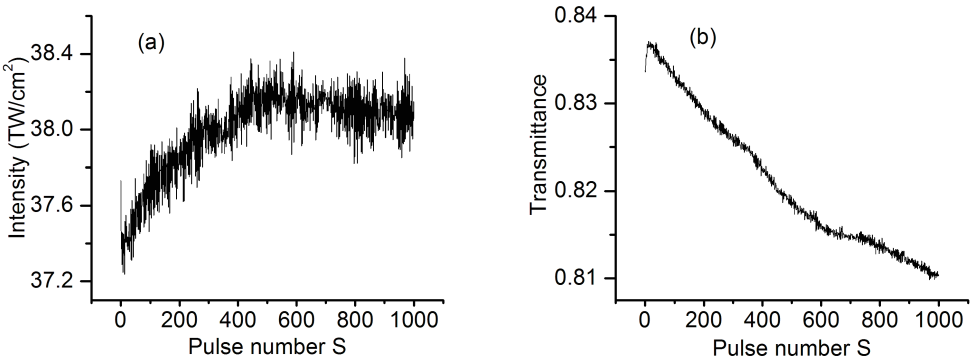

Figure 3.16: The intensity (a) and transmittance (b) versus pulse number of a 51-μm thick fused silica plate. Within a train of pulses, the intensity increases by 2% from the first pulse until $S \sim 500$. It keeps flat for the rest pulses in the train. This comes from the trigger of the Pockels cell in the laser system. The system becomes stable after the first 500 pulses. The results are averaged over 10 events. The transmittance decreases with increasing pulse number, which is a result of material incubation. For sapphire plates, similar transmittance curves were observed.

smaller than 0.5%.

In the experiment, each spot was illuminated with a burst of one thousand pulses spaced 1 ms apart. A data acquisition system recorded the signals from both PDs. The transmission of each pulse was calculated through a LABVIEW program. In order to reduce the signal fluctuation from shot to shot, at each laser energy level, ten events were repeated to get an average transmission curve. Typical results are shown in Figure 3.16.

From these transmission curves, we can plot the transmittance versus peak intensity for a certain pulse number from 1 to 1000. Representative results are shown in Figure 3.17 for fused silica and in Figure 3.18 for sapphire. At low intensity, the transmittance within the pulse train doesn't change. When intensities exceeded 5 TW/cm^2, the transmittance starts to decrease with increasing laser intensity. Incubation becomes obvious for high intensity.

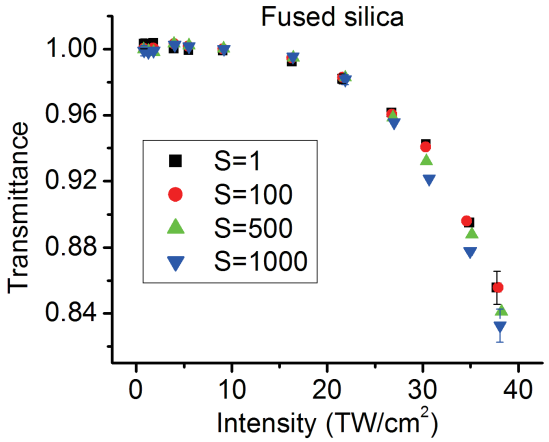

Figure 3.17: Transmittance versus incident intensity of an 800-nm, 40-fs pulse for fused silica for different pulses (S) within the 1000-pulse train. The angle of incidence was set to 60^o. This is not the exact Brewster angle for fused silica ($\theta_B = 55.4^o$). As a result, the transmittance at low intensity is 0.98, instead of 1.00. In order to fit Equation 3.10, a shift of 0.02 is made to the whole data set so that the transmittance at low intensity is 1.00. Each data point is the average value over 10 events. The error bar is the standard deviation of 10 events.

For fused silica and sapphire, in order to excite electrons from VB to CB, a six-photon absorption (6PA) process is needed. In six-photon absorption, the beam intensity change follows

$$dI = -\sigma^{(6)} I^6 dz \tag{3.4}$$

where $\sigma^{(6)}$ is the six-photon absorption coefficient. Integrating Equation 3.4 with respect to z, we can get the transmitted intensity as a function of the input intensity after passing through a sample with thickness L,

$$I(z = L) = I(z = 0)\left[1 + 5\sigma^{(6)} L[I(z = 0)]^5\right]^{-1/5}. \tag{3.5}$$

For Gaussian spatial and temporal shape pulses, the input intensity is a function of r and t,

$$I(z = 0) = I(r, t, z = 0) = I_0 \exp\left(-2\frac{r^2}{w^2}\right) \exp\left(-4\ln 2\frac{t^2}{\tau^2}\right), \tag{3.6}$$

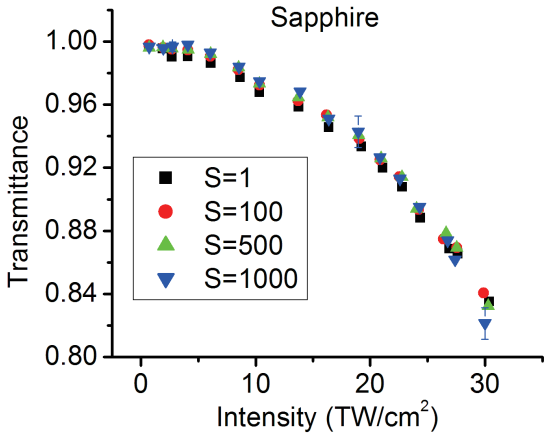

Figure 3.18: Transmittance versus incident intensity of an 800-nm, 40-fs pulse for sapphire for different pulses (S) within the 1000-pulse train. Each data point is the average value over 10 events. The error bar is the standard deviation of the 10 events. For the sapphire sample, the transmittance drops by 0.45 from the $S = 1$ to $S = 1000$ at $I = 37\,\mathrm{TW/cm^2}$ (not shown in the Figure). This involves many physical processes, such as the scattering from the bulk free electron plasma and the white light generation [37]. The transmittance results for $I > 30\,\mathrm{TW/cm^2}$ are not used for the calculation of MPA coefficients for sapphire.

where $I_0 = I(r = 0, t = 0, z = 0)$ is the input peak intensity, w is the beam radius, and τ is pulse duration (FWHM). Similarly, the transmitted intensity is also a function of r and t,

$$I(z = L) = I(r, t, z = L). \tag{3.7}$$

For small absorption, the transmitted intensity can be approximated by

$$I(r, t, z = L) \approx I(r, t, z = 0)\left[1 - \sigma^{(6)} L[I(r, t, z = 0)]^5\right]. \tag{3.8}$$

The reciprocal of the transmittance can be obtained by integrating the intensities spatially and temporally,

$$\frac{1}{T} = \frac{E(z = 0)}{E(z = L)} = \frac{\iiint I(r, t, z = 0) r d\theta\, dr\, dt}{\iiint I(r, t, z = L) r d\theta\, dr\, dt}, \tag{3.9}$$

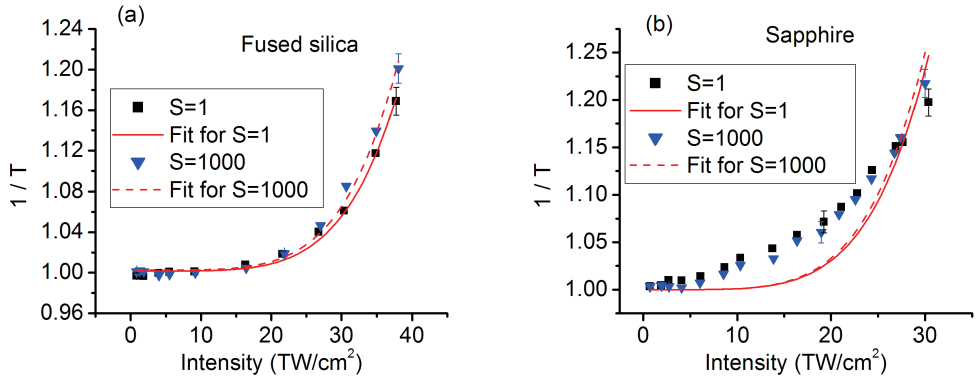

Figure 3.19: Six-photon absorption fit for $1/T$ versus intensity results with Equation 3.10. The results fit well for fused silica (a), but not for sapphire (b). For fused silica, it also has been checked the best fit for the number of photons needed is $m = 6$.

where E is the pulse energy. Inserting Equation 3.8 into Equation 3.9, we can get

$$\frac{1}{T(I_0)} \approx 1 + \frac{1}{6\sqrt{6}}\sigma^{(6)} L I_0^5. \tag{3.10}$$

We found that for fused silica Equation 3.10 fits the data well, but not for sapphire (see Figure 3.19).

For fused silica, the six-photon absorption coefficient for different pulse numbers is shown in Figure 3.20. From the results, the incubation effect is observed in the nonlinear absorption process. The coefficient for $S = 1000$ is increased by 16% compared to that of the first pulse in the train. This result shows that a six-photon absorption process is a good approximation even in the presence of incubation. Incubation means the production of some mid-gap states. In fused silica, these states can provide quasi-resonant intermediate levels, increasing $\sigma^{(6)}$ without changing the order of MPA.

The relation between β_m in Equation 3.2 and $\sigma^{(m)}$ in Equation 3.4 is $\beta_m = \sigma^{(m)}/(mE_{ph})$, where $m = 6$ for fused silica and $E_{ph} = h\nu$ is the photon energy. For

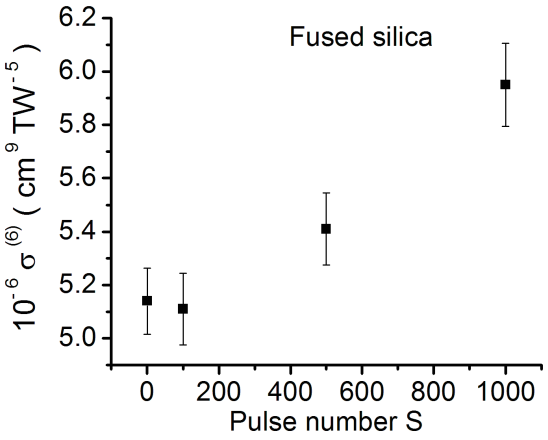

Figure 3.20: Six-photon absorption coefficient as a function of pulse number within the excitation burst for fused silica at $\lambda = 800$ nm. Because the sample is placed at Brewster angle, the effective distance the beam passes through is $L = t/\cos\theta_T$, where t is sample thickness, θ_T is the transmission angle. For fused silica, L=64 μm.

a laser at 800 nm, $E_{ph} = 2.48 \times 10^{-19}$ J. The results of published MPA coefficient β_6 for fused silica are listed in Table 3.5. The six-photon absorption coefficient for the first pulse is within the range of measurements recently published.

From our results, we can see that the six-photon absorption coefficient changes with the pulse number in a pulse train. The difference between single-pulse and multiple-pulse MPA coefficients is clarified in fused silica. The laser induced states do not change the order of MPA in fused silica.

For sapphire, it turns out that a 3-4 photon absorption process fits the results better (see Figure 3.21), although it is supposed to be a six-photon process like in fused silica. The likely reason is a low concentration of midgap states in sapphire undetectable with common spectrophotometers [63]. From the fit of the measurements, we also notice that incubation changes the order of MPA in sapphire. The laser induced states produced by incubation have different impact on the MPA order

No.	β_6	α	τ	S	L	w	I_0	Method	Ref.
1	6×10^{-70}	4	20-5000	50	500	15		A	[35]
2	3×10^{-74}	9	25	2	500	17.5		A	[89]
3	9.9×10^{-68}	8	40-1240	1	0.8	20		A	[33]
4	7.5×10^{-65}	0	50	1	100	51	10-40	B	[42]
5	5.8×10^{-66}	0	90	1	1000	2	9-498	C	[37]
6	4×10^{-65}	4	40	1				C	[38]
7	4×10^{-65}	4	43	1	>150		0.5-25	C	[39]
8	3.5×10^{-66}	0	39	1	64	20	0.8-38	C	this work

Table 3.5: Published MPA coefficient for fused silica. β_6: six-photon absorption coefficient ($(m^2/W)^6 s^{-1} m^{-3}$), α: Avalanche ionization coefficient (cm^2/J), τ: Pulse duration (fs), S: Number of pulses, L: sample thickness (μm), w: beam radius (μm), I_0: beam intensity (TW/cm^2). Method: techniques used in measurements, A: using optical breakdown threshold, B: using interferometry, C: using transmission. For the description of these techniques, see the introduction section. The lasers used in these results were at 800 nm. Reference [33] was a test of thin dielectric films. In References [37], [42] and this work, avalanche ionization was not considered in the calculation of MPA coefficients.

in fused silica and sapphire.

The measurements in sapphire agree with the observation by Karras *et al.* [41]. The intensity range in this study was from 0.7 to 30 TW/cm^2 (a similar range was used in Karras's work). The fluctuations of the transmission measurements were smaller than 5%. The experiments by Mouskeftaras *et al.* [85] were performed with an intensity range from 30 to 100 TW/cm^2. The fluctuations of the measurements using the pump-probe interferometry technique were much bigger than ours. At $I_0 \approx 40$ TW/cm^2, the measurements fluctuated by a factor of 2. At $I_0 \approx 30$ TW/cm^2, the measurements fluctuated by a factor of 4. Although a six-photon absorption law fit on average well near 40 TW/cm^2. That law could not be observed for intensity near 30 TW/cm^2. Measurements at lower intensities were not possible because of their sensitivity limit. From our measurements, the excitation law for lower intensities was obtained accurately.

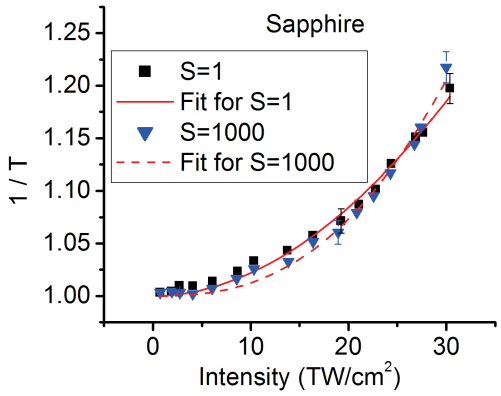

Figure 3.21: MPA fit for sapphire $1/T$ vs intensity results using function $y = 1+b\cdot x^c$, in which c gives the information about MPA order ($m = c+1$). From the fit, $c \approx 1.9$ for $S = 1$, $c \approx 2.1$ for $S = 100$, $c \approx 2.3$ for $S = 500$, and $c \approx 2.6$ for $S = 1000$. This suggests a 3-4 photon absorption for sapphire.

3.6 Two-color pulse pair damage test

3.6.1 Introduction

In sapphire, the relaxation of the electrons from CB is much longer than in fused silica (100 ps versus 100 fs) [41]. Electrons are pumped into the CB with a pump pulse. Free electron absorption and the change in electron density can be probed by a time-delayed probe pulse. Such a technique can be utilized to study the role of avalanche ionization in LID. The studies of sapphire with a time resolved pump-probe technique produced different conclusions [40,41,85]. According to the measurements by Guizard *et al.* [40], it was found that avalanche does not play a dominant role in LID. However, the observation by Karras *et al.* indicated that an intensity dependent avalanche coefficient must be applied to explain the measurements [41].

In these studies, different harmonics of 800 nm were used as the pump beam to

excite the electrons. In [40], the second harmonic 400 nm was used as the pump. After several ps, the 800 nm probes pulse was sent into the samples. Femtosecond pump-probe interferometry was applied to measure the density of electrons. The sample was a cube ($5\times5\times5$ mm^3) and polished on all surfaces. The probe beam was set perpendicular to the pump beam. The measurement of the carrier density was applied at the surface. In [41], the third harmonic at 267 nm was used as the pump. The transmission of the IR pulse was measured as a function of the probe intensity after the excitation by UV pulses of different energies. The sample was 89 μm thick. In the setup, the pump and probe beams were coaxial.

The role of avalanche ionization is still under debate for dielectric materials. Our goal was to check its role in thin film damage. An experiment on a HfO_2 film was set up with a pulse pair. One pulse is at 800 nm (IR) and another is at 267 nm (UV). Both pulses are about 50 fs long. Their separation was set to around 100 fs to avoid interference. The time scale between the pulses is too short for relaxation out of CB to affect the data. For the HfO_2 film, the relaxation time from CB to VB was measured to be a ps scale [64, 84]. The first pulse will excite the electrons from the VB without damage and the second pulse will be absorbed by the CB electrons further through impact ionization to damage the film. The LID tests were conducted under two cases: the UV pulse arrives at the film first and the IR pulse arrives at the film first. The results show that the damage depends strongly on the order of the pulse pair.

3.6.2 Experimental setup

A diagram of the experimental setup is shown in Figure 3.22. The beam from the amplifier was divided into two parts. One was used as a probe beam. The other was used as a pump beam to produce ultraviolet (UV) pulses through a third harmonic

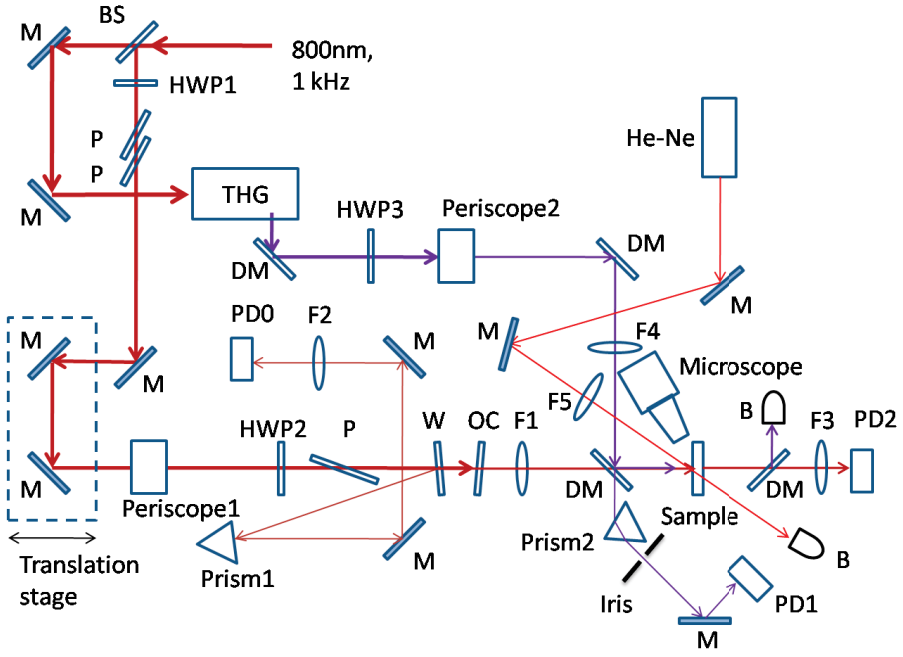

Figure 3.22: Damage test setup with IR and UV fs pulses. BS: beam splitter (Tran./Refl.=70/30), HWP1 and HWP2: half-wave plate for IR, P: ultrafast polarizer, M: mirror, W: fused silica window, OC: ultrafast output coupler, F1: focusing lens f=15 cm, F2: focusing lens f=10 cm, F3: focusing lens f=6 cm, PD0, PD1 and PD2: photodiode, THG: third harmonic generator, DM: dichroic mirror (high reflection for UV, high transmission for IR & Blue), HWP3: half-wave plate for UV, F4: focusing lens f=25 cm, F5: focusing lens f=10 cm, Sample: thin film sample mounted on XYZ translation stage, B: beam blocker.

generation unit (THGU) (see Chapter 2.1.2). Periscope1 consisted of two mirrors to change the beam height. Periscope2 consisted of a prism and a mirror. The prism was placed at Brewster angle for UV. The combination of HWP3 and the prism was used to adjust the UV pulse energy. The reflection from the prism 1 surface was used to reduce the pulse intensity. Prism 2 was used to separate the UV and the IR beams before detection. The central wavelength of the input IR pulses was at 800 nm. The wavelength of the UV pulses was centered at 267 nm. The two pulses were combined with a dichroic mirror and focused on the same spot on the sample. The

pulse duration (FWHM) of the IR pulse before the sample was 54±2 fs. The UV pulse has a pulse druation (FWHM) of about 50 fs before the sample measured by a auto-correlator using self-diffraction.

The beam size was measured using knife edge method for both IR and UV beams. The IR beam radii at the sample position were $w_x = 20.3\ \mu$m and $w_y = 22.2\ \mu$m, respectively. To reach a peak fluence of F=1 J/cm^2, a pulse energy of E= 7.07 μJ was required. The corresponding average power at 1 kHz was 7.07 mW. For the UV, $w_x = 33.7\ \mu$m and $w_y = 31.7\ \mu$m at the position of the sample. To reach a peak fluence of F=1 J/cm^2, a pulse energy of E= 16.8 μJ was required. The corresponding average power was 16.8 mW. Through these relations, the fluence could be obtained from the energy of the IR and UV pulses measured by reference photodiodes.

The procedure used to align the spatial and temporal overlap is outlined in Appendix D.

In the damage test, we needed to check the LIDT with only UV pulses present. A cw 0.5-mW He-Ne laser was used to illuminate the fs pulse excitation area on the sample. The beam radius on the sample was w $\approx 50\ \mu$m. When damage happened on the film, the He-Ne scattering change could be observed by the on-site microscope.

In the two-color damage test, the spatial overlap of the two pulses is critical. The beam profiles of the IR and UV beam were observed in the far field using long focal length lenses. The images were captured by a beam profiler camera (Spiricon LBA-USB L230). The beam profiles of IR and UV are shown in Figure 3.23. For the UV beam, special attention needed to be paid because the beam profile outside the focal plane was distorted. This was not related to the energy of the UV pulse. The exact reason of the distortion was not clear. The shape of the crater produced by UV pulses above LIDT is similar to the beam shape. Therefore, it is helpful to check the crater shape to make sure the beam profile being appropriate at the sample position.

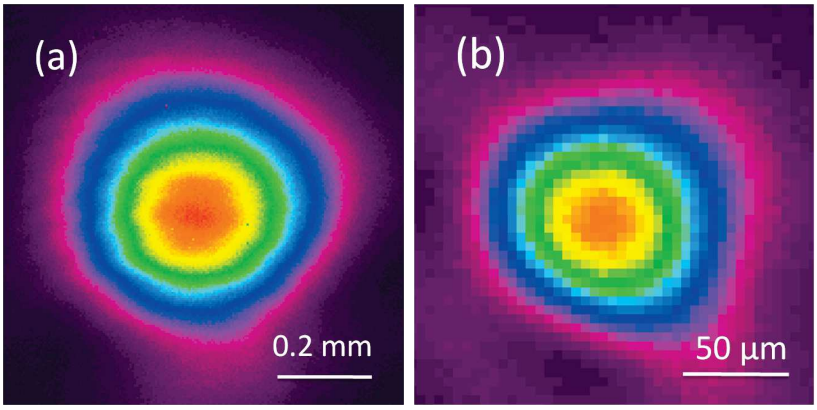

Figure 3.23: IR (a) and UV (b) beam profile images in the far field. The IR beam profile was taken with a f=2.0 m lens near the focus. The UV beam profile was taken with a f=1.0 m fused silica lens near the focus. The colors represent different intensity ranges. From the center of the beam to the outside, intensity decreases along the radius.

The input pulse energy for IR and UV pulses was monitored by calibrated photodiodes. In the damage test, the UV energy was set to several levels. The damage threshold was measured by varying the IR pulse energy for fixed UV pulse energy. Typical shot-to-shot energy fluctuations of IR and UV pulses are 3% and 25%, respectively.

The continuous adjustment of the IR pulse energy was realized by a fine tunable rotation stage for HWP2. As the UV energy was changed, the IR energy needed for damage changed also. Different filter sets were used in front of PD0 to set the output in the range of 0.2 to 2.0 V. A typical calibration curve for IR pulses is shown in Figure 3.24 (a).

For UV pulses, there was a small leakage through the dichroic mirror DM before the sample (see Figure 3.22). Because there was also a small reflection from the IR pulses, a prism was used to separate the two colors. The iris just let the UV beam pass through but blocked the IR beam. PD1 is a silicon photodiode. It did not

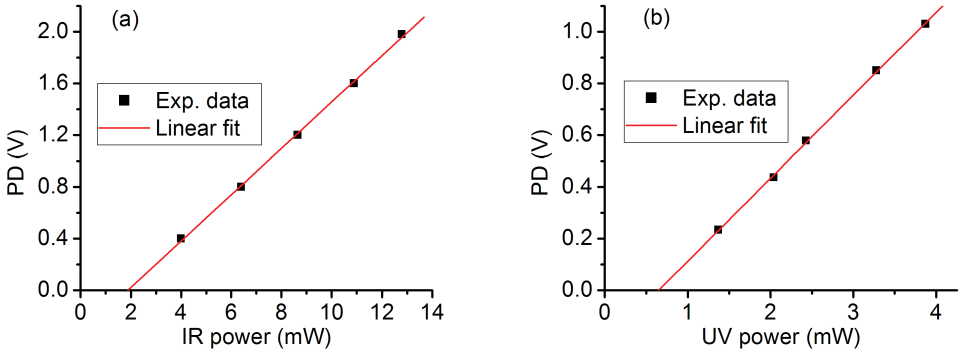

Figure 3.24: Calibration curves for (a) IR and (b) UV pulses. The power was measured before the test sample with a power meter (Ophir PD 300-UV). Each data point is an average over 3 seconds ($\sim$ 3000 pulses). Notice that the fit curves do not pass through (0, 0). This is because there are offsets ($\sim$ -0.24 V) from the PDs output.

respond to 267 nm pulse because it is outside the spectral range (300 nm - 1100 nm). A white card was placed before the detector PD1, which measured the fluorescence of the UV beam. The PD1 output had a linear response with respect to the incident UV pulse energy. A typical calibration curve for UV pulses is shown in Figure 3.24 (b).

3.6.3 Results

The LIDT measurements were done using a HfO_2 film (thickness: 85 nm) ion-beam sputtered onto a fused silica substrate. The MPA orders of the IR and UV pulses are $m = 4$ and $m = 2$, respectively. At each UV energy level, the LIDT with IR pulses was obtained for positive (IR pulse first) and negative (UV pulse first) delay. In each case, the time interval between the UV and IR pulses is $\sim$ 100 fs. The results are shown in Figure 3.25. The error bars along "y" axes (IR fluence) represent the fluence range of damage probability increasing from 0 to 1. The error bars along "x" axes (UV fluence) represent the fluence range of the average of the UV pulses in the

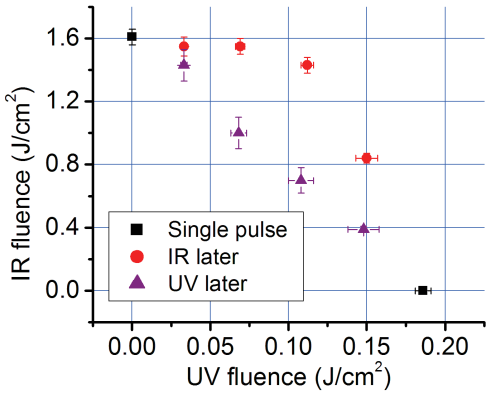

Figure 3.25: Two-color LIDT for a HfO_2 thin film (thickness: 85 nm) on a fused silica substrate. The error bars along "y" axes (IR fluence) represent the fluence range of damage probability increasing from 0 to 1. The error bars along "x" axes (UV fluence) represent the fluence range of the average of the UV pulses in the LIDT measurements.

LIDT measurements.

The results show that the damage threshold depends on the order of the pulse pair, whether the IR or the UV pulse arrives first.

For IR first, the IR threshold fluence as a function of UV fluence follows a linear trend. With the IR fluence increasing, the electron density on the CB increases. The latter UV pulse will excite more electrons from the VB to the CB through impact ionization. The impact ionization is sensitive to electrons accumulated by the former IR pulse. The UV pulse energy to damage the film deceased with increasing IR pulse energy in an almost linear way.

However, the threshold fluence change is quite nonlinear if the UV pulse arrives first. When the UV fluence was increased from 0 to 60% of the single UV damage threshold, the LIDT for IR pulse was only decreased by 11%. With the continuing increase of the UV fluence, the LIDT for IR pulse quickly drops. This demonstrates

that the impact ionization with the IR pulse is different with that with the UV pulse.

In general, when the IR pulse arrives the film first, the film is easier to be damaged by such two-color pulse pair. This observation cannot be explained by impact ionization based on the Drude model. The second pulse is responsible for increasing the electron density to N_{crit}, where $N_{crit} \propto 1/\lambda^2$ (see Chapter 5.3). As a result, $N_{crit}(\mathrm{IR}) \approx 0.1\ N_{crit}(\mathrm{UV})$. Also, the free carrier absorption coefficient $\alpha_{abs} \propto [1 + (\omega/\nu_e)^2]^{-1}$ [49], where ω is the light frequency, ν_e is effective electron collision rate. Assuming an optically thin plasma which is valid at electron densities below dielectric breakdown ($\omega/\nu_e \gg 1$), one can derive $\alpha_{abs} \propto \lambda^2$ [91], which leads to $\alpha_{abs}(\mathrm{IR}) \approx 10\ \alpha_{abs}(\mathrm{UV})$. Considering these two aspects, the pulse pair with UV first should damage the film easier than the IR first. The observation is opposite with the theoretical prediction based on this simple model.

In future work, there are several aspects to be improved. First, improve the beam profile of the UV pulses. The reason why the beam profile was distorted off focal plane needs to be explored. Second, the film thickness needs to be optimized so that the intra-film intensity of the two pulses both have maxima near the front surface of the film. Third, different color combinations, such as SH and fundamental wave, and different dielectric films, like TiO_2 films, should be tested. Appendix E gives a list of the optimized film thickness for HfO_2 and TiO_2 films with different color combinations.

3.7 LID test with different input beam polarization

3.7.1 Introduction

Among the study of the nonlinear physical processes, the role of circular and linear polarization in MPI is an interesting and still open topic. Early work in theory suggested that a strong dominance of circular over linear polarization in MPI [65]. The theory was based on a one-electron atomic system. Perturbation theory predicted that the coupling of orbital momenta was larger for circular polarization, which led to a larger MPI cross section. For higher order MPI, it was predicted that the dominance of circular polarization would increase even more [65]. Reiss suggested that for high order MPI, a reversal of this behavior might be expected [66]. Parzyński derived the complete ratio of probabilities for MPI by circularly and linearly polarized light on the basis of the one-electron model of an atom or ion [92]. Ivchenko *et al.* generalized the predication later to the case of solids [93].

For a hydrogen atomic system, a recent numerical solution of the time-dependent Schrödinger equation shows that the ratio of the ionization probabilities by linear and circular polarization varies with the order, m, of the MPI process [94]. For two- or three-photon absorption, circular polarization produces larger ionization rates. For higher order of MPI, linear polarization is more efficient. The ionization probability is the interplay of two factors: (i) the allowed channels of choosing angular momenta for the electrons in MPI; (ii) the overlap between the initial and final wave functions. The results are consistent with the prediction of Reiss [66] and Parzyński [92].

Some experimental results agree with the theory. In atomic Cesium excited by a ruby laser (λ=694 nm, m=3), circular polarization was found to be more efficient in MPI [67]. For high-order MPI of nitric oxide (m=5 and 6), the dominance of linear

polarization was qualitatively observed [68]. For solids, fs LID studies on bulk fused silica and sapphire (m=6 for both at λ=800 nm) demonstrated linear polarization having significant higher MPA cross sections than circular polarization [42].

However, the published experimental results do not fully agree with the theoretical predictions. In crystalline quartz excited by a Nd laser, four photon-induced photoconductivity experiments suggested that circular polarization still dominated [69]. For thin dielectric films, LID tests with 30-ps pulses at 1.06 μm showed that there was no obvious difference between circular and linear polarization for ZrO_2 (m=6, ratio of thresholds F_{cl}/F_{ll}=1.4-0.76) and MgF_2 (m=10, F_{cl}/F_{ll}=1.0). For TiO_2 film (m=3, F_{cl}/F_{ll}=1.2-1.0) and τ = 30 ps, linear polarization showed a small advantage [43].

From the published results on thin films with single 30-ps pulse, it is hard to tell how the damage behavior is affected by polarization because of the large error bars. The reason for the large error bars may come from the large pulse duration and/or the impurities in the film. Using shorter pulses of a few ps or fs duration, we observe more deterministic damage threshold values [63]. Also, the impact of impurities in today's high-quality films is smaller than what was observed in those earlier experiments. The polarization dependence can thus be studied today with better sensitivity.

Also, from the practical point of view, it is more important to know how the trend goes in S-on-1 tests. The properties for the laser induced mid-states may be revealed through the incubation study. This will help to build the model in explaining the polarization dependence of LID.

3.7.2 Experimental setup

The experimental setup is shown in Figure 3.26. The pulse energy was tuned by half-wave plates (HWP) and thin film polarizers (P). The mirror OC was placed to

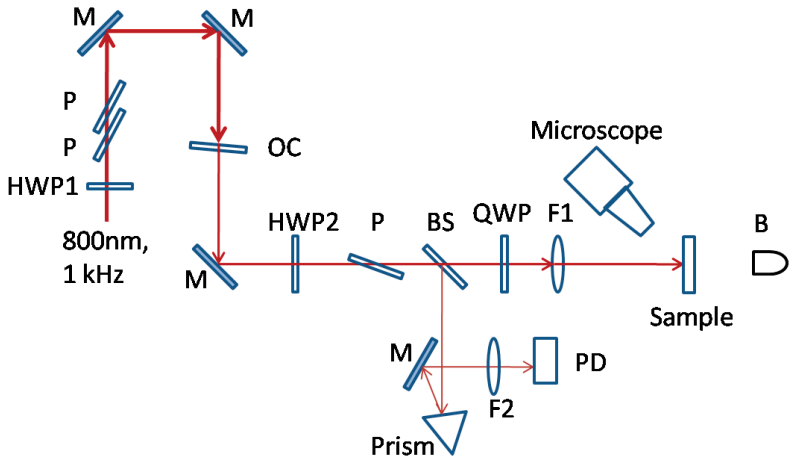

Figure 3.26: Setup for LID test with circular and linear polarization pulses. HWP1, HWP2: half-wave plate, P: ultrafast polarizer, M: mirror, OC: ultrafast output coupler, BS: beam splitter, T=90%, QWP: quarter-wave plate, F1: focusing lens f=17.5 cm, F2: focusing lens f=10 cm, B: beam blocker, PD: photodiode. The reflection from the prism surface was used to reduced the pulse intensity.

reduce the pulse energy (T≈13%). HWP2 was used to finely adjust the pulse energy. Photodiode (PD) monitored the input pulse energy. The beam was focused on the sample at normal incidence.

A quarter-wave plate (QWP) was used to switch between linear polarization and circular polarization. The extinction ratio of the linear polarization is better than 1150. The residual ellipticity of "circular" polarization was smaller than 0.07.

The sample was mounted on a XYZ translation stage. The beam radii were measured around focus along horizontal and vertical directions with the knife edge method. The sample was placed in a plane where the fluence was a maximum. This is similar as in the previous section. The beam radii at the sample were $w_x = 32.2\,\mu$m and $w_y = 28.6\,\mu$m. To reach a fluence of 1 J/cm^2, a pulse energy of 14.5 μJ was needed. Through this relation, the fluence can be obtained from the energy of the IR pulse.

An on-site microscope was used to monitor the scattering change of the film through the amplified stimulated emission (ASE). The camera (Chameleon CMLN-13S2M) has a resolution of 1296×964 pixels. The magnification of the microscope is about 1000.

By tuning the compressor in the amplifier, the pulse duration could be adjusted. In the experiment, damage tests were conducted with pulse duration $\tau = 37$ fs and 0.96 ps.

The samples tested were HfO_2 films (thickness: 216 nm) and TiO_2 films (thickness: 116 nm). In order to decide the spacing of the excitation spots on the sample, we studied the debris distribution with $S = 1000$ pulses at a fluence of 10% above LIDT. The results showed that the probability to probe ablation debris was reduced to less than 1% 115 μm away from the center of the craters. The spacing from spot to spot in our test was set to be 150 μm.

3.7.3 Damage threshold dependence on polarization

The measured damage thresholds versus pulse number are shown in Figures 3.27, 3.28, 3.29, and 3.30. The error bars for the thresholds represent the fluence ranges of damage probability increasing from 0 to 1. In general, the LIDT for circular polarization is larger than that for the linear polarization for the same number of pulses S. The results indicate that for single pulse damage linear polarization is more efficient in exciting electrons in both films. The threshold values for linear polarization are 10% to 20% lower than those for circular polarization.

The tested films, HfO_2 (band gap: 5.1 eV) and TiO_2 (band gap: 3.3 eV) can be excited with MPA of order m=4 and m=3 for pulses at 800 nm, respectively [33]. For 37 fs pulses, the ratio F_{cl}/F_{ll} increases with S for both films. It reaches a plateau at $S \sim 10k$. This is an indication that the laser induced mid-gap states introduced

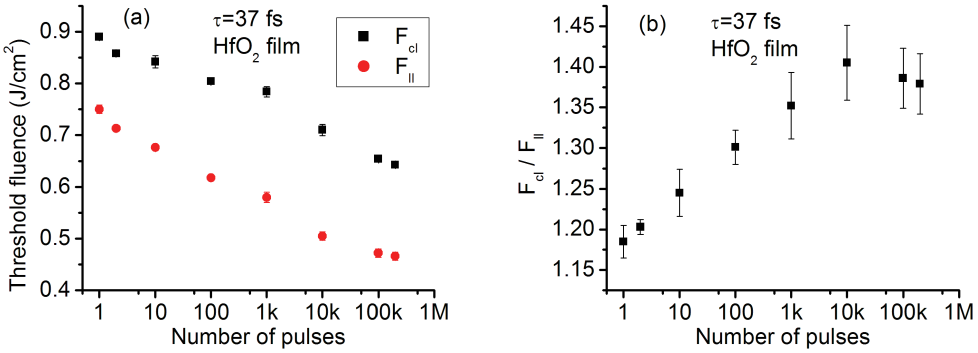

Figure 3.27: (a) The LIDT with circularly polarized light, F_{cl} and linearly polarized light, F_{ll} at different number of pulses S. (b) The ratio F_{cl}/F_{ll} versus S. These results are for HfO_2 films tested with 37 fs pulses at a repetition rate of 1 kHz.

a larger difference in the process of damage between circular and linear polarization. For 0.96 ps pulses, TiO_2 follows the same trend as for fs pulses. But for HfO_2, there is a LIDT drop at $S = 2$. This suggests that there is a production of some mid-gap state which removes the difference between two polarizations. As a result,

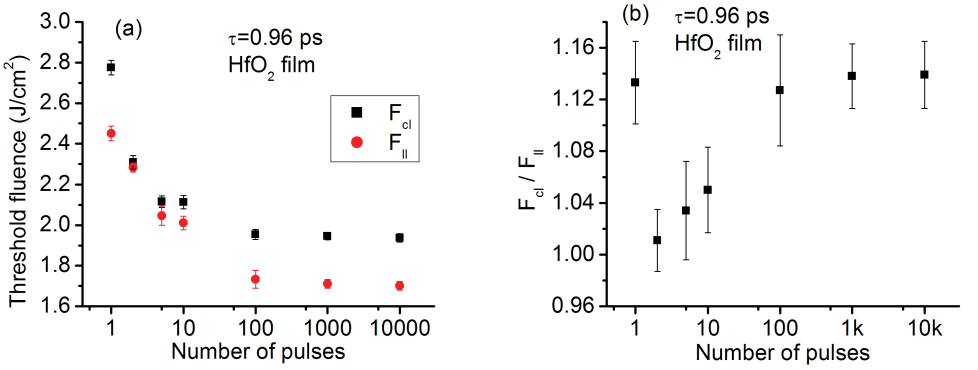

Figure 3.28: (a) The LIDT with circularly polarized light, F_{cl} and linearly polarized light, F_{ll} at different number of pulses S. (b) The ratio F_{cl}/F_{ll} versus S. These results are for HfO_2 films tested with 0.96 ps pulses.

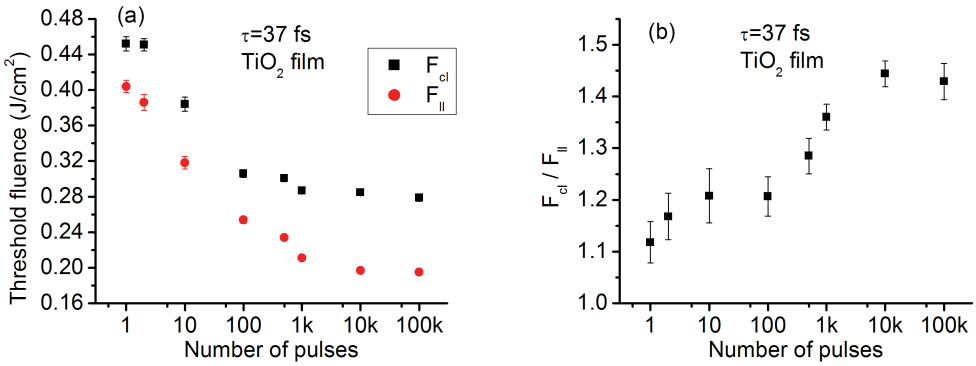

Figure 3.29: (a) The LIDT with circularly polarized light, F_{cl} and linearly polarized light, F_{ll} at different number of pulses S. (b) The ratio F_{cl}/F_{ll} versus S. These results are for TiO_2 films tested with 37 fs pulses.

$F_{cl}/F_{ll} \approx 1.0$ for $S = 2$.

The results provide important information for the physics of incubation and its dependence on polarization for thin film damage. The current model is not sufficient to address the polarization dependence.

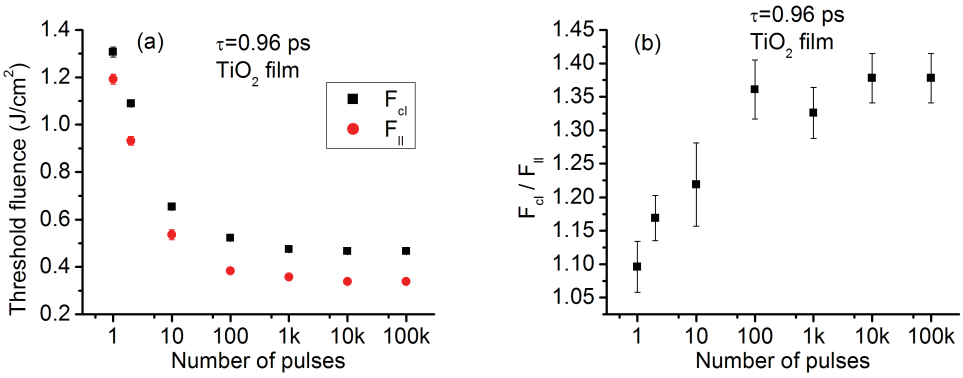

Figure 3.30: (a) The LIDT with circularly polarized light, F_{cl} and linearly polarized light, F_{ll} at different number of pulses S. (b) The ratio F_{cl}/F_{ll} versus S. These results are for TiO_2 film tested with 0.96 ps pulses.

3.8 LID characterization through crater morphology

3.8.1 Introduction

Incubation affects the morphology of the craters in LID. Normally, laser induced periodic surface structures (LIPSS, often termed "ripples") can be observed after the illumination of solids with ultra-short pulses. The directions of the ripples were found to be either parallel or perpendicular to the input laser beam polarization [46].

Two types of ripples are distinguished according to their period. One is low-spatial-frequency LIPSS (LSFL), the other is high-spatial-frequency LIPSS (HSFL). In dielectrics, fs-LSFL often show ripple periods close to the irradiation wavelength λ or λ/n, where n is the refractive index of the material. HSFL have spatial periods significantly smaller than the irradiation wavelength ($\ll \lambda$) [45, 95].

Most of the LIPSS research was done with fs pulses with duration from 15 to 200 fs [45]. Ripples are also observed with ps pulses [96–98] and ns pulses [99].

From the published results, we can differentiate LIPSS produced with fluences well above the ablation threshold and with fluences smaller than the ablation threshold. For the former, LIPSS are quite often found at the bottom of the craters. There are a lot of physical processes involved in the formation of the structures [45, 95, 100–102]. These results are often discussed from the perspective of laser machining. For the latter, the structure will give some finger prints in the LID initial processes, because there is not much material removed by laser pulses. We put our emphasis on the study of LIPSS on thin films.

As for fs LIPSS on dielectric films, Zamfirescu [103, 104] studied ZnO (band gap: 3.3 eV) with 200-fs, 775-nm, 2 kHz pulse trains. The ripples are perpendicular to

the linear polarization direction. The period of the ripples is from 150 nm to 200 nm depending on the input laser fluence. These are HSFL.

Other studied films were made from the following materials, silver [105], Ti [106], photoresist layer [107], indium-tin-oxide (ITO) [108], TiN and TiAlN [109], diamond-like carbon (DLC) [110], $YBa_2Cu_3O_7$ (YBCO) [111] and $CuInGaSe_2$ (CIGS) [112]. References [105, 106, 108, 110] reported HSFL, while references [107, 109, 111, 112] reported LSFL.

In references [110–115], linear and circular polarized pulses were both used. Their effects were compared. In references [110,113], the circular polarized pulses produced dots instead of ripples on the sample surface. In references [111, 112, 114, 115], the left and right circularly polarized pulses produced ripples orthogonal in direction.

In most of the experiments, ripples appeared after multi-pulse illumination of the samples. Even though in reference [109] it was claimed ripples began from the first pulse, the ripples were clearer for multi-pulse illumination.

Most of the articles show ripples at fluence levels close to or above the ablation threshold. At low fluence level and small number (<5) of pulses per burst, the film surface is almost not affected by laser pulses. Only few structures known as pre-ripples are observed in ZnO films [104]. These pre-ripples look like shallow ripples and are distributed randomly on the surface. In reference [105], it is mentioned that when the laser fluence is below the threshold fluence of film breakdown, a textured nanostructure including many nanobumps and nanocavities will appear on the surface of a silver film.

From the theoretical perspective, ripples are in general explained by the interaction of incident laser pulses and surface electromagnetic waves [45, 47, 110, 116]. The roughness of the surface is considered to trigger the surface electromagnetic waves when laser light is incident.

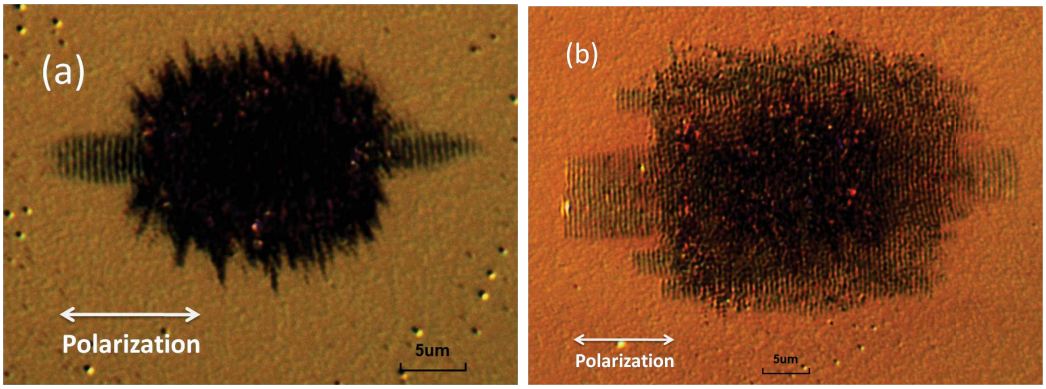

Figure 3.31: Crater images of a HfO_2 film illuminated by a burst of (a) 10 and (b) 10k pulses (τ = 37 fs). The light was linearly polarized. The fluences were above the damage thresholds at $S = 10$ and $S = 10k$, respectively.

The morphology change of films is the direct result from the laser illumination. Can we capture the structure change to help understand the damage process? If so, that will help a lot to connect the theoretical predictions and the real world events.

In order to answer this question, the illuminated spots were checked under an optical microscope after the damage test. Special attention was paid to different damage structures. The incubation effect on crater morphology was explored. Different structures were observed with fluence near and above threshold. They were studied in details with different techniques.

Experimentally, no previous work demonstrated the surface structure change before the ripples were formed. In our tests, we obtained different structures which would help to explain the formation of ripples. This provided experimental evidence for the initiation of ripples in the damage of thin films.

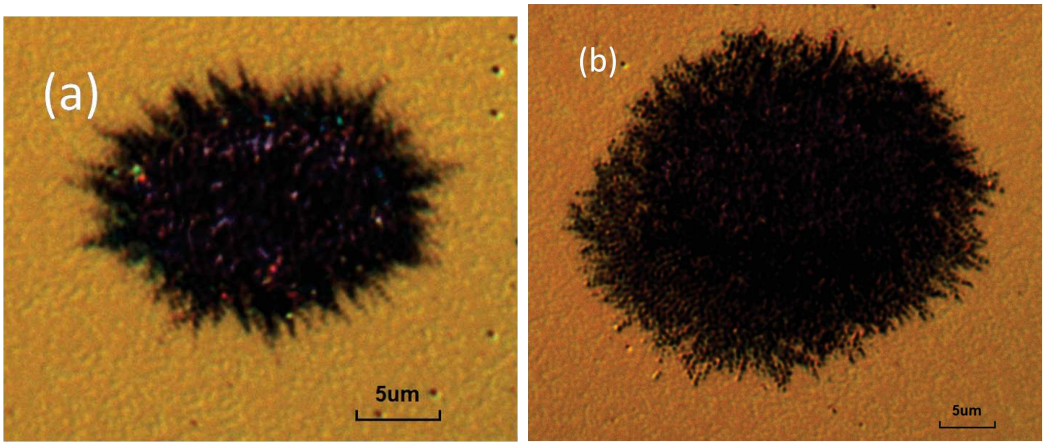

Figure 3.32: Crater images of a HfO_2 film illuminated by a burst of (a) 10 and (b) 10k pulses ($\tau = 37$ fs). The light was circularly polarized. The fluences were above the damage thresholds at $S = 10$ and $S = 10k$, respectively. The reason for the crater shape change may be that the "circular" polarization had a residual ellipticity. The long axis direction was 45^o relative to the horizontal direction. The crater ellipticity along the long axis and short axis increases with S (see Appendix H). This effect was coupled with the original elliptical beam shape. As a result, the crater ellipticity for larger S decreased.

3.8.2 Crater morphology dependence on polarization

After illumination with laser pulses, the HfO_2 sample was inspected with a Nomarski microscope (Olympus BX 60). It showed that the craters looked quite different for linear and circular polarization. For craters produced by linearly polarized multiple pulses, there are clear periodic structures near the crater edge, see Figure 3.31. As mentioned before, these structures are called ripples. The direction of the ripples is perpendicular to the polarization direction. For the craters produced by larger number of pulses, the ripples are longer and cover more area. For the craters produced with circular polarization, there is no clear ripple pattern observed at the edge, see Figure 3.32.

For craters produced with ps pulses, there are no ripples observed for either linear

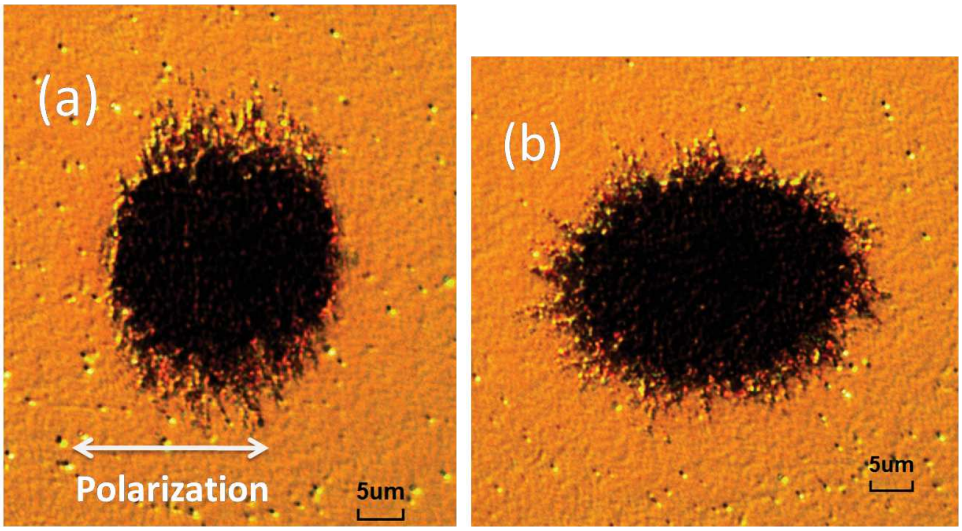

Figure 3.33: Crater images of a HfO_2 film illuminated by a burst of 100 pulses ($\tau = 0.96$ ps). The light was linearly (a) and circularly (b) polarized. The fluence is close to the damage threshold. The change of the crater shape may come from the polarization dependence similar to the observation with fs pulses (see Appendix H).

or circular polarization see Figure 3.33.

3.8.3 Damage process revealed from crater morphology

Except for the craters, there are pure lines and ripples found after the laser illumination at some spots. These structures appeared both for excitation with linear polarization (see Figure 3.34) and with circular polarization (see Figure 3.35). For linear polarization, the direction of the lines and ripples is perpendicular to the input polarization. For elliptical polarization, the direction of the lines and ripples is perpendicular to the long axis polarization (see Appendix F). Although lines and ripples were observed in the pre-ablation condition for elliptical polarization, there is no obvious ripples observed near a crater (see Figure 3.32). This is because the electric field was rotating and the ripples could not be identified in the crater. For

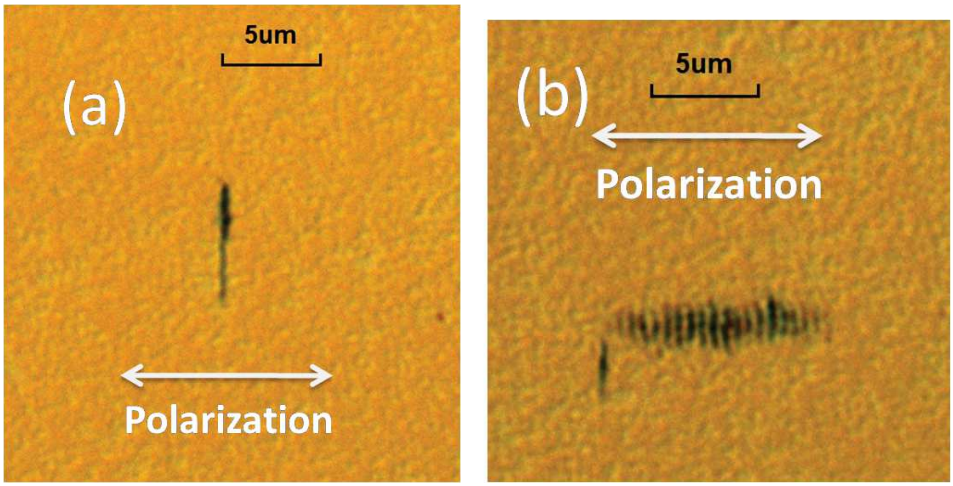

Figure 3.34: Line (a) and ripple (b) structures on a HfO_2 film illuminated by 37 fs linearly polarized pulses, $S = 100$.

ps pulse damage test, there are no lines or ripples found on the sample.

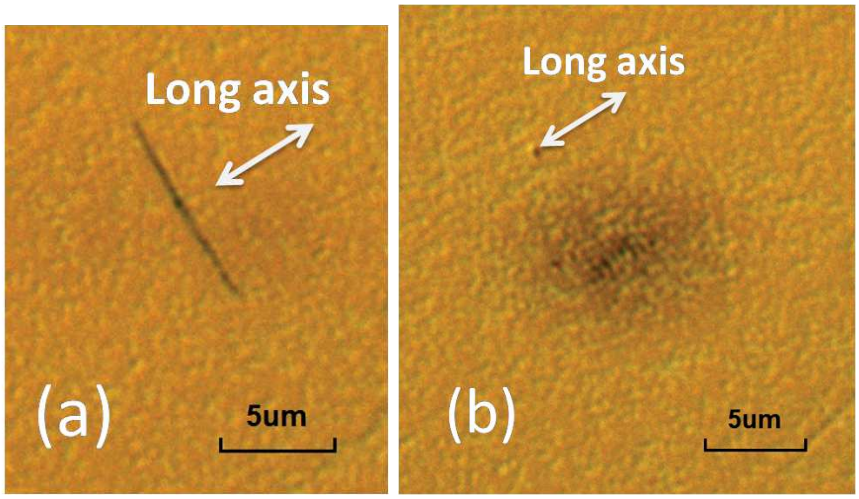

Figure 3.35: Line ($S = 100k$) (a) and ripple ($S = 100$) (b) structures on a HfO_2 film illuminated by 37 fs "circularly" polarized pulses. The residual ellipticity of the "circular" polarization was less than 7%. The direction of the long axis in this elliptically polarized light was about 45^o relative to the horizontal direction.

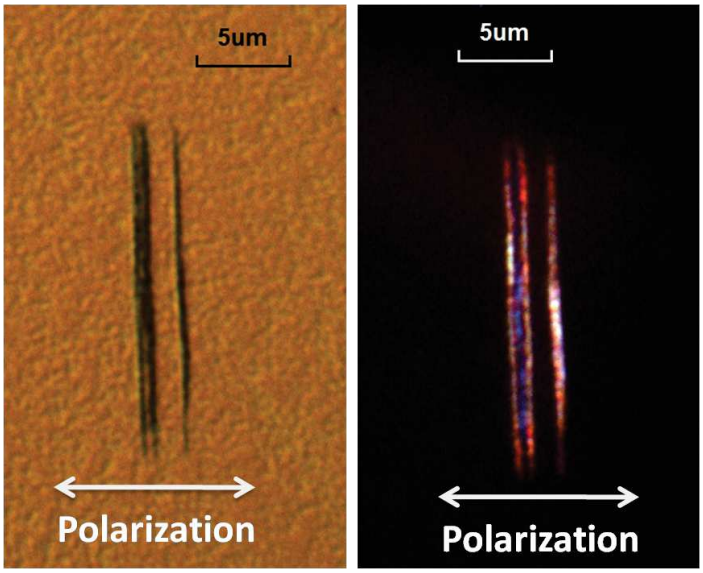

Figure 3.36: Line structures on a HfO_2 film illuminated by 37 fs linearly polarized pulses, $S = 10k$. The Nomarski (left) and the dark field (right) images show a fine structure in one of the main lines.

For the line structure, it could have 1 or 2 main lines. Within one main line, there are fine structures. They may include two or more finer lines, see Figure 3.36. The distance between the main lines varies from 2 μm to 7 μm. It is not an integer of the input wavelength λ (800 nm) or λ/n (380 nm for HfO_2 n=2.09, 550 nm for SiO_2 n=1.45). The distance between fine lines is 0.75±0.15 μm. The length of the lines ranges from 2 μm to 22 μm. The average length of lines increases with the number of pulses.

For the pure ripple structure, the period is around 550±50 nm. It is close to λ/n (550 nm for fused silica substrate SiO_2 n=1.45) . The ripples near the edge of the craters shown in Figure 3.31 have the same period as the pure ripple structure.

In general, we can see clear ripples distributed near the crater edge for fs multiple pulse illumination with linear polarization. For some spots, we even observed craters

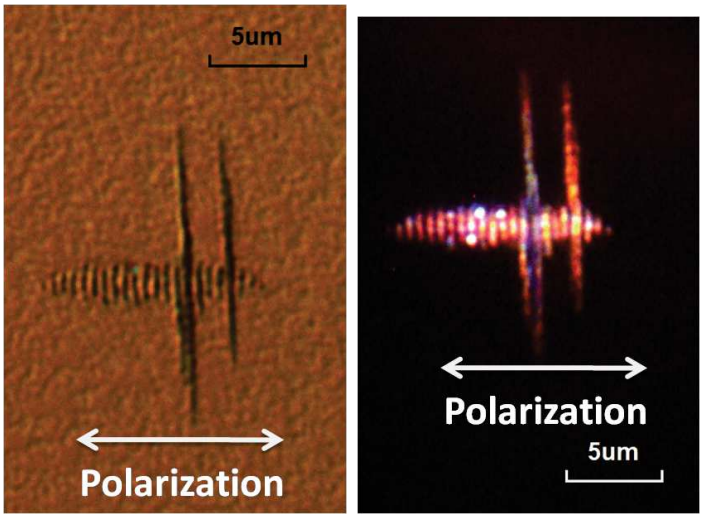

Figure 3.37: Line and ripple structures shown on one spot on a HfO_2 film illuminated by 37 fs linear polarized pulses, $S = 5k$. The left figure shows the Nomarski image and the right figure shows the dark field image.

starting to develop on top of the ripples. While on some other spots, we just observed clean line structures.

In order to clarify the relation between the line structure and the ripples, we used 90% of the damage threshold fluence for 10k pulses to illuminate the films. When the scattering from the film started to change, the input beam was blocked. In most cases, the line structure was observed when the beam was blocked (see Figure 3.36). In some rare cases, we obtained ripples sitting on top of line structures (see Figure 3.37). The lines were much longer than the ripples. If the input beam was not blocked when scattering started to change, a crater was formed.

As we observed from the line structures, the average length of lines increases with the number of pulses. In some cases with illumination by burst of 100 pulses or less, we observed ripples without obvious lines standing out (see Figure 3.34 (b)). This is probably because the length of the line structure is roughly on the same order of

the length of the ripples.

The line structure is quite different from the ripples when observed in a scanning electron microscope (SEM) (see Appendix G). The ripples were also scanned by a photo-thermal microscope (PTM) (see Appendix G). Based on the absorption increase from the undamaged film area to the ripples [117], it is conceivable that damage would happen quickly once the ripples are formed.

From these observations, we can draw a conclusion on the order of the formation of different structures. The line structure was formed first. The ripples followed after the lines. In the end, a crater was formed on top of the ripples.

Theoretically, ripples are explained by the interference of input laser pulse and the surface electron waves [110, 116]. The trigger for this to happen is the surface roughness. From our observation, the formation of the line structure introduced a change in the surface roughness, which leads to the development of ripples. The line structures may be caused by some defects in films.

Similar tests were conducted using fs circular polarization pulses. It was found that no line structure or ripples could be identified after blocking the incident pulses. Once the scattering pattern started changing, a crater was quickly formed. The change of structures was much faster than that with linear polarization.

By comparing the damage threshold defined by the appearance of normal craters and including both line structure and normal craters , it is found that the damage thresholds are almost the same (see Figure 3.38 (a)). There is no indication that line structures appear at a lower fluence level. Also, by changing the number of pulses at a specific fluence level, there is no indication that the line structure starts to happen at a specific number of pulses (see Figure 3.38 (b)).

From the morphology study, the order of structure change in thin films was revealed: first lines, and then ripples, and a crater in the end. These structures were

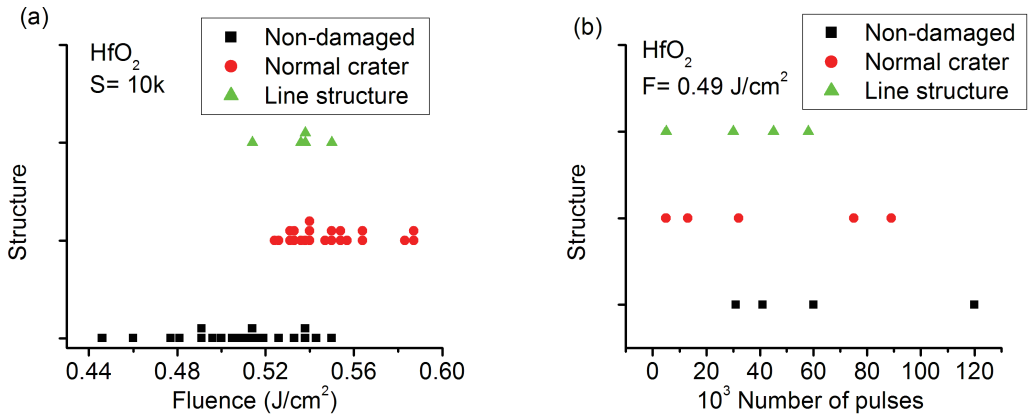

Figure 3.38: (a) Summary of the observed structure of the illuminated spots as a function of the pulse fluence for a specific number of pulses, $S = 10k$ on a HfO_2 film ($F_{th} = 0.54$ J/cm^2). (b) The structure status as a function of the number of pulses at a specific input fluence, $F = 0.49$ J/cm^2. There were no observation of only ripple structure in these damage tests.

experimentally demonstrated. The surface roughness introduced by lines caused the initiation of ripples in thin films. This is new as far as we know in the exploring of the damage processes.

3.9 Chapter summary

In this chapter, we discussed modifications and damage of some dielectric materials with laser pulses. The samples were bulk materials and thin films.

LID tests were conducted on thin HfO_2 and Sc_2O_3 films with 375 ps and 13 ns pulses. Combined with the results with fs and ps pulses, our damage model was applied to pulse durations that vary over almost six orders of magnitude. It was found that the model can be applied to damage with ps and ns pulses for nascent films if a suitable time constant for relaxation out of CB is chosen.

The presence of mid-gap states was verified by the pulse pair (2-on-1) test. The relaxation to the mid-gap states is on a time scale of tens ps to ns for Sc_2O_3 films and agree with the results from the LID measurement data for different pulse durations.

The difference between single pulse and multiple pulses MPA coefficients was clarified. Within a pulse train of 1000 pulses, the transmittance of each pulse was measured at different input pulse fluence levels. For fused silica, the results fit well with a six-photon absorption process. The effect of incubation on the MPA coefficient is demonstrated. For $S = 1000$, the MPA conefficient is increased by 16% compared to $S = 1$. For sapphire, although it has a similar band gap as fused silica, a three- to four-photon absorption fitted the results best. This is likely caused by the mid-gap states.

The LID test with two-color pulse pairs showed that the damage threshold depends on the order of the pulse pair, that is, whether the IR or the UV pulses arrive first. It presents evidence of the frequency dependence of impact ionization. For future work, necessary improvements on the setup and samples were discussed.

The LIDT dependence on the input pulse polarization was explored. LIDT versus numbers of pulses were measured for HfO_2 (m=4) and TiO_2 (m=3) films with different input polarizations. The damage tests were conducted with two pulse durations, 37 fs and 0.96 ps. Linear polarization has lower LIDT than circular polarization.

Incubation affects both the LIDT and the morphology of the illuminated "damage" spots. The damage processes were discussed from the perspective of structure change through the observation of craters in the tested HfO_2 films. During exposure to a pulse train, line structure appeared first, followed by ripples, and a crater in the end.

The results presented in this chapter were published in [63, 81, 117].

Chapter 4

Empirical incubation law for laser damage and ablation thresholds

4.1 Introduction

4.1.1 Literature review and open questions

Laser induced ablation and damage has been an active research area for over 50 years. This topic was presented soon after the appearance of laser (see the introduction to Chapter 3). The onset of laser ablation and laser damage are governed by the same physical principles although one is usually intended, for example for material processing (see References [118, 119] for reviews), and the other to be avoided (see References [28, 120] for reviews). The determination of threshold fluences and intensities are important for dimensioning laser processing (structuring) systems and to mitigate the catastrophic failure of optical components [121]. While the actual physical mechanisms depend on material parameters and type (metal [122], semiconductor [123], dielectric [90] etc.) and the illumination (wavelength [124], pulse

duration [125], repetition rate [49]), common characteristics exist and can be explained with phenomenological approaches.

Laser processing of metals and dielectric materials, unlike mechanical techniques, is not affected by surface hardness, which makes it attractive. To first order the critical illumination parameters for metal ablation depend on the absorption (skin) depth and the specific energy needed to vaporize the material if the excitation pulses are shorter than characteristic heat diffusion times [126]. In dielectric materials, the energy deposition proceeds through a multiphoton ionization process and absorption by the generated carrier plasma [28].

Ablation thresholds are usually defined in terms of the lowest fluence and intensity required to remove material (in the limit - a single atom). Determination of thresholds are typically performed by inspection of the illumination sites with a microscope or by detecting changes in the scattering pattern produced by a probe laser [121]. Care must be taken to define clearly what threshold means and that the applied diagnostic techniques are suitable.

Single-shot ablation (or damage) thresholds (1-on-1 tests) are frequently determined by measuring the crater diameter as a function of pulse fluence F. Linear extrapolation of a plot of the crater area A versus $\ln(F_0)$ yields the threshold fluence F_{th} at $A = 0$ [48]. The validity of this approach can be shown easily assuming a Gaussian excitation beam of waist w and postulating that ablation occurs within a crater of radius R (area $A = \pi R^2$) for which the local incident fluence $F_0 \exp(-2R^2/w^2) \geq F_{th}$. The radius of the crater,

$$R^2 = \frac{1}{2} w^2 \ln\left(\frac{F_0}{F_{th}}\right). \tag{4.1}$$

The advantage of this technique is that the measurements can be performed at fluences well above threshold for which the detected fingerprint signals are clearly detectable by far-field microscopy. Also, the beam waist w_0 does not have to be

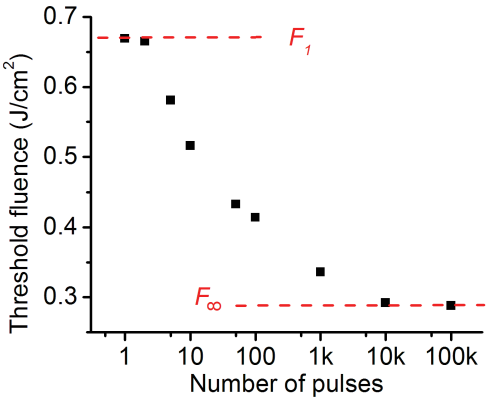

Figure 4.1: Typical incubation curve showing decreasing threshold fluence for larger pulse numbers. The data were taken with a 1-kHz, 55-fs Ti:sapphire laser and TiO_2 thin films.

known; it is obtained as the slope of the regression line.

It is well established that the critical fluence, F_{th}, depends on the number S of pulses exciting one and the same spot (S-on-1 test). This phenomenon is often referred to as material incubation [49]. In most cases, the threshold fluence decreases with S starting from the single-shot ablation threshold F_1, before it remains constant for $S > S_c$. If the fluence is below the so defined multiple pulse threshold F_∞, ablation or damage does not occur for any number of pulses. Figure 4.1 shows a typical incubation curve and indicates the single-shot threshold F_1 and the saturation value F_∞. There are also examples where F_{th} increases with S, which is known as laser conditioning and is advantageously used when ramping up the power of high-power laser systems.

An early attempt to model the incubation behavior of the threshold fluence $F_{th}(N)$ was published in 1988 [50]. Here, the authors use a single incubation pa-

rameter S that is derived from the following equation:

$$F_{th}(S) = F_{th}(1)\, S^{P-1} \tag{4.2}$$

where $F_{th}(1)$ and $F_{th}(S)$ are the ablation threshold fluences for a single pulse and for S pulses, respectively. For the most common case of incubation, the lowering of the ablation threshold with every laser pulse on the same spot, the parameter P is confined to $0 < P < 1$. For $P = 1$, the LIDT does not depend on the number of applied pulses. This model was successfully used to fit incubation in different material groups like dielectrics [127, 128], glass [129], thermoplastics [130], metals [131–133], polymers [134], and semiconductors [132], to name just a few examples. The incubation parameter P was estimated in numerous other publications and widely used to compare the incubation behavior of different materials.

A major drawback of equation 4.2 is that the ablation fluence does not saturate for large S, which is experimentally observed (see Figure 4.1). Ashkenasi *et al.* [51] accounted for the convergence at large S by using an exponential function and an empirical fit parameter k:

$$F_{th}(S) = F_{th}(\infty) + [F_{th}(1) - F_{th}(\infty)]\, e^{-k(S-1)} \tag{4.3}$$

Although this model accounts for the convergence of the damage threshold with large pulse numbers it does not explain more sophisticated incubation curves that are common.

For dielectrics, this was achieved by physical models that link incubation to properties of the particular material. The occupation of existing and the creation of laser induces defects are accountable for the increase of absorption and the lowering of the LIDT for subsequent pulses [52]. With some simplifying assumptions, the multiple pulse damage threshold of dielectric materials can be written as

$$[F_{th}(S)]^m = [F_{th}(\infty)]^m + [(F_{th}(1))^m - (F_{th}(\infty))^m] \times \left(1 - \frac{T_1}{T_2}\frac{n_1}{n_2}\right)^{S-1} \tag{4.4}$$

where m is the order of the multiphoton absorption process for excitation. The last term in braces controls the asymptotic approach $F_{th}(S) \to F_{th}(\infty)$. It is determined by the ratio of band-to-band relaxation time T_1 and the creation time T_2 of absorbing midgap states, and by the ratio of the electron density generated by a single pulse, n_1, and the maximum density of trap states, n_2.

Employing computer simulations, physical processes during pulse excitation and between pulses can be treated in detail. This procedure is particularly successful in describing rather complex incubation curves in dielectric materials and the dependence of the LIDT on the laser pulse duration [34] and intrinsic material parameters. Measurements of $F_{th}(S)$ reveal information about the detailed material response to pulsed excitation and its transient behavior.

To describe incubation for a larger class of materials - dielectrics, metals and possibly semiconductors – based on physical processes, we establish a phenomenological approach taking into account two major components of material incubation. While this model lacks the rigor of those described before [34, 52], it is based on physical processes known to control the material response.

While the crater size technique has also been applied to multiple pulse (S-on-1) measurements, it is not a priori clear whether this method is applicable. Note the incubation itself becomes radius dependent. Our model will be applied to assess the validity of the crater size method to determine multi-pulse thresholds $F_{th}(S)$ and to compare incubation in metals and dielectric materials.

From the experimental point of view, it is important to verify whether the crater size method gives the same results as other methods, such as on-site scattering change method. The relationship between the thresholds using the crater size method and using other methods will indicate the incubation effect on the crater size. Also, it is worthwhile to know if the required conditions for this method is valid in the LIDT

measurements.

Since bulk metal surfaces usually have much more scattering than thin dielectric films, using an on-site microscope does not help to identify the ablation threshold by scattering pattern change. The ablation thresholds are often obtained using the crater size method. It is meaningful to explore and develop other potential methods to determine the ablation thresholds, such as using the plasma emission from the excited metal surface.

Main parts of this chapter are being published in [135, 136] and the research was performed in close collaboration with Dr. Matthias Lenzner. This chapter is based on a paper submitted to Journal of Applied Physics [136].

4.1.2 Chapter goals

Here are the goals of this chapter:

- Study the relationship between LIDTs of thin dielectric films obtained using the scattering pattern change method and the crater size method.

- Explore the method using plasma emission to determine ablation thresholds of metals and compare this technique with the crater size method.

- A phenomenological model will be introduced to describe incubation for dielectrics and metals. The measured incubation curves will be fit with this model. Conditions under which the crater size method can be used will be discussed.

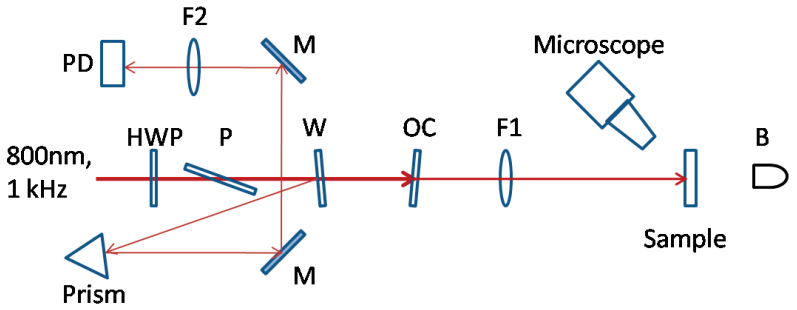

Figure 4.2: Experimental setup for fs IR damage tests of TiO_2 films. HWP: half-wave plate, P: ultrafast polarizer, W: fused silica window, OC: ultrafast output coupler, F1: focusing lens f=15 cm, B: beam blocker, M: mirror, F2: focusing lens f=10 cm, PD: photodiode. The reflection from the prism surface was used to reduce the pulse intensity.

4.2 Using crater size and scattering change methods to measure LIDTs of dielectric films

4.2.1 Experimental setup

To compare the S-on-1 damage thresholds determined by the on-site scattering change method and the crater size method we set up an experiment to test TiO_2 films. The 800-nm pulse duration before the sample was 55 ± 3 fs (FWHM). The beam size was measured using the knife edge method near the focus plane. The sample was placed in the plane of the highest fluence.

The diagram of the damage test setup is shown in Figure 4.2 . The scattering change on the film was monitored by an on-site microscope using the ASE from the Ti:Sapphire amplifier. The sample was mounted on a 3-D translation stage. In the test, the sample was moved laterally with 150 μm spacing between spots. The spacing between columns was 200 μm.

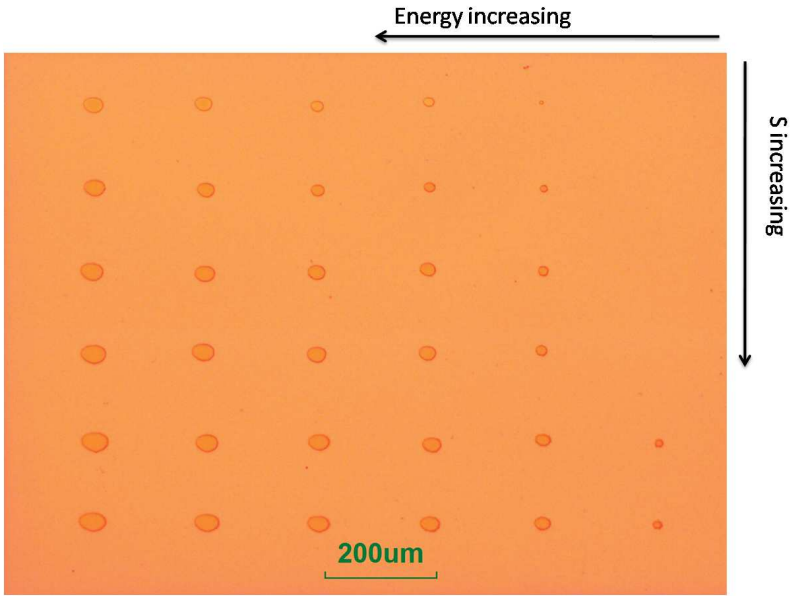

Figure 4.3: A Nomarski image of the damage/ablation crater matrix on a TiO_2 film. In the pattern, each column is illuminated with the same laser pulse energy. The number of pulses (S) on each spot is increased from the top to the bottom. The pulse energy is increased from the right to the left. On the first column from right, the pulse energy is too low to produce craters on the first four spots from the top ($F < F_{th}$).

For the crater size measurements, a matrix of craters was produced on the sample with the number of pulses (S) changing within a column and the energy of the pulses changing along a row. The spacing of the craters was kept the same as in the scattering change damage tests. A Nomarski image of the crater matrix is shown in Figure 4.3.

4.2.2 Results

Typical crater images of the film are shown in Figure 4.4. All the crater images were taken with a Nomarski microscope unless stated otherwise. For small number

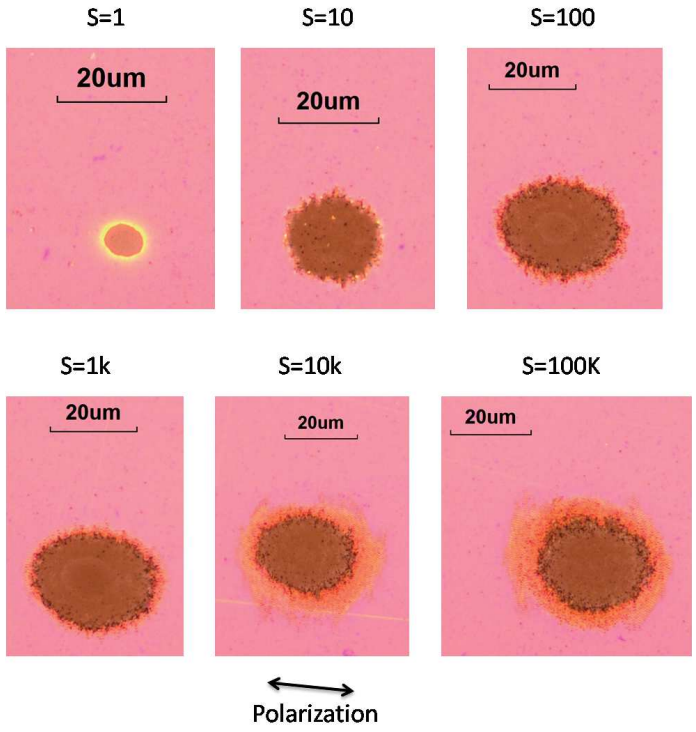

Figure 4.4: Typical crater images from a Nomarski microscope of TiO_2 films damaged with different number of pulses S. The fluence was 0.7 J/cm^2. The long axis direction of the elliptical craters was along the polarization of the incident light.

of pulses ($S \leq 1000$), there were no obvious ripples near the crater edge. For large number of pulses ($S > 1000$), clear ripples were observed near the crater edge. These ripples were part of the damaged coating. They were included as the crater size was measured. However, with the presence of the ripples, the crater size for large S fluctuated more than for small S. Therefore, for each energy level, there were five craters produced under identical conditions and averaged to get the crater size for $S > 1000$.

Figure 4.5 shows the change of crater area with pulse fluence on a semi-log scale. According to Equation 4.1, the linear fit of Figure 4.5, will give the threshold $F_{th}(S)$ by extrapolating the fit to zero area. The damage threshold results are shown in

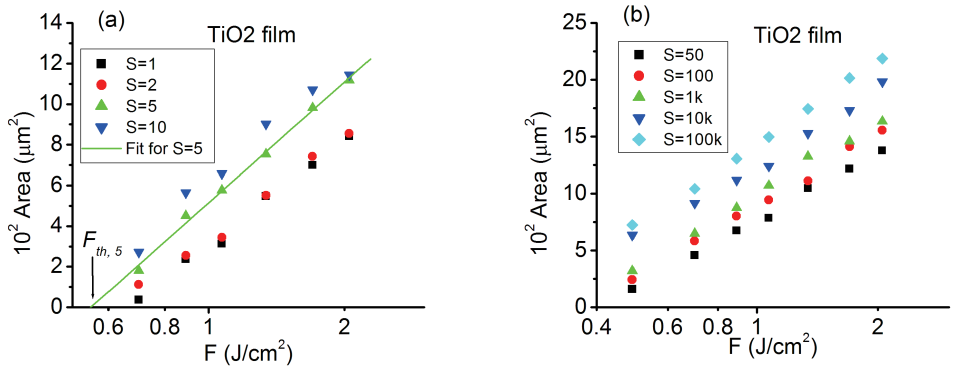

Figure 4.5: The crater area as a function of fluence (on ln scale) for different S. For S =1 to 1000, each data point for the area was obtained from one crater spot. For $S = 10^4$ and 10^5, each data point for the area is an average over five craters.

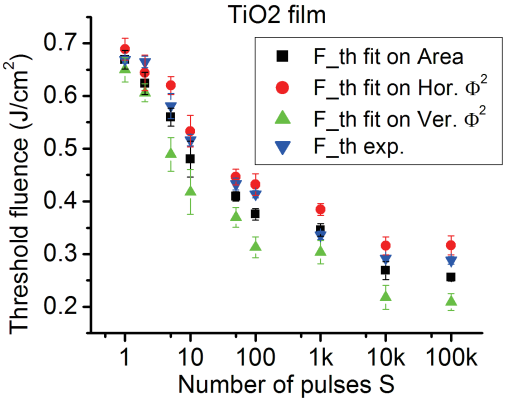

Figure 4.6: LIDTs of TiO_2 films from two methods: on-site scattering change method (F_th exp.) and crater size method (F_th fit on Area). The incident beam polarization is along horizontal direction. The "LIDTs" along horizontal (F_th fit on Hor. Φ^2) and vertical axes (F_th fit on Ver. Φ^2) were obtained using the diameter square vs $\ln(F_0)$ for the horizontal and vertical axes of the ellipse. For a specific number of pulses, $F_{th}(S)$ along horizontal direction is always bigger than that along vertical direction.

Figure 4.6. We see that the damage threshold values obtained from the crater area method are in agreement with those obtained from the scattering change method.

The craters show an elliptical shape (see Figure 4.4). By fitting the diameter square along the horizontal and vertical direction separately, we can see that the threshold along horizontal direction is always higher than that along vertical direction at a specific S (see Figure 4.6). A detail description about the crater shape dependence on the input polarization direction is shown in Appendix H.

The direction of the ripples of TiO_2 films is different than that of HfO_2 films. On HfO_2 films, the direction of the ripples is strictly perpendicular to the input beam polarization direction (see Section 3.8). On TiO_2 films, the ripples do not follow one specific direction (see Appendix H). The main direction of the ripples is parallel to the input beam polarization direction. From the literature, the directions of the ripples were found to be either parallel or perpendicular to the input laser beam polarization for different materials [46].

4.3 Using crater size method to measure LIDTs on bulk metals and metal films

4.3.1 Experimental setup

A diagram of the experimental setup is shown in Figure 4.7. The applied pulse energy (2 mJ maximum) was so high that an air plasma was formed near focus. The pulse duration was optimized to the shortest with the brightness of the super continuum from the air plasma. The pulse duration of the 800-nm laser before the metal is 37 fs (FWHM). The metal plate (76 mm $\times$ 76 mm) was placed before the focal point to avoid the air plasma. The distance from the lens (f=30 cm) to the

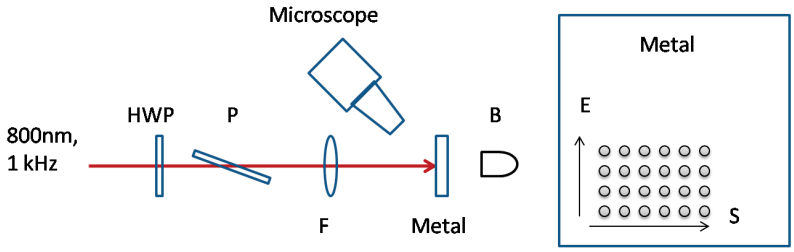

Figure 4.7: Experimental setup for fs metal ablation tests. HWP: half-wave plate, P: ultrafast polarizer, F: focusing lens f=30 cm, B: beam blocker. The metal plates are mounted on a XYZ translation stage. On the right side, a crater matrix pattern is shown. The spacing between columns and rows is 2 mm.

metal was 26.0 cm. The pulse energy was adjusted using the half-wave plate. The on-site microscope was used to monitor the surface to avoid obvious scratches in the metal surface.

The plate was raster scanned. Pulse energy (E) and number of pulses (S) were varied along column and row direction separately, see Figure 4.7. The spacing between spots were 2 mm along both directions. Three samples (bought from McMaster-Carr) were tested under the same condition: Nickel super alloy 625(1-mm thick), stainless steel A286(1-mm thick)and Aluminum 6061(2-mm thick). The surface of these metal plates was unpolished. Before tests, the metal surface was cleaned with acetone solution.

The beam size at the sample position was measured using knife edge method (w_x= 377 μm; w_y= 311 μm.). The fluence was calculated from the measured pulse energy. The corresponding pulse energy for fluence $F = 1$ J/cm^2 is $E = 1.84$ mJ .

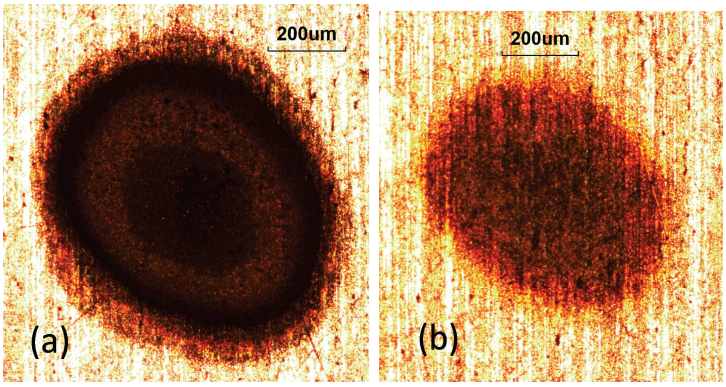

Figure 4.8: Typical images of the ablated area on Nickel alloy: (a) S=1k, crater depth d=30 μm; (b) S=5, no obvious crater, only discoloration observed. The laser fluence for both spots was the same, $F = 1.09$ J/cm^2. The images were taken with a NA=0.15 objective. The crater depth was measured using a NA=0.80 objective.

4.3.2 Ablated area characterization

The size of the ablated area was measured under an optical microscope (Olympus BX 60). At the same time, the depth of the craters was also measured using high-NA reflective microscopy. The minimum depth measurable with the microscope is about 1 μm. The typical images of ablated area on Nickel alloy are shown in Figure 4.8. The images shown in this section were taken by a bright field microscope unless mentioned otherwise.

For large S and high fluence F, the range of the ablated area includes the discoloration region around the obvious craters at the center (see Figure 4.8 (a)). As S and F decrease, the craters become less visible. Until some point, only discoloration is observed without obvious craters (see Figure 4.8 (b)). At even lower S and F, no obvious change is observed on the sample surface. According to literature [137, 138], the discoloration around the craters is shallow ablation of the metals with the depth on the order of tens to hundreds of nanometers.

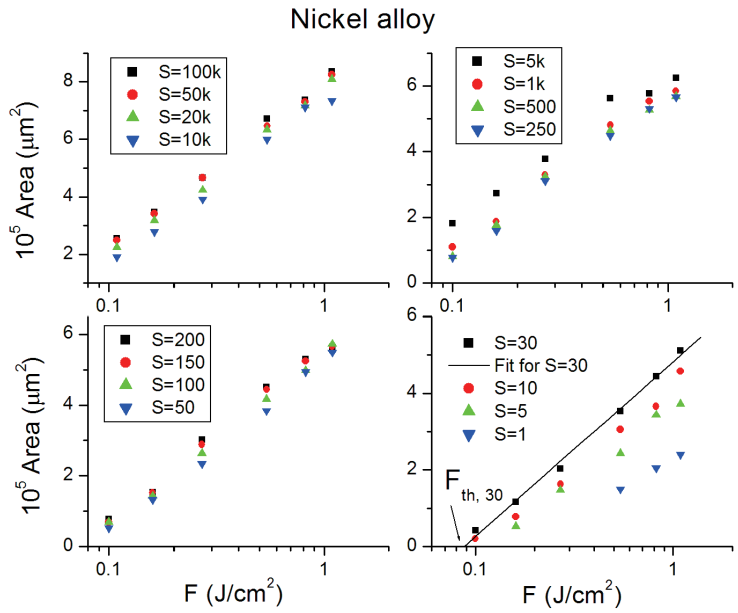

Figure 4.9: The ablated area as a function of the input pulse fluence for different number of pulses S for Nickel alloy. Notice that the fluence is on ln scale. A linear fit extrapolated to Area=0 yields F_{th}.

Therefore, in the determination of the diameter of the ablated area, the boundary includes the discoloration. The area of the ablation is determined using $A = 0.25\pi$ $\Phi(x) \cdot \Phi(y)$, where $\Phi(x)$ and $\Phi(y)$ are the diameters along the long axis and the short axis for an elliptical shape.

4.3.3 Results

Bulk metals

The ablated area as a function of the fluence is shown in Figure 4.9. By fitting the experimental results with linear curves on the semi-log figures, the ablation threshold fluences were obtained from the extrapolation to area being zero, see Figure 4.10. We

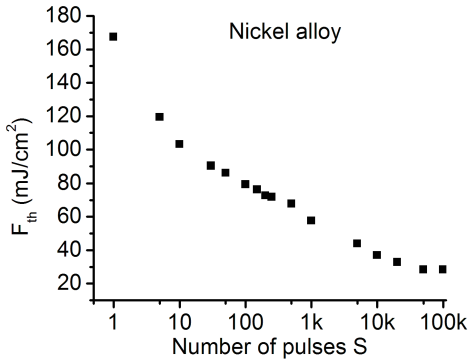

Figure 4.10: Threshold fluence as a function of the number of pulses for Nickel alloy.

assumed here that the beam profile was elliptical. The threshold fluences decrease with the number of pulses and are then constant for $S \geq 50k$.

Aluminum shows different results. The ablated area measurements of Aluminum are shown in Figure 4.11 and the threshold fluence results are shown in Figure 4.12. $F_{\text{inf}} = F_{th}(S \geq 5000)$.

Thin films

As a comparison, the damage threshold of an Aluminum film was measured using the scattering change method. The sample was a UV enhanced mirror from Thorlabs (PF10-03-F01). Above the Aluminum film was a thin layer of MgF_2 around 100-nm thick, which could be neglected in this laser damage experiment because its LIDT ($F_{th,1} = 1.84$ J/cm^2 with 100 fs laser pulses at 800 nm [139]) was much higher than Aluminum . The thickness of the Aluminum film was around 1 μm. The experimental setup used here was the same as for the TiO_2 damage test cf. Chapter 4.2. $F_{th}(S)$ of the film is plotted together with the bulk Aluminum, see Figure 4.12, for comparison. In general, $F_{th}(S)$ is higher in the film than in the bulk. The main reason for the

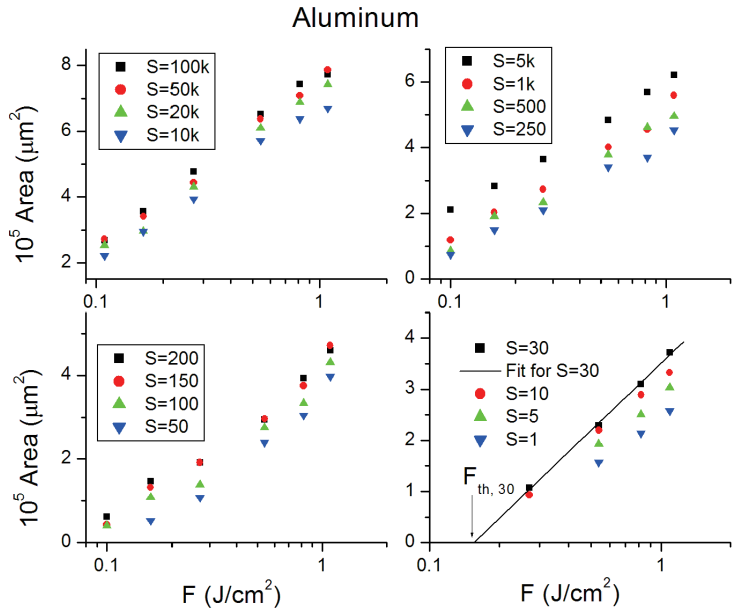

Figure 4.11: The ablated area as a function of the input pulse fluence for different number of pulses S for Aluminum. Notice that fluence is on ln scale. A linear fit extrapolated to Area=0 yields F_{th}.

difference is likely the large surface roughness of the bulk. The effective exposed area is proportional to the surface roughness. Increasing the exposed area will increase the number of defects and impurity levels. As a result, LIDT decreases with the increase of the surface roughness [140].

A question of practical interest is the aspect ratio of the holes that can be drilled with ultrashort pulses. The results about the depth of holes using different beam sizes are shown in Appendix I. Through the linear relationship between the hole depth and the number of pulses S, the depth for single pulse ablation was extrapolated. For metals, the depth for single pulse is on the order of the skin depth for the incident light. As for the energy needed for ablation, it is close to the energy needed to sublimate the illuminated volume. The theoretical estimations and the experimental

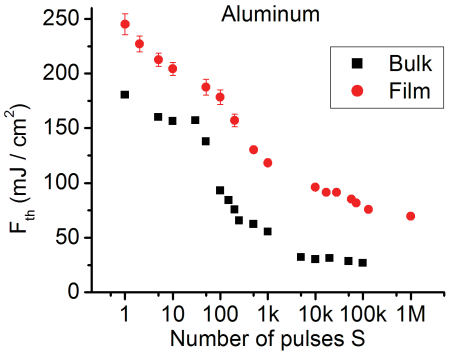

Figure 4.12: Characteristic curves $F_{th}(S)$ for Aluminum film and bulk for comparison. The "error bar" for the film is the range of fluences corresponding to damage probability from 0 to 1.

results are listed in Appendix J.

4.4 Measurement of the ablation threshold using plasma emission

In order to explore other methods to get the ablation thresholds for small number of pulses (S <100), we tried several ways: the scattering of 800 nm input pulses from the metal surface, the scattering of a reference cw He-Ne at the center of the ablation area, and the scattering of an air plasma emission at 633 nm from the metal surface. It was found the plasma emission was the most sensitive among them.

4.4.1 Setup

The experimental setup for measuring the plasma emission is shown in Figure 4.13. In this experiment, several photodiodes were added to the ablation test setup (see Figure 4.7). A silicon photodiode (PD1) was used to measure the input pulse energy for each pulse. With the pulse energy close to the ablation threshold, the

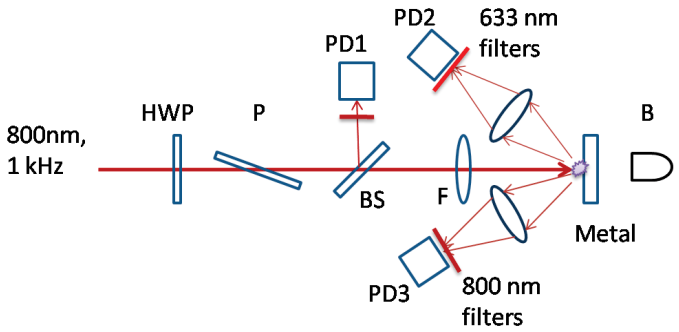

Figure 4.13: Experimental setup for measuring 633 nm plasma emission from metal surfaces. HWP: half-wave plate, P: ultrafast polarizer, BS: 90(T):10(R) beam splitter, F: focusing lens f=30 cm, B: beam blocker. PD1: reference photodiode for the input pulses, PD2: photodiode for 633 nm emission, PD3: photodiode for scattering of the input pulses.

plasma emission was much weaker than the scattering of the main pulses. A sensitive avalanche photodiode (ThorLabs APD 110A2, wavelength range: 200-1000 nm) was used to pick up the plasma emission. To suppress the scattering of the main pulses, two narrow filters at 633 nm and a 0^o 800 nm mirror (high transmission for 633 nm) were placed before PD2. The laser illuminated spot was imaged onto PD2 through a lens (f=6 cm). The scattering of 800 nm pulses was imaged through a lens (f=3.5 cm) onto PD3 (ThorLabs PDA 400, wavelength response: 800-1750 nm). Neutral density glass filters were inserted before the photodiodes.

The assumption for this method was that the plasma emission from the surface was directly related to the metal removal by laser pulses. $F_{th}(S)$ was defined as the plasma emission began to appear for pulse S in a train of pulses. There are two ways to find $F_{th}(S)$: (1) Adjust the input pulse fluence to find out the threshold fluence at which the plasma emission starts from the S pulse. This way requires a low noise level. (2) Use different fluences above the threshold to obtain the corresponding emission signals, and extrapolate the signal to zero plasma emission. Using this way can reduce the affect of the noise on the determination of F_{th}. In our measurements, we used the second way. For Nickel alloy and stainless steel, at fluence above the threshold, the plasma emission increased from the first pulse, it reached a maximum at $S \sim 30$. And then it dropped gradually. For Aluminum, the drop started after only several pulses ($S \approx 3$). In the experiment, we chose the first 30 pulses on Nickel alloy and the first 20 pulses on Aluminum to be considered.

The laser repetition rate was 1 kHz. In order to detect 30 pulses, a time window of 30 ms was required. The width of the signal varies depending on the bandwidth of the detectors: 0.3 ms (square signal) for PD1, 15 ns (FWHM) for PD2 and 50 ns (FWHM) for PD3. In order to get the peaks of all pulses, the peak detection mode was applied instead of the normal mode of the oscilloscope. For the output from PD1, a general oscilloscope was used (Tektronix TDS350, bandwidth of 200 MHz,

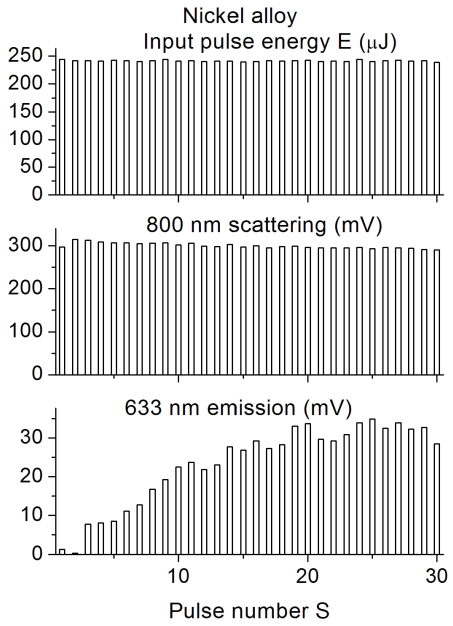

Figure 4.14: An example of signals from three photodiodes for Nickel alloy with input pulse energy $E \approx 250\,\mu$J ($F \approx 136$ mJ/cm^2). Output from PD1 gave each pulses energy within the burst. PD2 gave the plasma emission signal at 633 nm (background being abstracted in the figure). PD3 gave the scattering signal of the 800 nm input pulses. The results were averaged over four measurements under the same laser condition. From the plasma emission at 633 nm, we can see that this fluence is close to $F_{th}(S = 3)$.

1 GS/s sample rate).For the output from PD2 and PD3, an oscilloscope (Tektronix TDS6804B, bandwidth of 8 GHz, 40 GS/s real-time sample rate on two channels) was used to get the accurate peaks. At each energy level, the signal was averaged over four spots with the same parameter set. The spacing between spots was 2 mm.

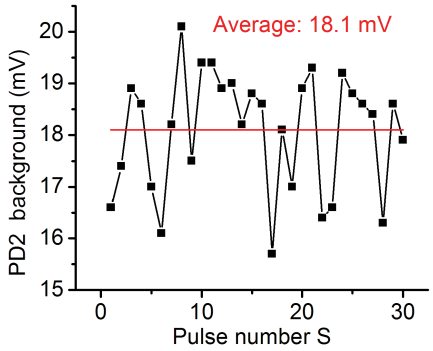

Figure 4.15: Typical PD2 output background. PD2 was used to detect the 633 nm plasma emission. The background was from the electronic devices in the laser system. Each point was an average of four measurements. The average value of the background was about 18.1 mV. The peak-to-peak noise was about 4.5 mV.

4.4.2 Results

An example of signals from different photodiodes is illustrated in Figure 4.14. For PD1 and PD3, the background can be neglected, but not for PD2. The background of the PD2 is shown in Figure 4.15. In Figure 4.14, the background of PD2 was subtracted. The background was from electronic devices in the laser system. When PD2 was blocked, it still existed. For signals connecting to the fast oscilloscope, the 800 nm scattering was stable. It was then used as the trigger for the oscilloscope.

As for the 633 nm plasma emission, it had the same order of magnitude from different metals. By checking the characteristic emission lines of the tested metals and air, it was verified that the emission at 633 nm was from air ionization. It was verified that there was no plasma emission at the sample position if the metal plate was not placed into the beam path. To check the validity of the plasma emission being related to metal ablation, a 0^o 800 nm mirror was placed at the position of the metal plate. When it was illuminated by the laser pulses with the similar

energy level, there was no plasma emission observed. This would expels the chance of the emission coming from focusing of the reflected laser pulses. If the laser pulses continued illuminating the mirror, at some point, the coating was damaged, and then a plasma signal was detected. This confirms that the 633 nm signal was related to the ablation of the metals.

Among the characteristic lines of metals, Nickel has a strong emission around 349-353 nm. It is close to the third harmonic wavelength (354 nm)of YAG laser (1064 nm). With two filters of peak transmission at 355 nm (FWHM: 10 nm) and a 0^o 800 nm mirror in front of PD2, the detection was conducted with both an avalanche photodiode and a GaP amplified detector (ThorLabs PDA25k, wavelength range: 150-550 nm). No signal was observed. From this, it shows that the characteristic metal emission line is much weaker than the plasma emission at 633 nm in the experiment.

For Nickel alloy, the emission signals were collected for for a burst of 30 pulses. The energy/fluence levels were chosen to be close to the ablation threshold. The signals are shown in Figure 4.16 (a). Using linear fit for the experimental results, the threshold for different pulse number S was obtained for zero 633 nm emission (see Figure 4.16 (b)). If we compare the results with those obtained from the crater size method, we can see that within error bar, the two methods produce the same results.

The reasons for the signal suppression with $S > 30$ were not fully understood. One possible reason may be the development of the crater. The change of the crater, such as the depth and the debris, may affect the interaction of the metal and laser pulses, which caused the change of the plasma emission. As a result, the plasma emission cannot be used for characterizing the ablation threshold with $S > 30$.

Among the three metals, Nickel alloy has the smoothest surface. More experi-

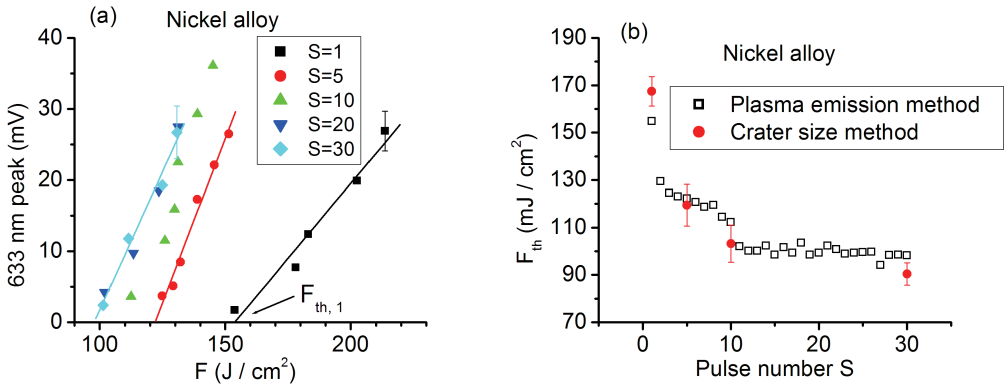

Figure 4.16: (a) Plasma emission at 633 nm as a function of the input pulse fluence for Nickel alloy. The 633 nm signal was collected for a burst of 30 pulses. Here only signals at several representative S are plotted. Each data point was an average over four measurements. The error bar is the standard deviation of the measurements. The lines are the linear fit with different pulse number. (b) Threshold fluence as a function of S for Nickel alloy using the plasma emission method. The results from the crater size method are plotted together for comparison. Within error bar, the results using these two methods agree well.

ments were therefore conducted with Nickel alloy. The results are summarized in Appendix K.

For Aluminum, signals for a burst of 20 pulses were collected. The plasma emission signals and the threshold results are shown in Figures 4.17 (a) and (b). Compared to the Nickel alloy, the plasma signals and the Aluminum threshold values fluctuate more. This may be caused by the large surface roughness for Aluminum. As for the discrepancy between the results from the two methods, it may come from the plasma emission itself. As was mentioned before, the suppression of the plasma signals started after the first several pulses. The plasma emission method may not applicable for Aluminum.

The suppression of the signal was not related to incubation. It may come from the oxygenization of Aluminum, which forms a dielectric material, Al_2O_3. It has

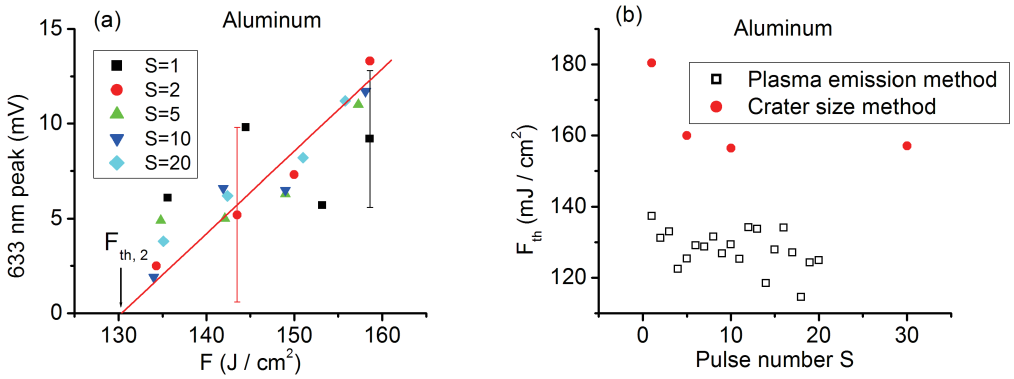

Figure 4.17: (a) Plasma emission at 633 nm as a function of the input pulse fluence for Aluminum. The 633 nm signal was collected for a burst of 20 pulses. Here only signals at several representative S are plotted. Each data point was an average over four measurements. The error bar is the standard deviation of the measurements. The lines are the linear fit with different pulse number. (b) Threshold fluence as a function of S for Aluminum using plasma emission method. The results from the crater size method are plotted for comparison. The threshold from the plasma emission method is about 30 mJ/cm^2 lower than the threshold from the crater size method.

much higher damage threshold than Aluminum. As a result, the signal started to decrease only after several pulses. Therefore, the thresholds obtained for $S > 3$ using this method may not represent the real thresholds.

In conclusion, the plasma emission method is applicable for Nickel alloy with $S < 30$, while inapplicable for Aluminum.

4.5 Model for incubation

This section is based on a paper submitted to Journal of Applied Physics [136]. Dr. Matthias Lenzner performed the fit of the experimental results.

4.5.1 Multiple-pulse laser induced damage threshold

We consider a cylindrically symmetric beam profile $f(r)$ normalized so that $f(r = 0) = 1$, the actual fluence profile being $F_0\, f(r)$. We assume that changing the fluence during the experiment does not change the beam profile $f(r)$. Experimental care has to be taken to fulfill this condition. For example, if a diode-pumped solid-state laser is used as a pulse source, one must not change the energy of the excitation pulses by changing the diode current. This will potentially alter the thermal lens in the crystal and consequently the beam profile of the laser output. A suitable setup to change the pulse energy includes a half-wave plate between crossed polarizers and sufficiently large beam diameters to avoid other detrimental nonlinear optical effects.

Furthermore, we assume an arbitrary incubation model that yields $F_{th}(S, r, F_0)$. We assume that the local fluence controls the damage behavior and neglect any spatio-temporal effects like for example diffusion.

Using the above conditions, we want to find the damage fluence for an arbitrary number S of pulses at the beam center, $F_{th}(S) = F_{th,S}$. In previous sections, we performed measurements where we kept S constant, changed the incident fluence F_0 and measured the radius of the area where the incident fluence exceeds the damage fluence and produced a crater of radius R. We plotted the area A versus $\ln F_0$ and determined threshold and beam diameter as in the single-pulse case described above. We repeated this procedure for all values of S that were needed for an incubation curve $F_{th}(S)$.

Using a known incubation model, see next section, the crater radius R obtained from a burst of S pulses is determined from a, typically transcendental, equation

$$F_0 f(R) = F_{th}[S, F_0 f(R)], \tag{4.5}$$

where

$$F_{th,S} = F_{th}(S, F_0 f(r = 0)) \tag{4.6}$$

determines the input fluence equal to the multiple-pulse LIDT.

Because of the structure of the arguments of F_{th} in Equation (4.5) we can argue as follows to obtain the scaling of the crater radius with fluence and to evaluate the usefulness of the cited logarithmic plot (cf. Figure 4.1). If F_{thN} is a solution to Equation (4.5) for $r = 0$ then for arbitrary F_0 the following relationship must hold

$$F_{th,S} = F_0 f(R) \tag{4.7}$$

from which the crater diameter R can be determined for a given input fluence F_0. (We need to solve the transcendental equation 4.5 for each S only once and then use Equation (4.7) for other input fluences F_0.)

Taking the natural logarithm of both sides of Equation 4.7 yields

$$\ln\left(\frac{F_0}{F_{th,S}}\right) = -\ln[f(R)]. \tag{4.8}$$

For Gaussian beam profiles $f(r) = \exp\left[-2(r/w)^2\right]$, one obtains a linear relationship of $\ln(F_0/F_{th,S})$ and R^2, and $F_0 = F_{th,S}$ for $R = 0$. For other beam profiles, one can plot $\ln(F_0/F_{th,S})$ versus $\ln[f(r)]$ and recover the linear dependence if $f(r)$ is known. These statements are applicable independent of S.

The crater-size method is applicable for a much broader range of incubation models than what has been described so far. Let us illustrate this using as an example a Gaussian input beam and consider an incubation model of the form

$$F_0 f(R) = F_{th}[S, F_0 f(S, R)], \tag{4.9}$$

where the pulse number S also appears in the argument of the function $f = f(S, R)$ unlike in Equation 4.5. The function f described the incident beam profile but actually is the lateral profile of energy deposition. If for example the incubation involves

(i) the creation of intraband traps in dielectrics [34] the multiphoton absorption changes to a lower order with pulse number S. In metals and semiconductors, (ii) the radius of the zone where the absorption changes may increase with pulse S due to diffusion of temperature and carriers. For both cases one can formally write the beam profile responsible for energy deposition as

$$f(S,r) = \exp\left[\frac{-2r^2}{g(w,S)}\right], \tag{4.10}$$

where g is a function that describes the change of the "effective" beam diameter. The crater-size method now produces a plot, cf. Equation 4.8, of

$$\ln\left(\frac{F_0}{F_{th,S}}\right) = \frac{2}{g(w,S)}r^2, \tag{4.11}$$

where $g(w, S = 1) = w^2$. There is still a linear relationship between $\ln(F_0)$ and A but the slope is expected to depend on the number of excitation pulses S. In the two mentioned physical scenarios the diameter of the energy deposition increases with S and this is what one expects also from the slope. Examples of such behavior are shown in Figure 4.5 (TiO_2 film), Figure 4.9 (bulk Nickel alloy), and Figure 4.11 (bulk Nickel alloy). The slope of the curves as a function of S is shown in Figures 4.18 and 4.19. Similar dependencies were observed in metals and semiconductors [132].

4.5.2 Incubation model

We start with an axially symmetric Gaussian beam with fluence

$$F(r) = F_0\, e^{-2r^2/w^2}, \tag{4.12}$$

with a $1/e^2$-radius w and a peak fluence F_0 above the threshold fluence of the irradiated material. We model the threshold fluence F_{th} in Equation 4.1 at which ablation of the material starts, as

$$F_{th}(S) = \frac{H(S-1)}{\alpha(S-1)}, \tag{4.13}$$

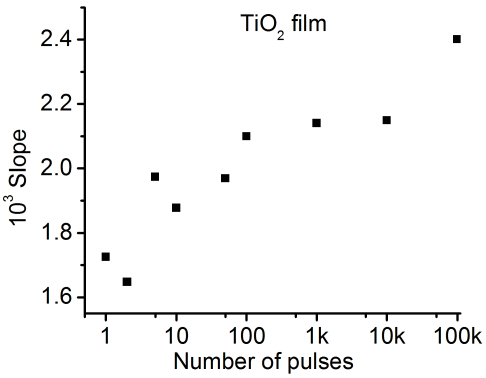

Figure 4.18: The slope of A versus $\ln(F_0)$ as a function of S for TiO_2 film. It is obtained from Figure 4.5.

where α has the meaning of an absorption coefficient, and $H(N)$ is a critical energy density that needs to be deposited to cause LID and ablation. α comprises a part α_0 for the virgin material and a part $\Delta\alpha$, which increases the total absorption after

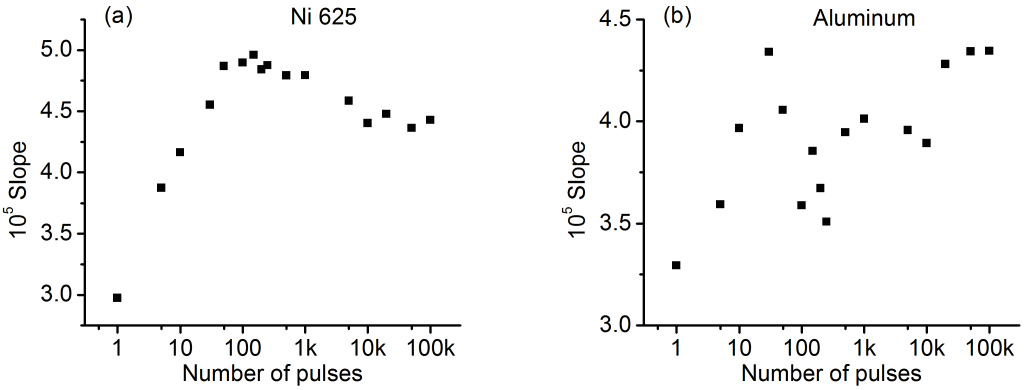

Figure 4.19: The slope of A versus $\ln(F_0)$ as a function of S for bulk Nickel alloy (a) and Aluminum (b). They are obtained from Figures 4.9 and 4.11.

S laser pulses to:

$$\alpha(S-1) = \alpha_0 + \Delta\alpha \left[1 - e^{-F(r)\beta(S-1)}\right]. \tag{4.14}$$

$H(N)$ decreases during a train of pulses according to:

$$H(S-1) = H_0 - \Delta H \left[1 - e^{-F(r)\gamma(S-1)}\right]. \tag{4.15}$$

Appendix L gives the detailed derivation of $\alpha(S)$ and $H(S)$. Recently, it was shown that the ablation threshold is related to the dissociation energy density of a material [141]. This quantity is derived from the sum of the dissociation energies of all bonds that tie the constituent atoms to the lattice and to each other [142]. This approach assumes that the ablation products are single atoms.

From Equation 4.13 with Equations 4.14 and 4.15 we obtain

$$F_{th}(S,r) = \frac{H_0 - \Delta H \left[1 - e^{-F(r)\gamma(S-1)}\right]}{\alpha_0 + \Delta\alpha \left[1 - e^{-F(r)\beta(S-1)}\right]}. \tag{4.16}$$

So far, we have 6 parameters in this equation: H_0, ΔH, γ, α_0, $\Delta\alpha$, and β. One can easily obtain the single-shot ablation threshold $F_{th}(N=1)$ and the saturation value for a large number of pulses $F_{th}(N=\infty)$ from the experimental curves. In terms of these parameters Equation 4.16 can be written as

$$F_{th}(S) = \frac{F_1 - \left[F_1 - F_\infty \left(1 + \frac{\Delta\alpha}{\alpha_0}\right)\right]\left[1 - e^{-F(r)\gamma(S-1)}\right]}{1 + \frac{\Delta\alpha}{\alpha_0}\left[1 - e^{-F(r)\beta(S-1)}\right]}, \tag{4.17}$$

which has reduced the unknowns to β, γ and the ratio $\Delta\alpha/\alpha_0$.

This equation determines the LIDT of a material at a certain position r after S pulses of peak fluence F_0 have been applied. For an axially symmetric Gaussian beam this defines a circle of radius R, which corresponds to the edge of the ablation crater obtained in the experiment.

The threshold fluence for each pulse number S will be determined as discussed in section 4.5.1 from a measurement of crater radius R versus the logarithm peak

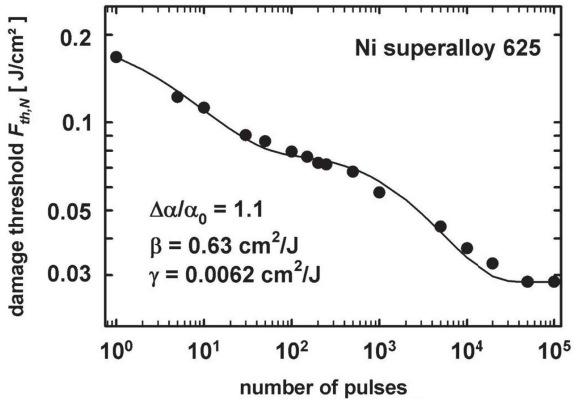

Figure 4.20: Incubation curve of Nickel superalloy 625 for 37-fs pulses at 800 nm and 1 kHz. The solid line is a fit using Equation 4.18 with the parameters given in the figure.

fluence $\ln(F_0)$ and extrapolating the resulting curve $R^2 = (w^2/2)[\ln(F_0) - \ln(F_{th})]$ to $R = 0$. For our experimental conditions (S-on-1, with pulses of identical energy), we can then replace $F(r)$ in Equation 4.17 by $F(r = 0) = F_0 = F_{th}$. The transcendental equation that has to be fitted to the experimental data is now:

$$F_{th}(S) = \frac{F_1 - \left[F_1 - F_\infty\,(1 + \frac{\Delta\alpha}{\alpha_0})\right]\left[1 - e^{-F_{th}\gamma(S-1)}\right]}{1 + \frac{\Delta\alpha}{\alpha_0}\left[1 - e^{-F_{th}\beta(S-1)}\right]}, \tag{4.18}$$

with the three fit parameters $\Delta\alpha/\alpha_0$, β, and γ.

4.5.3 Fitting of experimental data

We used Equation 4.18 to fit experimental data from our own measurements as well as from the measurements of others. Figure 4.20 shows an incubation curve for the Nickel superalloy 625. The experiment was performed with linearly polarized pulses from a Titanium:sapphire CPA system at a center wavelength of 800 nm and 37 fs duration. The energy of the pulses was adjusted by rotating a half-wave plate before a polarizer. In this curve, as in others to follow, a distinct feature can be

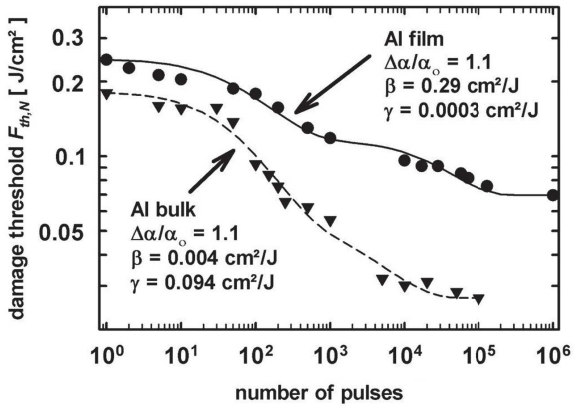

Figure 4.21: Laser damage (ablation) threshold fluence F_{th} as a function of the number S of pulses for Aluminum film (dots) and bulk sample (triangles) with fs pulses at 800 nm and 1 kHz. The lines are fits using Equation 4.18 with the parameters given in the figure.

recognized, looking like a "hump" in the center part. This indicates the existence of two components in the incubation process with different rates of pulse induced changes. For example, this could be due to a laser induced change of absorption dominating at small pulse numbers S followed by a change in dissociation energy that becomes dominant at large S. This behavior is expected for $\beta > \gamma$. Another possible cause is the existence of two different processes affecting the absorption with different rates and relaxation times.

Similar results were obtained for Aluminum under the same laser excitation conditions as for Nickel. Here, we used a bulk sample of Aluminum 6061 and an Aluminum film. The experimental data and the fit to our model are shown in Figure 4.21. The difference in absolute LIDT values is attributed to the different surface roughness, the film has an optical quality surface and hence reflects more of the incoming laser energy, consequently withstanding a larger incident fluence. At larger pulse numbers ($S > 100$), the incubation in the bulk material is more pronounced. This can be a result of increasing surface roughness during the pulse train and the occurrence of

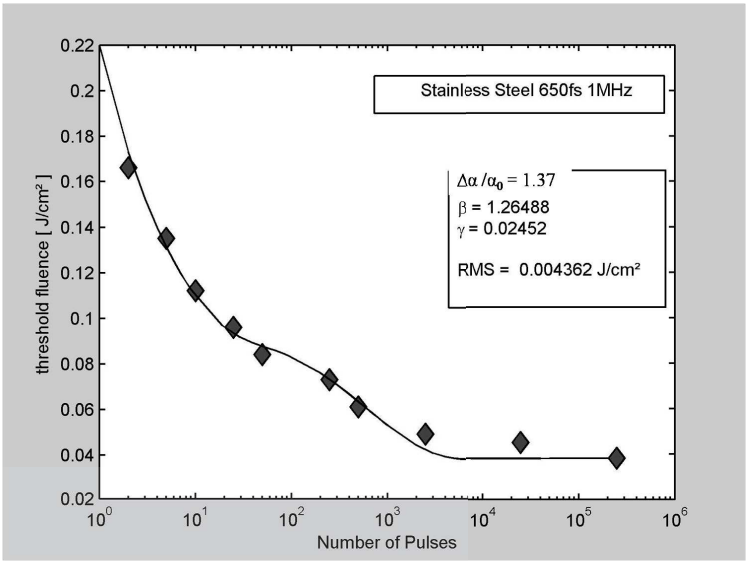

Figure 4.22: Incubation curve of stainless steel for 650-fs pulses at 1030 nm. The data were taken from reference [143]. The solid line is a fit using Equation 4.18 with the parameters given in the figure.

ripples, see discussion below.

Another set of experimental data that could be fitted successfully was taken from reference [143]. The experiments were performed in stainless steel with different pulse durations and repetition rates. In Figure 4.22, we fitted our model to the data for a pulse duration of 650-fs pulses at a wavelength of 1030 nm. The pulses had a repetition rate of 1 MHz and was circularly polarized. The two-component incubation behavior is clearly visible.

The physical processes underlying the incubation model are not specific to certain classes of materials. Hence, not only metals but also dielectric materials can the modeled. Figure 4.23 shows experimental data for thin films of TiO_2 (116 nm thick) on a fused silica substrate. The damaging laser pulses were 55 fs in duration at a wavelength of 800 nm, linearly polarized.

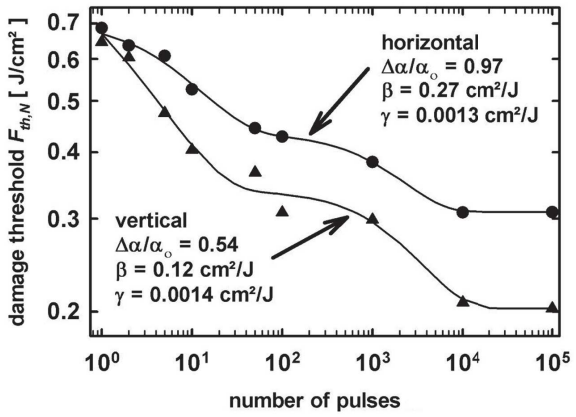

Figure 4.23: Incubation curves of TiO_2 thin films on fused silica substrate along two directions, parallel (horizontal) and perpendicular (vertical) to the polarization of the laser light. Laser pulses were 55 fs in duration at a wavelength of 800 nm. The solid lines are fits using Equation 4.18 with the parameters given in the figure.

In general, the craters have an elliptical footprint, therefore, we determined the threshold independently for two directions: horizontally (which is parallel to the laser polarization) and vertically. Naturally, for an isotropic material, the single-shot threshold is identical for the two directions. However, for multiple pulses, the thresholds change in a different way, eventually leading to different saturation values F_∞ for a large number of pulses (see Figure 4.6).

Here, we can draw some conclusion to the physical processes involved from the fit parameters. While γ is about the same for both polarization directions, $\Delta\alpha/\alpha$ and β differ almost by a factor of 2. The latter parameters describe the laser induced change of absorption, which obviously differs for the two directions, i.e. depends on the polarization direction of the damaging laser pulse. This behavior could be connected to the occurrence of laser induced periodic surface structures (LIPSS), which were observed in these samples. It is well known that LIPSS structures can increase the absorption, as shown in Appendix G.

4.6 Chapter summary

In this chapter, we discussed the validity of the crater size method for multiple-pulse (S-on-1) damage threshold measurements.

First, we checked the agreement between the LIDTs obtained from the crater size method and the scattering change method. The incubation curves of TiO_2 films from these two methods show good agreement. For a linearly polarized laser, it was found that the multiple-pulse LIDTs were different along the horizontal and vertical directions. A likely reason of this behavior is the occurrence of ripples in the films.

Second, we explored LIDTs of bulk metals using the plasma emission method. Incubation curves were obtained using the plasma emission at 633 nm with small number of pulses. Similar curves were also obtained using the crater size method for Nickel alloy and Aluminum. The results from these two methods overlapped well for Nickel alloy. There was bigger discrepancy for Aluminum. This may come from the big fluctuation of plasma signals caused by large surface roughness of Aluminum.

The conditions of the applicability of the crater size method for S-on-1 tests were discussed. We showed that extrapolation of the squared ablation crater diameter versus the natural logarithm of the peak fluence can be used to determine the damage threshold also in multi-pulse ablation experiments if Gaussian beams are used. A more general form $\ln(F_0) \propto \ln(f(r_c))$ can be used for any beam profile if it is known. The condition for the applicability to S-on-1 experiments is that the beam profile does not change with the pulse energy. The slope of the $\ln(F_0)$ versus A plot can depend on S due to for example a change in the multiphoton order of the absorption and diffusion.

Last, an empirical incubation model was introduced to explain experimental results from metals and dielectrics. It includes two physical processes: the laser induced

change of absorption of the material with every laser pulse and the laser induced change of the specific energy that is necessary to remove an atom or molecule from the material. A common feature for the incubation curves is a "hump" in the center part. This indicates the existence of two components in the incubation process, which can be successfully explained using this model.

The results described in this chapter were published in [135, 136].

Chapter 5

Femtosecond laser induced filament in air

5.1 Introduction

5.1.1 Literature review and open questions

The broad introduction of ultrafast lasers in the 1990s [6] led to the discovery of many new phenomena, from which active research topics were developed. One of the topics which has gained a great deal of interest is femtosecond (fs) pulse induced filaments (see References [21–23] for recent reviews). Filaments have been produced is various transparent media such as air (gases), transparent solids and liquids [22].

Filaments are initiated when laser pulses self-focus to intensities large enough to produce multiphoton ionization. The resulting plasma produces a radial refractive index variation (negative lens) counteracting the self-focusing, which leads to filamentation over distances that can exceed several tens of meters depending on the energy and duration of the optical pulse [20].

The first experiment was reported by Braun *et al.* in 1995 with an intense 775-nm infrared (IR) 200-fs pulse [20]. It was found that the self-channeling of laser pulses could propagate 20 m in air at a pulse energy of 0.75 mJ. Shortly afterwards, filaments of fs laser pulses were shown to occur over more than 50 m [144] and then over several hundreds of meters [145]. Experiments in Spring 2003 at École Polytechnique had revealed an horizontal filamentation over a distance larger than 2 km [146, 147]. Applications of filaments range from lightning control and triggering of discharges [148], to remote sensing [25], to few-cycle pulse generation [26, 27].

One of the interesting applications is using these filaments to help guide signals. There is work discussing the possibility of guiding signals with an array of filaments [149–151]. Châteauneuf *et al.* demonstrated microwave guiding over 16 cm in air using a large diameter plasma waveguide [53]. The waveguide was generated with the 100 TW femtosecond laser system (pulse energy: 1.5 J) at the Advanced Laser Light Source facility. The diameter of the waveguide was around 45 mm. The center was hollow (air) and the outside ring consisted about 1030 filaments distributed in the wall of the waveguide [53].

It is very interesting to know whether the filaments can help guide waves or not with much lower energy (mJ) laser source. This could open new doors for remote sensing applications. From the literature, evidences were found for enhanced backward scattering in the presence of one filament [54]. It is worthwhile to check the possibility of guiding a wave using one or several filaments produced by a fs laser pulse with mJ energy.

To take full advantage of the potential these plasma channels offer for many applications their properties including the transient behavior must be known. Two key parameters of laser plasmas are the electron density N_e and electron temperature T_e. Plasma densities produced by filaments in air are on the order of $10^{18}\mathrm{m}^{-3}$ to $10^{24}\mathrm{m}^{-3}$ [152–154]. Previous measurements obtained the electron density from the

electric conductivity of the plasma [152, 155], from interferometry measuring the optical phase shift introduced by a plasma channel [153], by optically probing the plasma induced diffraction [55, 154, 156, 157], and by third harmonic generation of a weak femtosecond probe pulse intersecting a pump laser induced plasma [158].

More recently, a spectroscopic approach was applied to characterize fs laser filaments in argon gas [159] and air [160]. The plasma density was derived from the Stark broadened fluorescence line width, while the electron temperature was determined from relative line strengths. Typically these techniques average over several nanoseconds (the shorter of the detector integration time and the fluorescence lifetime). Simulations of kinetic processes in air plasmas suggest substantial changes of the electron temperature and electron density on time scales of a few hundred picoseconds [161].

While the transient behavior of the electron density in air plasmas was measured with a fs probe in Reference [55] the transient electron temperature had not yet been determined with sub ns temporal resolution.

This chapter is based on a paper published in Physical Review E [162].

5.1.2 Chapter goals

In this chapter we determine the transient electron temperature and electron density in an air plasma with ps resolution by measuring the real and imaginary parts of the time dependent refractive index and applying the Drude model. The experimental results are compared to plasma kinetic theory that takes into account elastic and inelastic collisions with ionic and neutral molecules.

The possibility of guiding a wave with single and multiple filaments will be discussed. Signal guiding with a single filament will be studied experimentally. The idea

of wave guiding with multiple filaments will be checked from theoretical perspective.

5.2 Transient absorption and diffraction of an air plasma

A schematic diagram of the experimental setup is shown in Figure 5.1. An air plasma channel was produced by focusing the pulses from a 40-fs, 1-kHz, 2-mJ Ti:sapphire oscillator-amplifier system using an $f = 1$ m lens. The beam profile was Gaussian with a beam radius of about 8 mm. The transient absorption and diffraction of the plasma were measured by a time delayed, weak probe pulse. The chopper operated at 71 Hz. The energy of the probe beam is less than 1% of the total energy from the laser.

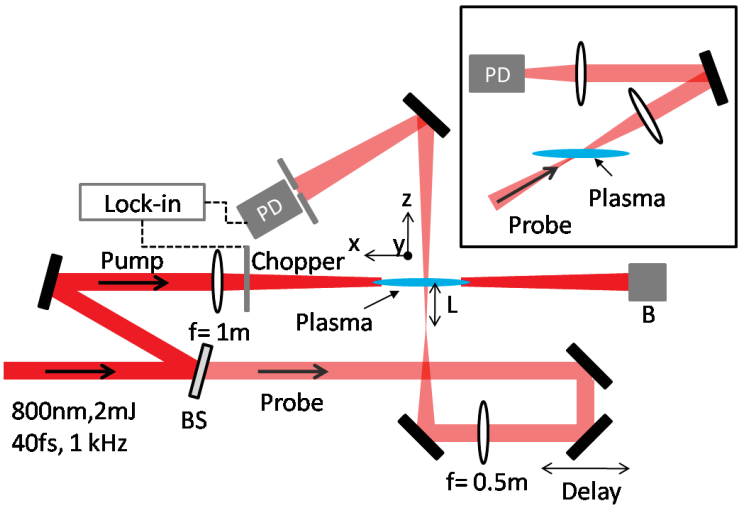

Figure 5.1: Experimental setup to probe the transient diffraction and absorption of a fs pulse produced air plasma. The inset shows the diagram for the absorption measurements. BS: beam splitter, PD: photodiode, B: beam blocker.

A pump-probe technique similar to that described in Ref. [55] was applied to measure the transient diffraction. For higher sensitivity and to employ lock-in detection we replaced the CCD camera with a pinhole and photodiode to monitor the negative lens (real part of the dielectric constant) produced by the plasma. The plasma diameter was estimated from the plasma emission to be $d \approx 200$ μm (FWHM). As will be explained below the probe beam diameter at the position of the plasma was $2d$. L is the distance from the probe's beam waist to the plasma.

For the measurement of the absorption (imaginary part of the dielectric constant), the probe beam was focused through the plasma center ($L = 0$) and the transmitted beam was fully collected by the photodiode with the pinhole removed. To increase the interaction length with the plasma, probe and pump included an angle of $\beta = 30$ degrees (see inset of Figure 5.1). The measured absorption (in percent) as a function of delay is depicted in Figure 5.2. All results are plotted for delays $\tau > 35$ ps to

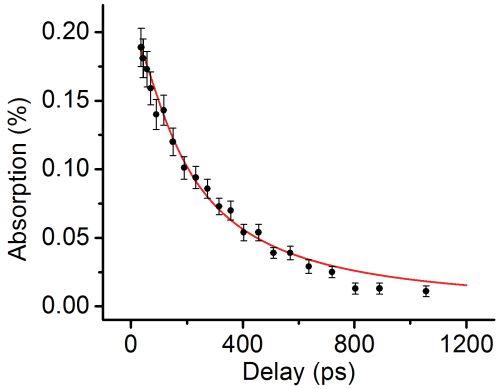

Figure 5.2: Measured plasma absorption as a function of the delay (data points). The solid line is a modeling result with an initial Gaussian N_e and initial flat-top T_e transverse profile (see section 5.4). The error bars represent the combined contribution from the absorption and input power measurements (relative error of the latter $\sim$1%).

avoid complications in the data interpretation resulting from pulse overlap and non-

equilibrium electron distributions (see Appendix M for results near zero time delay). In addition, we avoided delays at which index changes due to molecular alignment revival are expected [163]. Since our probe diameter was about 0.4 mm each data point represents an average over about 2 ps, further reducing the effect of molecular rotation.

Figure 5.3 shows the measured diffraction signal $|\Delta S|$ as a function of delay. The

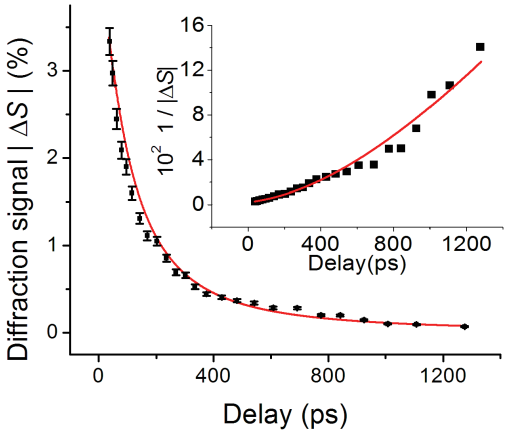

Figure 5.3: Measured diffraction signal $|\Delta S|$ as a function of the delay after subtracting an offset of about 0.3% produced by heating of the gas (data points). The solid line is a modeling result with an initial Gaussian N_e and initial flat-top T_e profile (see section 5.4). The inset shows $1/|\Delta S(t)|$ (data points), which changes nonlinearly with delay time, and modeling results (see section 5.4). The error bars represent the combined contribution from the diffraction and input power measurements and from the far-field approximation.

signal recovers on a time scale of a few hundred ps, similar to what was observed previously [55, 157]. It is interesting to note that the signal recovery is not complete after 1.3 ns and that there is a small signal ($\sim 0.3\%$) even for negative delays (note that ps negative delays actually correspond to a delay of one ms relative to the previous excitation pulse). We attribute this signal, which decays on a time scale

of a few ms, to a temperature increase of the air. The thermal time constant for heat dissipation can be estimated with $\tau_T = \rho_{air} c_p d/(4h) \approx 3$ ms [164], where $\rho_{air} \approx 1$ kg/m^3 is the air density (at 1600 m above sea level), $c_p \approx 1 \times 10^3$ J/(kg K) is the mass specific heat capacity, and $h \approx 15$ W/(m^{2}K) is the heat transfer coefficient. This signal disappeared at a repetition rate of 333 Hz (see Figure 5.4).

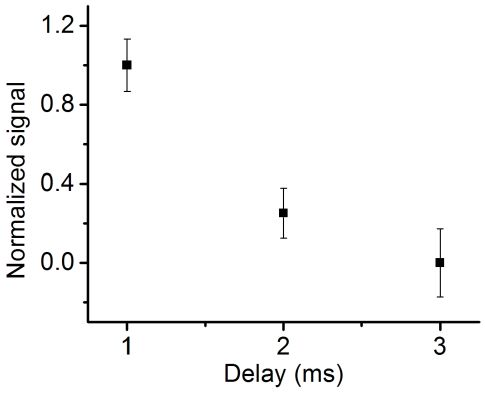

Figure 5.4: Normalized diffraction signal on a ms scale. The signal was close to zero after 3 ms.

To relate the diffraction results to the refractive index change we modeled the signal using Fraunhofer diffraction. The distance from the plasma to the detector was about 1 m, which requires scrutinization of the accuracy of the far-field results. We therefore also performed a numerical analysis based on Fresnel diffraction; the results are within 1.5% of those obtained using the far-field approximation. We show here the semi-analytic expression for the Fraunhofer case because they show explicitly the parameter dependencies.

The diffraction geometry and the coordinate system used are shown in Figure 5.1, with z ($-x$) being the propagation direction of the probe (pump) and y being perpendicular to both the filament and probe beam axes. The pinhole in front of the

detector PD selects the zero spatial frequency ($\rho = 0$) component of the product of the probe field, $E(x, y)$ and the complex transmission function of the filament, $\exp[i\phi(x, y)]$:

$$\begin{aligned} S(\rho = 0) = S_0 &= |\text{F.T.}\{E(y)\exp[i\phi(y)]\}|^2 \\ &= \frac{C}{w^2}\left|\int \exp\left[-\frac{y^2}{w^2} + ik\left(\frac{y^2}{2R} + \int \tilde{n}(y,z)\mathrm{d}z\right)\right]\mathrm{d}y\right|^2, \end{aligned} \tag{5.1}$$

Here w and R are the beam radius and the radius of the wavefront of the probe, respectively, at the position of the filament, C is a constant, $k = 2\pi/\lambda$ is the wave vector, and $\tilde{n}$ is the (complex) refractive index. Because of the larger transverse density gradient, the plasma causes diffraction with respect to "y" only. $\phi(y) = k\int \tilde{n}(y, z)\mathrm{d}z$, in which the integral represents the phase change through the plasma along z direction. The beam change with respect to the "x" coordinate is that of an undisturbed Gaussian probe beam.

According to the Drude model of a plasma (see for example [72]), the dielectric constant can be written as

$$\epsilon = 1 - \frac{\omega_{pe}^2}{\omega^2 + i\omega\nu_e} = \tilde{n}^2 = (n + in_I)^2, \tag{5.2}$$

where ω is the probe laser frequency and $\omega_{pe} = \sqrt{N_e e^2/\epsilon_0 m_e}$ is the plasma frequency. Here e and m_e are the electron charge and mass, respectively, ϵ_0 is the permittivity of free space, and ν_e is the electron collision rate.

For weakly ionized plasmas, as is the case here, the plasma induced index change at $y = z = 0$ is $|\Delta\tilde{n}_m| \ll 1$. From the Drude model it can be shown that the imaginary part of the index n_I is much smaller than the real part Δn_m for electron densities $N_e < 10^{24}$ m^{-3} and its contribution to the diffraction signal can be neglected.

Under these conditions the relative signal change is proportional to the index

change

$$\Delta S(L, w_0) = \frac{S_0(\Delta n_m) - S_0(\Delta n_m = 0)}{S_0(\Delta n_m = 0)} \approx Q(L, w_0)\Delta n_m, \tag{5.3}$$

where the calibration factor Q depends on the waist w_0 of the probe beam, the distance L between the probe waist and the plasma center, and on $\Delta n(y, z)$. $\Delta n(y, z)$ is controlled by the electron density distribution (see Equation 5.6). For flat-top transverse electron density profile, there is no analytical expression of Q. It is calculated numerically. For Gaussian profiles and $|\Delta n_m| \ll 1$,

$$\begin{aligned} S_0(\Delta n_m) \approx & \frac{C}{w^2}\left|\int \exp\left(-\frac{y^2}{w^2} + \frac{iky^2}{2R}\right)\mathrm{d}y \right. \\ & \left. + \frac{ikd}{2}\sqrt{\frac{\pi}{\ln 2}}\Delta n_m \int \exp\left(-\frac{y^2}{w^2} - \frac{4\ln 2 y^2}{d^2} + \frac{iky^2}{2R}\right)\mathrm{d}y\right|^2, \end{aligned} \tag{5.4}$$

where $w^2 = w_0^2\left[1 + (L\lambda M^2/\pi w_0^2)^2\right]$. Inserting Eq. (5.4) into Eq. (5.3) and neglecting the much smaller Δn_m^2 term, we obtain for Q

$$Q \approx \frac{2\Re\left(\tilde{A}\tilde{B}^*\right)}{\left|\tilde{A}\right|^2}, \tag{5.5}$$

$$\tilde{A} = \sqrt{\frac{\pi}{(1/w^2 - i\ k/(2R))}}, \quad \tilde{B} = \frac{i\ (\pi/\sqrt{2\ln 2})kd}{\sqrt{2/w^2 - i\ k/R + 8\ln 2/d^2}}.$$

For example, for flat-top and Gaussian transverse electron density profiles of FWHM d =200 μm, $Q \approx 910$ and $Q \approx 520$, respectively, for our experimental geometry ($w_0 = 54$ μm, $L = 20$ mm and a beam M^2 value of 2.1). Typical relation between Q and L is shown in Figure 5.5. For flat-top N_e profile, there is a maximum near L=40 mm. For Gaussian N_e profile, a maximum appears at L> 100 mm.

Because the excitation beam is Gaussian and the plasma is weakly ionized, it is reasonable to assume that the initial electron density can be approximated by a Gaussian profile. Because of the density dependent recombination, the electron density at later times will approach a flat-top profile (see Section 5.4). For a rough

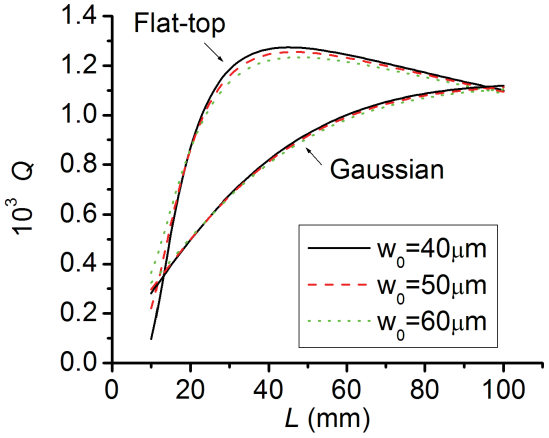

Figure 5.5: Q versus L for different w_0 for flat-top and Gaussian transverse electron density profiles of FWHM d =200 μm. For flat-top profile, it is calculated numerically. For Gaussian profile, it is calculated using Equation 5.5.

estimation the scale factor Q can be used to obtain the time dependent refractive index changes $\Delta n_m(t)$ and the electron density N_e from the diffraction signal assuming constant (flat-top) profiles as will be explained in the next section.

5.3 Determination of the initial plasma density and electron temperature

If we introduce the critical electron density $N_{cr} = \omega^2 m_e \epsilon_0 / e^2 \approx 1.74 \times 10^{27}$ m^{-3} for which $\omega_{pe} = \omega$, and use the fact that $\nu_e \ll \omega$ ($\nu_{e,max} \sim 10^{13}$ Hz, $\omega = 2.4 \times 10^{15}$ Hz) and $N_e \ll N_{cr}$ in this plasma, we can approximate the real part of the refractive index by $n \approx 1 - N_e/(2N_{cr})$ according to Equation 5.2. This yields for the plasma induced (real) index change as a function of the plasma density

$$\Delta n(t) \approx -\frac{1}{2}\frac{N_e(t)}{N_{cr}}. \tag{5.6}$$

If we make the approximation that the shape of the electron density profile does not change in time we can estimate $N_e(r = 0)$ at different delays using Equations 5.3 and 5.6 and the data points from Figure 5.3 for flat-top and Gaussian profiles. The data points in Figure 5.6 show the normalized electron density assuming a flat-top profile for N_e. The initial plasma density is about $N_{e0} = 1.3 \times 10^{23}$ m^{-3} and $N_{e0} = 2.3 \times 10^{23}$ m^{-3} for flat-top and Gaussian density profiles with FWHM widths $d = 200$ μm, respectively.

The absorption coefficient is proportional to the imaginary part of the refractive index change, $\alpha = 2\omega n_I / c$. Using Equations 5.2 and 5.6 and the previous approximations ($\nu_e \ll \omega$ and $N_e \ll N_{cr}$), it can be written as

$$\alpha(t) \approx \frac{\nu_e(t) N_e(t)}{c N_{cr}}, \tag{5.7}$$

where c is the speed of light. For $\alpha \ll 1$, the relative absorption change experienced by the probe is

$$A(t) = \frac{E_0 - E_1}{E_0} = \iint \alpha(t, y, z) \mathrm{d}y \mathrm{d}z, \tag{5.8}$$

where E_0 and E_1 are the input and output probe pulse energies, respectively. To extract the electron temperature we need to evaluate the electron collision rate ν_e

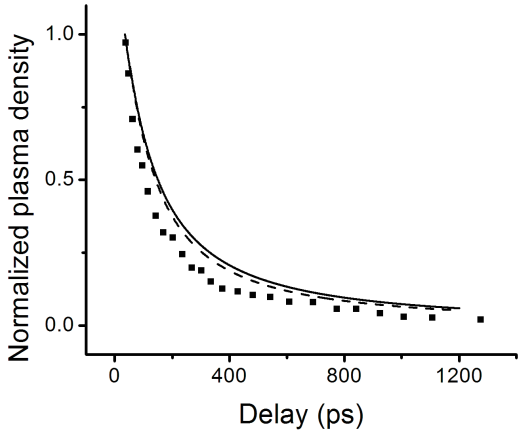

Figure 5.6: Plasma density $N_e(r = 0)$ as a function of delay. The data points are obtained from the diffraction experiment (data points in Figure 5.3) assuming time-invariant flat-top electron density radial distributions. The solid and dashed line are from the model (see section 5.4) and represent initially flat-top and Gaussian $T_e(r)$ distributions, respectively. The initial electron distribution was Gaussian. The two curves are almost identical.

contained in Equation 5.7. The collision rate can be written as the sum of the electron - ion and the electron - neutral collision rates $\nu_e = \nu_{ei} + \nu_{en}$ [161]. The electron - ion collision rate in weakly ionized plasmas is given by

$$\nu_{ei}(t) = c_{ei} \ln \Lambda(t) \frac{N_e(t)}{T_e^{3/2}(t)}, \tag{5.9}$$

where $c_{ei} = e^4 / \left(6\epsilon_0{}^2 \sqrt{2\pi^3 m_e {k_B}^3}\right)$, k_B is the Boltzmann constant and $\ln \Lambda$ is the Coulomb logarithm [72]. The Coulomb logarithm is weakly dependent on N_e and T_e and is typically used as a constant on the order of 10. The uncertainty of its value increases as $1/|\ln \Lambda|$ [165]. We determined $\ln \Lambda$ from a fit to the experimental data (see next section) and use here $\ln \Lambda \approx 4$.

The electron - neutral collision rate can be expressed as [161]

$$\nu_{en}(t) = N_n \sigma_{en} (k_B/m_e)^{1/2} T_e^{1/2}(t), \tag{5.10}$$

where $N_n \approx 2.0 \times 10^{25}$ m^{-3} is the density of neutral particles, which can be regarded as time independent in a weakly ionized plasma, and $\sigma_{en} \approx 1 \times 10^{-19}$ m^2 is the collision cross section [161]. For $T_e \approx 10000$ K, $\nu_{en} \approx 1 \times 10^{12}$ Hz.

Using Equations 5.7 to 5.10, the measured absorption A, and the initial N_e, we can estimate the initial electron temperature. Assuming a flat-top temperature profile we obtain $T_{e0} \approx 3900$ K for Gaussian $N_{e0}(r)$ while for Gaussian $T_{e0}(r)$ and $N_{e0}(r)$ profiles $T_{e0}(0) \approx 5400$ K. The uncertainty of the initial temperature range is about 8%. In the next section we will apply a kinetic plasma model taking into account the spatial evolution of the electron density and temperature profiles during relaxation to extract $T_e(t)$ from the measurements. The model will also allow us to discuss the evolution of $T_e(r,t)$ and $N_e(r,t)$ transverse profiles.

5.4 Modeling and discussion

Even though the ionization potential of O_2 is considerably lower than that of N_2 (12.1 eV versus 15.6 eV [72]), for typical pulse intensities in filaments, there can be a non-negligible density of nitrogen ions [166,167]. During our time scale of interest, the plasma density changes due to the recombination of electrons with ions and the electron and ambient gas temperature change due to elastic and inelastic collisions. The rate equation for the electron density can be written as [55]

$$\frac{\mathrm{d}}{\mathrm{d}t}N_e(t) = -k_{ei}N_e(t)N_i(t) = -k_{ei}N_e^2(t), \tag{5.11}$$

where N_i is the ion density, which equals N_e here. With the assumption that k_{ei} is constant a solution to Eq. (5.11) is $N_e(t) = N_{e0}/(1 + k_{ei}N_{e0}t)$. This expression was previously used to deduce $k_{ei} \approx 1.2 \times 10^{-13}$m^3/s from time-resolved diffraction measurements [55]. For a more accurate description of the recombination process the T_e dependence of the recombination rate must be taken into account, which causes k_{ei}

to be a function of time. For a temperature range from 80 K to 11000 K a rate constant of $k_{ei}(T_e) \approx K_0/\sqrt{T_e[\mathrm{K}]}$ m^3/s was deduced from measurements of the electron recombination with both O_2^+ and N_2^+ [168]. The coefficients $K_0(O_2^+) \approx 3.3 \times 10^{-12}$ and $K_0(N_2^+) \approx 6.1 \times 10^{-12}$ are similar but not identical. We will consider in our model the electron temperature dependence of k_{ei} and use K_0 as a fit parameter, which contains the information on the average relative density of singly ionized nitrogen and oxygen molecules.

The relaxation of the electron temperature is controlled by elastic and inelastic collisions between electrons and ionic and neutral molecules:

$$\frac{\mathrm{d}}{\mathrm{d}t}T_e(t) = \frac{2m_e}{m_{i,n}}(\nu_{ei} + \nu_{en})(T_{i,n} - T_e) + V(T_e). \tag{5.12}$$

Here $m_{i,n}$ ($T_{i,n}$) is the mass (temperature) of the ionized and neutral molecules, which are assumed to be equal, and we also do not distinguish here between oxygen and nitrogen. The introduced errors are small. The first summand describes the energy transfer due to elastic collisions according to the Landau-Spitzer model [72]. The second term takes into account inelastic collisions exciting molecular vibrational degrees of freedom.

The energy transfer rate to vibrational degrees of freedom of O_2 and N_2 molecules can be written as

$$\frac{3k_B}{2}V(T_e) = -\frac{(T_e - T_b)}{T_e}\sqrt{\frac{k_B T_e}{m_e}}N_n \left[0.79\sigma_{N_2}(T_e)\epsilon_{N_2} + 0.21\sigma_{O_2}(T_e)\epsilon_{O_2}\right], \tag{5.13}$$

where σ_x is the inelastic collisional cross section for collisions with nitrogen and oxygen molecules and $\epsilon_{N_2(O_2)} = 0.29$ eV (0.20 eV) is the vibrational energy quantum of N_2 (O_2) [72]. The experimentally obtained inelastic collision cross sections can be approximated analytically by

$$\sigma_{N_2(O_2)} = a_0^2 \exp\left[\sum_{k=0}^{4} b_k \ln\left(\frac{T_e k_B}{e}\right)^k\right], \tag{5.14}$$

where $a_0^2 = 2.8 \times 10^{-21}$ m^2, $b_0 = 2.172$, $b_1 = 1.799$, $b_2 = -0.6725$, $b_3 = 0.0954$, $b_4 = -0.00565$ for N_2, and $b_0 = 2.465$, $b_1 = 0.825$, $b_2 = -0.2325$, $b_3 = 0.0194$ and $b_4 = -0.00094$ for O_2 [169].

We assume that the temperature of ions and neutral molecules (background temperature) is equal with an initial value of 300 K. This background temperature changes according to

$$\frac{\mathrm{d}}{\mathrm{d}t}T_b(t) = -\frac{3k_B N_e}{\rho_{air} c_p}\frac{\mathrm{d}T_e}{\mathrm{d}t}\bigg|_{elastic}. \tag{5.15}$$

During our time scale of interest, only elastic collisions lead to an increase in the molecules kinetic energy (temperature). The vibrational degrees of freedom excited through inelastic collisions exchange energy with translational degrees of freedom (VT relaxation) slowly and the corresponding time constants are much greater than a few ms [170, 171].

The rate equations 5.11, 5.12 and 5.15 are solved numerically. We take into account the radial (r) dependence of the temperature and electron density and compute the diffraction and absorption. We assume that initially the electron density $N_e(r)$ is Gaussian and use the corresponding initial value of 2.3×10^{23} m^{-3}. The initial electron temperature is controlled by the kinetic energy of the electrons after multiphoton ionization of O_2 and N_2. It should be noted that inverse bremsstrahlung has only a minor effect on the electron energy for sub 100 fs pulses. In the limit where multiphoton absorption dominates, the photon energy rather than the intensity profile $I(r)$ controls the initial $T_e(r)$, which is then best described by a flat-top profile. Although for our laser and beam parameters tunneling ionization cannot be neglected we will assume this initial temperature profile with the previously estimated $T_{e0} = 3900$ K. To evaluate the impact of this assumption we will compare the results to an initially Gaussian temperature profile later.

Free parameters are the Coulomb logarithm and K_0, which are determined from

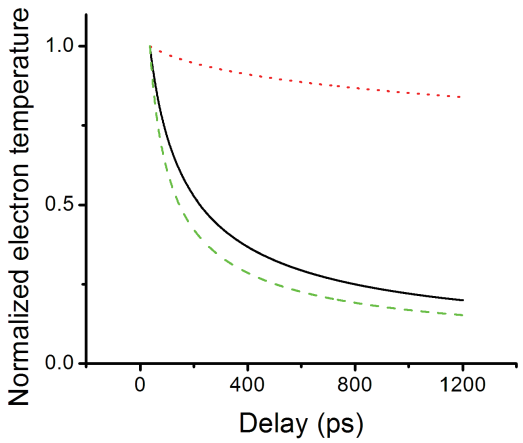

Figure 5.7: Normalized electron temperature $T_e(r = 0)$ as a function of delay. The solid and dashed line are from a fit of the model to the experimental data and represent initially flat-top and Gaussian $T_e(r)$ distributions, respectively. The initial electron distribution was Gaussian. The dotted line was calculated with the same parameters as the solid line but without inelastic collisions.

a simultaneous best fit to the diffraction and absorption measurements. For $\ln \Lambda = 4$ and $K_0 = 2.1 \times 10^{-12}$, the modeling results and the measurements are shown in Figures 5.2 and 5.3 showing good agreement overall. For comparison we also evaluated the case of an initially Gaussian temperature profile $T_e(r)$ with a peak value of $T_{e0} = 5400$ K. The relaxation of N_e and T_e at the center of the plasma is depicted in Figures 5.6 and 5.7. It is obvious that the decay curve $N_e(t)$ is less sensitive to the assumed initial radial distributions of the plasma parameters than $T_e(t)$.

The electron temperature averaged over 1 ns for an initially flat-top T_e profile is in good agreement with the 1500 K used in [157] to define a temperature independent rate k_{ei}. It should also be mentioned that if we use separate recombination equations for O_2^+ , $k_{ei}[O_2^+](T_e) = 6 \times 10^{-11}/T_e[\mathrm{K}]$ m^3/s , and N_2^+, $k_{ei}[N_2^+](T_e) = 4.85{\times}10^{-12}/\sqrt{T_e[\mathrm{K}]}$ m^3/s, with the published k_{ei} coefficients [157,168],

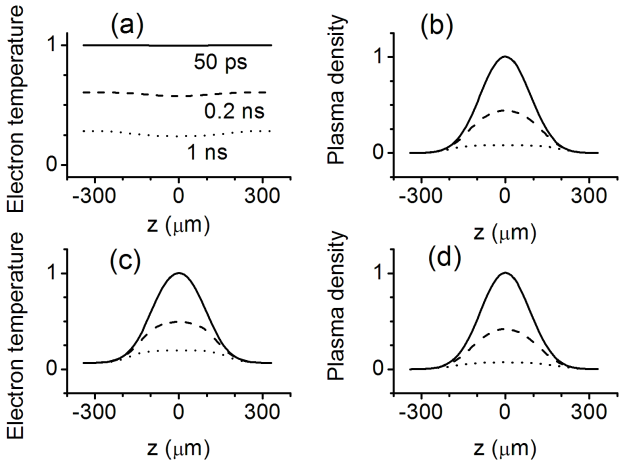

Figure 5.8: Calculated electron temperature and density profiles at different delay times for two sets of initial profiles ($x = y = 0$). (a),(b): flat-top $T_{e0}(r)$, Gaussian $N_{e0}(r)$, (c), (d): Gaussian $T_{e0}(r)$ and $N_{e0}(r)$.

the initial ion ratio becomes a free parameter. With $N_{O2+}/N_{N2+} \approx 3.3$ we obtain a similarly good agreement with the experimental results. This ion ratio is what one can expect for our experimental conditions using the ionization rates from [167].

The inelastic collisions exciting molecular vibrations play a major role in the relaxation of the electron temperature as can be seen in Figure 5.7. In plasmas produced in atomic gases, there are no vibrational degrees of freedom and consequently the corresponding rate $V(T_e) = 0$. This can explain the relatively high average electron temperature observed in a fs pulse produced argon plasma of $T_e \approx 5500$ K [159]. Since the measurement was based on relative emission line strengths from a Boltzmann plot the reported temperature was an average over about 10 ns (integration time of camera).

Figure 5.8 shows the normalized radial distributions of T_e and N_e at three different time delays for initially Gaussian and flat-top $T_e(r)$ with Gaussian $N_e(r)$ profiles.

The electron temperature at the plasma center relaxes faster compared to the outer regions. This is a result of the dependence of the elastic collision term in Equation 5.12 on the electron density through ν_{ei}. The electron density flattens because of the bimolecular nature of the recombination process. Because the electron density has a Gaussian initial profile, the intensity at the center is the highest. According to Equation 5.11, the recombination is the fastest at the center. As a result, the profile flattens as the delay increases. The electron density distribution can successfully explain the observation of the third harmonic generation with a probe beam passing through an air filament [158].

The start point of the simulations refers to the experimental data at a delay of 35 ps. If we extrapolate the initial values to zero delay the electron temperature would be about 20% higher and the electron density about 50% times larger than the values mentioned before.

Since the experiments were carried out with a 1-kHz pulse train the average ambient temperature of the volume immediately surrounding the plasma is higher than room temperature (300 K). A simple heat diffusion model estimates a temperature increase of a few ten degrees with a FWHM of the distribution of $D \approx 1$ mm. Changing the ambient temperature by 50 K does not affect the previously derived results noticeably. The aforementioned 0.3% diffraction signal at negative delays is a result of this temperature increase and the heat deposition by the preceding single pulse in a cylinder of diameter d.

The classical description of the dielectric constant by the Drude model using effective collision rates is an approximation. The electron - electron collision rate [169] at the center of the plasma is between 3.3×10^{13} Hz and 5.5×10^{13} Hz for delay times between 35 ps and 1200 ps. The sum of the rates for ion - ion and ion - neutral collisions [172] is between 6×10^{11} Hz and 1.0×10^{13} Hz in the same delay range. The reason for the lower collision rates of ion - ion and ion - neutral than electron

- electron is the bigger mass of ions and neutrals than electrons. The corresponding time scales to reach equilibrium are therefore less than 10 ps. The model assumes electrons and ions with well defined energies rather than distribution functions. The electron and ion densities therefore must be considered as averages.

5.5 Wave guiding using one filament

5.5.1 Backscattering through a filament

There are two ways the filament could be helpful to guide an electro-magnetic wave. The first one is using the interchange between self-focusing and defocusing along the propagation of the filament (see Figure 5.9). At the position of the plasma, the refractive index is lower than other places. The longitudinal index change will act

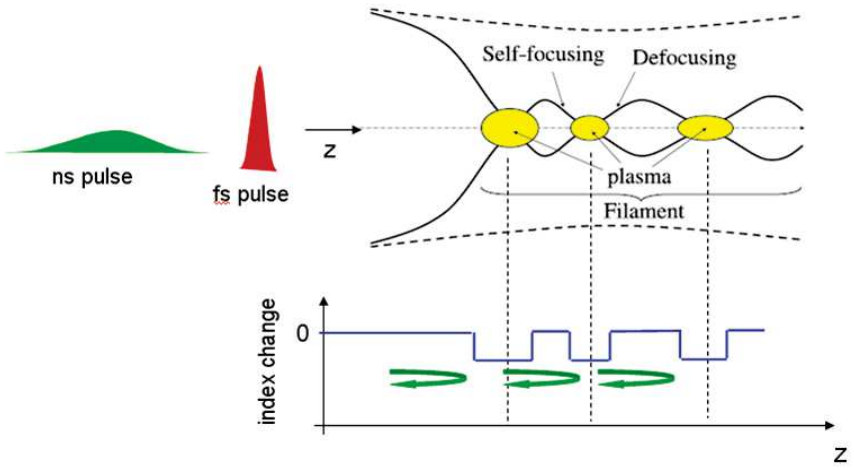

Figure 5.9: Index change along the propagation of a filament. The fs pulse is focused to produce the filament. The latter coming ns pulse could be partially reflected because of the index variation.

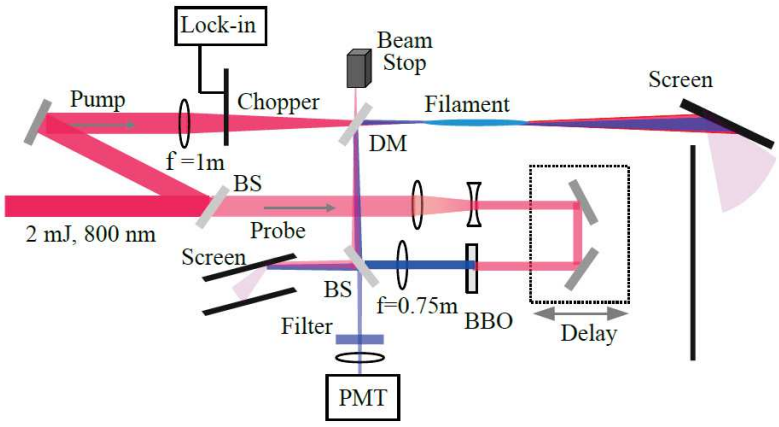

Figure 5.10: Experimental scheme for backscattering measurement along a filament. BS: beam splitter, DM: dichroic mirror, PMT: photomultiplier tube.

like "mirrors" and reflect part of the signal generated by the latter coming ns pulse. This filament is formed by the focusing of a Gaussian beam. From the published work, there is some evidence that the backward scattering is higher than the normal Rayleigh scattering [54, 173].

In order to explore the wave guide properties of the filament, we set up an experiment to measure the backward scattering of the probe beam with the presence of the filament. Figure 5.10 shows the scheme for the experiment. The main beam from the laser was split into the pump beam (87%) and the probe beam (13%). The pump is focused to produce a 5-cm long filament. The probe beam size is reduced to half through a telescope. And then it was converted into second harmonic (400 nm) using a BBO crystal to distinguish it from the pump. The weak probe was focused to pass through the filament. The beam splitter for the 400 nm has a reflection of 50%. The pulse energy of the second harmonic before the filament was around 2 μJ. In this experiment, special care was taken for the unwanted scattering from different surfaces. The pump beam was chopped at 71 Hz and the backscattering signal was picked up by a PMT.

Through the test, we found out that the smallest backscattering change we can measure is about 0.015 ppm. With this sensitivity, we did not observe any backscattering change from the filament. The back scattering of the probe beam is smaller than 0.015 ppm. Using the similar method in Yu's paper [54], we can calculate the Rayleigh backscattering efficiency of 400 nm for our setup being $\sim 4 \times 10^{-10}$. The backscattering of the suppercontinuum was reported to be 2 times of the Rayleigh scattering [54]. For the current setup it could not resolve the scattering change on that order.

5.5.2 Field-free alignment of molecules

As for the transmitted probe beam after the filament, we observed periodic maxima and minima when the delay was changed. We collected the change of intensity at the probe beam center and measured the beam profile at different positions. They are shown in Figure 5.11 and 5.12. The results are in agreement with the field-free alignment of molecules (N_2, O_2 and CO_2) in air observed previously [174, 175] and the associated change in refractive index.

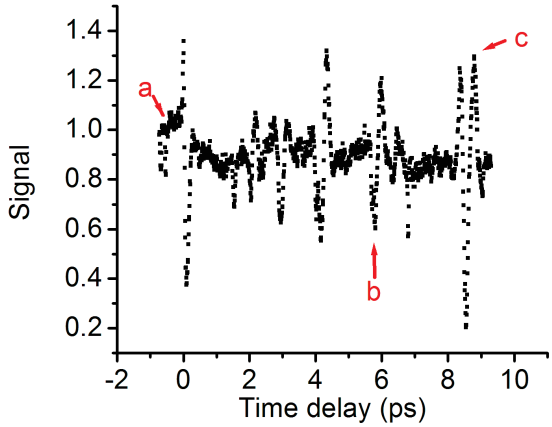

Figure 5.11: The change of the 400-nm probe beam center intensity as a function of delay. Typical beam profile pictures of the probe at different delay positions are shown in Figure 5.12.

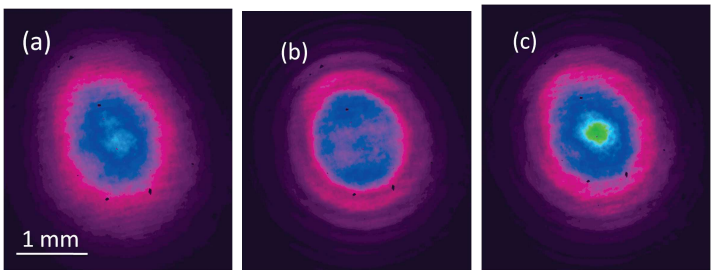

Figure 5.12: Typical beam profile pictures of the probe at different delay positions. (a), (b), and (c) are corresponding to the three positions marked in Figure 5.11.

5.6 Wave guiding with multiple filaments

Except for the idea to enhance the backscattering from a single filament, there is another idea to create a fiber-like wave guide using a donut shape beam. As in a typical fiber, the mechanism of wave guiding is through total internal reflection. The refractive index the fiber core is larger than the index outside. The Laguerre-Gaussian (LG) beam has a donut beam shape [176]. By focusing the LG beam, plasma could be formed in the region of the donut beam. Because of the lower refractive index in the plasma than in the air, this could produce a refractive index difference.

In the propagation of LG beam, the intensity would not normally keep uniform because of noise. Instead, the beam would break apart into individual Townes profiles [177]. This makes the idea of uniform index change similar to a hollow fiber challenging.

There is theoretical work discussing the possibility of guiding signal with an array of plasma filaments [149–151]. Châteauneuf *et al.*. demonstrated microwave guiding over 16 cm in air using a large diameter plasma waveguide hollow in the center (air) [53]. The waveguide was generated with the 100 TW femtosecond laser system (pulse energy: 1.5 J) at the Advanced Laser Light Source facility. The diameter of the waveguide was around 45 mm with about 1030 filaments distributed in the outside ring [53]. The thickness of the wall of filaments varied between 1 and 3 mm along the ring, which was thicker than the skin depth. It is very interesting to know whether the plasmas can help guide waves or not with much lower energy (mJ) laser source. This means that the number of the filaments would be much less.

If the beam consisting of several equal-energy parts can produce filaments from each bead, there is still index change between the center and the outside plasma. A necklace beam can be produced with 0-π phase plate [178]. That setup works

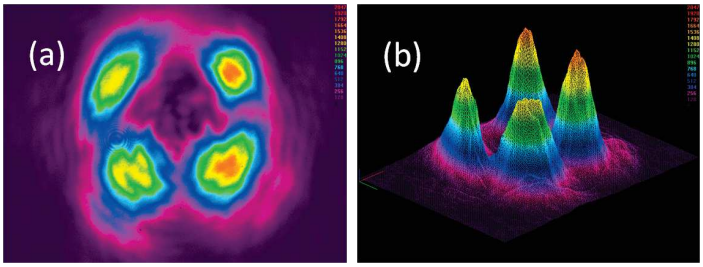

Figure 5.13: A necklace beam from the interference of a LG_{02} beam. (a) 2D intensity profile; (b) 3D intensity profile. This beam was produced by a 40 fs laser at 800 nm.

only for low energy pulses around 10 μJ. In order to produce filament in air, the pulse energy needs to be around several mJ, depending on the number of beads in the beam. Using a hologram [176], we can get an LG beam of maximum energy around 0.3 mJ. Through the interference of the LG beam, a necklace beam consisting several beads can be produced. Considering the limitation of the energy, the number of beads cannot be large. Figure 5.13 shows an example of the interference beam profile consisting of four separate beads.

Another problem is the fusion of filaments [179]. The main reason for the attraction between filaments is because of the Kerr effect. To avoid that, one has to separate temporally the adjacent beads by a pulse duration. Otherwise, the distance between the different single filaments must be larger than $\sim$200 μm [179].

Assuming each filament produces a Gaussian shape index change, we simulated the case for a wave guide consisting of four filaments. The refractive index change distribution is shown in Figure 5.14.

For a plasma wave guide, there is a relation between the guided wave and the size of the wave guide [150],

$$\lambda_{pe} < \lambda \leq R_{wg} \ll L_{pe}, \tag{5.16}$$

where $\lambda_{pe} = 2\pi c/\omega_{pe}$ is the plasma wavelength, λ is the wavelength of the guided

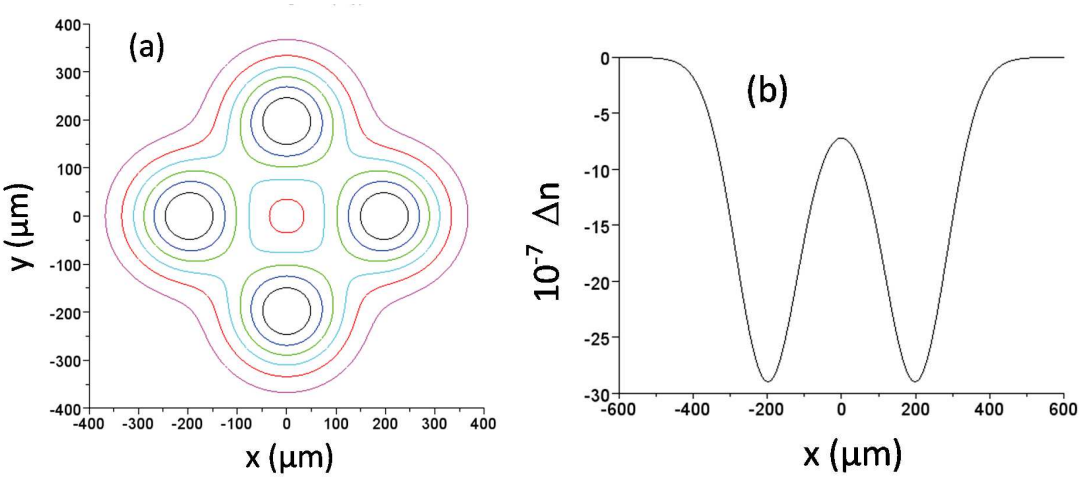

Figure 5.14: Refractive index change in the presence of four filaments. (a): the contour of the index change, (b): index change along y=0. Each filament was assumed having a Gaussian shape for plasma density, with $N_e = 1 \times 10^{22}$ m^{-3} at the center.

wave, R_{wg} is the radius of the waveguide, L_{pe} is the length of the plasma channel.

Plasma densities produced by filaments in air are on the order of 10^{18}m^{-3} to 10^{24}m^{-3} [152–154, 180] (see Section 5.3). At the center of the filament, we assume the average density being 1×10^{22} m^{-3}. The maximum λ_{pe} corresponding to that is 0.3 mm ($\omega_{pe} = 1$ THz). For the outside region, the plasma wavelength is larger. From this, we can see that, the possible wavelength that can be guided is larger than 0.3 mm.

Another relation needs to be satisfied in the plasma waveguide is [150]

$$h_{wg} > \delta = \sqrt{\frac{2}{\omega \mu_0 \sigma}}, \tag{5.17}$$

where h_{wg} is the waveguide wall thickness, δ is the skin depth, ω is the guided wave frequency, μ_0 is the permeability of vacuum, σ is the plasma conductivity. From the maximum λ_{pe}, we can get the minimum δ is 270 μm. From our measurements, the average diameter of the filament (FWHM) is 150 - 200 μm. From this, we can see

that one layer of filaments is not enough to confine the guided wave.

Last, there is loss cause by the plasma cladding for the guided wave (see Section 5.3). According to the expression given in [150], for electron density consider here, the propagation length is smaller than 1 mm for THz wave.

In summary, it is not practical to use several plasma channels to guide electromagnetic signal for long distance using pulse energy of mJ level.

5.7 Chapter summary

In this chapter, we discussed the determination of the transient electron temperature of laser induced air plasmas and the wave guiding properties with single and multiple filaments.

A time-resolved optical method and a kinetic plasma model were developed to determine the transient electron density N_e and the temperature T_e distribution in a fs pulse produced air plasma. The electron temperature decays on a time scale of a few hundred ps. Initial electron temperatures of 3900 K were obtained for initially flat-top temperature and Gaussian electron transverse density distributions with initial peak values of 2.3×10^{23} m^{-3}.

The experimental results were modeled with plasma kinetic theory taking into account elastic and inelastic collisions between electrons, ions, and neutral molecules, including their vibrational degrees of freedom as well as the radial dependence of electron temperature and density. The results indicate the importance of molecular vibrational degrees of freedom in the cooling of the electron gas. While the initial values for N_e and T_e depend on the assumed initial transverse profiles the decay transients are rather independent.

The exploration of guiding signals using plasmas did not show enhanced backward scattering in the presence of a filament. The signal was less than 0.015 ppm from a plasma channel produced by a 2-mJ pulse. Field-free alignment of molecules was observed from the transmitted probe beam.

For wave guiding with multiple filaments, calculations were performed on the wavelength of the guided wave, the required thickness of the plasma layer and the loss of the guided wave. It was found the idea is not practical.

The results discussed in this chapter were published in [158, 162].

Chapter 6

Summary and outlook

6.1 Summary

In this dissertation, we discussed modifications and damage of dielectric materials with laser pulses. The samples were bulk material and thin films. We demonstrated that a damage model based on multiphoton and impact ionization agreed with experimental data in a wide pulse width range, from fs to ns, for nascent films.

The difference between single-pulse and multiple-pulse multiphoton absorption (MPA) coefficients was clarified. The LID test with two-color pulse pair showed that the damage threshold depended on the order of the pulse pair. The LID dependence on the input pulse polarizations was explored with fs and ps pulses. The results provided information for the physics of incubation and its dependence on polarization for thin film damage. The order of structure change was revealed through the observation laser illumination spots in HfO_2 films.

We discussed the validity of the crater size method for multiple-pulse (S-on-1) damage threshold measurements. We checked the agreement between the LIDTs

obtained from the crater size method and the scattering change method. The incubation curves of TiO_2 films from these two methods showed good agreement. We explored LIDTs of bulk metals using the plasma emission method. While Nickel alloy presented good agreement, Aluminum did not. The condition for the crater size method for S-on-1 tests was discussed. The condition for the applicability to S-on-1 experiments is that the beam profile that does change with the pulse energy. An empirical incubation model was introduced for a wide variety of materials. It includes two physical processes: the laser induced change of absorption of the material with every laser pulse and the laser induced change of the specific energy that is necessary to remove an atom or molecule from the material. Evidence for this has been given by fitting incubation curves for a metal, a multi-component alloy and a dielectric film with good agreement.

We discussed the determination of the transient electron temperature and the wave guiding properties with single and multiple filaments. A time-resolved optical method and a kinetic plasma model were developed to determine the transient electron density N_e and the temperature T_e distribution of laser induced air plasmas. The electron temperature decays on a time scale of a few hundred ps. The experimental results were modeled with plasma kinetic theory. The results indicate the importance of molecular vibrational degrees of freedom in the cooling of the electron gas. In the exploration of the signal guiding using plasmas, we did not observe enhanced backward scattering in the presence of a filament.

6.2 Outlook for future work

In the MPA coefficient measurement of thin sapphire plates, a 3-4 photon absorption process fits the results better. According to its band gap, a 6 photon absorption is expected for the incident laser at 800 nm. The exact physical reason is still not clear.

More thoughts and experiments are needed to clear that.

For the two-color two-pulse damage test, experiments was performed on thin HfO_2 films. The results cannot be explained based on the Drude model. In order to draw a general conclusion, more experiments with different color combinations and films would help.

The ripple directions are different with HfO_2 films and TiO_2 films in fs laser damage tests. The ripples in HfO_2 films are strictly perpendicular to the incident laser polarization direction, while the ripples in TiO_2 films do not have a strict direction and the main direction of ripples is parallel to the laser polarization direction. The determination factor for the ripple directions is not clear. For future work, experiments could be performed to explore this.

Appendices

Appendix A

Transformations for a Gaussian pulse

For a Gaussian pulse in spatial and temporal profile, the intensity can be written as

$$I(r,t) = I_0 \cdot \exp\left[-\left(2 \cdot \sqrt{\ln 2} \cdot \frac{t}{\tau}\right)^2\right] \cdot \exp\left[-\left(\sqrt{2} \cdot \frac{r}{w}\right)^2\right], \tag{A.1}$$

where w is beam radius for $I(w) = I_0 \cdot e^{-2}$, τ is the pulse duration (FWHM), and I_0 is the peak intensity.

The following are the transformations between peak intensity (I_0), peak power (P_0), peak fluence (F_0), and pulse energy (E) [181].

$$\begin{aligned} I_0 &= \frac{2}{\pi} \cdot \frac{P_0}{w^2} = 0.637 \cdot \frac{P_0}{w^2} = \sqrt{\frac{4 \cdot \ln 2}{\pi}} \cdot \frac{F_0}{\tau} = 0.939 \cdot \frac{F_0}{\tau} \\ &= \sqrt{\frac{16 \cdot \ln 2}{\pi^3}} \cdot \frac{E}{w^2 \cdot \tau} = 0.598 \cdot \frac{E}{w^2 \cdot \tau} \end{aligned} \tag{A.2}$$

$$\begin{aligned} P_0 &= \frac{\pi}{2} \cdot w^2 \cdot I_0 = 1.571 \cdot w^2 \cdot I_0 = \sqrt{\pi \cdot \ln 2} \cdot \frac{w^2}{\tau} \cdot F_0 = 1.476 \cdot \cdot \frac{w^2}{\tau} \cdot F_0 \\ &= \sqrt{\frac{4 \cdot \ln 2}{\pi}} \cdot \frac{E}{\tau} = 0.939 \cdot \frac{E}{\tau} \end{aligned} \tag{A.3}$$

$$F_0 = \sqrt{\frac{\pi}{4 \cdot \ln 2}} \cdot \tau \cdot I_0 = 1.064 \cdot \tau \cdot I_0 = \frac{1}{\sqrt{\pi \cdot \ln 2}} \cdot \frac{\tau}{w^2} \cdot P_0 = 0.678 \cdot \frac{\tau}{w^2} \cdot P_0$$
$$= \frac{2}{\pi} \cdot \frac{E}{w^2} = 0.637 \cdot \frac{E}{w^2} \tag{A.4}$$

$$E = \sqrt{\frac{\pi^3}{16 \cdot \ln 2}} \cdot w^2 \cdot \tau \cdot I_0 = 1.672 \cdot w^2 \cdot \tau \cdot I_0 = \sqrt{\frac{\pi}{4 \cdot \ln 2}} \cdot \tau \cdot P_0$$
$$= 1.064 \cdot \tau \cdot P_0 = \frac{\pi}{2} \cdot w^2 \cdot F_0 = 1.571 \cdot w^2 \cdot F_0 \tag{A.5}$$

Here are transformations for different beam size parameters and pulse duration parameters.

$$x_{1/e} = \frac{1}{2\sqrt{\ln 2}} \cdot x_{FWHM} = 0.601 \cdot x_{FWHM} = \frac{1}{\sqrt{2}} \cdot x_{1/e^2} = 0.707 \cdot x_{1/e^2} \tag{A.6}$$

$$x_{1/e^2} = \sqrt{2} \cdot x_{1/e} = 1.414 \cdot x_{1/e} = \frac{1}{\sqrt{2 \cdot \ln 2}} \cdot x_{FWHM} = 0.849 \cdot x_{FWHM} \tag{A.7}$$

$$x_{FWHM} = 2 \cdot \sqrt{\ln 2} \cdot x_{1/e} = 1.665 \cdot x_{1/e} = \sqrt{2 \cdot \ln 2} \cdot x_{1/e^2} = 1.177 \cdot x_{1/e^2} \tag{A.8}$$

Appendix B

List of tested films

Table B.1 gives the detail information about the tested films mentioned in this work. For Sc_2O_3 films, more details about fabrication can be found in [81, 182]. The absorption measurements of TiO_2 films can be found in [183].

Sample ID	Film	Thickness (nm)	Technique	Annealing
120602b	HfO_2	216	IBS	Yes
130220b	HfO_2	85	IBS	Yes
111008b	Sc_2O_3	130	IBS	No
111009b	Sc_2O_3	130	IBS	No
120411b	Sc_2O_3	200	IBS	No
120412b	Sc_2O_3	200	IBS	No
c8-3-11-23-10	TiO_2	116	EBE	N/A

Table B.1: Details of the tested films. The films were prepared by two techniques: ion beam sputtering (IBS) and electron beam evaporation (EBE).

Appendix C

Locate sample position

The beam radius near the focus was measured in vertical and horizontal directions with the knife edge method. The results are shown in Figure C.1. Assuming the beam has a Gaussian profile $I = I_0 \cdot exp[-2(x^2/w_{hor}^2 + y^2/w_{ver}^2)]$, the beam radius

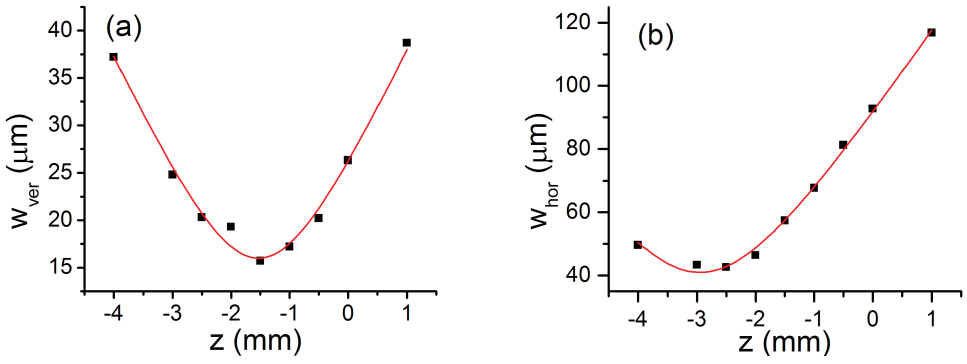

Figure C.1: Beam radius measurements in vertical (a) and horizontal (b) directions along the beam propagation direction. The square dots are the measurements. The red curves are the best fitting using Equation C.1. Notice that the knife edge was placed at Brewster angle. As a result, w_{ver} and w_{hor} are not equal.

$w(z)$ along z follows

$$w(z) = w_0 \cdot \sqrt{1 + \frac{(z - z_c)^2}{z_0^2}}, \tag{C.1}$$

where w_0 is the beam waist (smallest beam radius), z_c the position of beam waist and z_0 is the Rayleigh range. For a Gaussian spatial beam, to calculate the pulse fluence from pulse energy, we can define the effective beam area on the sample as

$$A = \frac{1}{2}\pi w_{hor} \cdot w_{ver}. \tag{C.2}$$

If we insert the results of the fit to the measurements into Equation C.2, we get the minimum effective area and the position of the maximum fluence. It is at $z = 2.0$ mm with $w_{hor} = 46.4\mu m$ and $w_{ver} = 19.3\mu m$ (see Figure C.1). Notice that the knife edge was placed at an incident angle of 60^o. That is why w_{hor} is about two times of w_{ver}. The effective area is $1.32 \times 10^{-5}\text{cm}^2$.

Appendix D

Spatial and temporal overlap procedures

The procedures for the spatial overlap of the IR and UV beams in the two-color pulse pair damage tests (see Chapter 3.6) will be presented here.

First, steer the IR and UV beams so that their fluorescence can be observed on a paper card at the same time. For the UV beam, the fluorescence is bright. So it needs to be reduced. In addition to reducing the pulse energy almost to the minimum with the half-wave plate and polarizer (prism), a reflective UV neutral density filter (O.D.=2.5) was inserted to reduce the pulse energy. Observe the overlap immediately after the dichroic mirror on which UV and IR pulses combine. Tune the dichroic mirror before the UV focusing lens to move the UV beam over the IR beam.

Second, put a 100-μm thick brass sheet at the position of the sample. Increase the IR pulse energy so that a hole is drilled through the metal. The transmission can be observed behind the hole with a IR fluorescence card. Once the hole is drilled, reduce the IR energy but still high enough so that the IR transmission can still be observed with the IR card. Leave the UV beam at low energy. Tune the dichroic

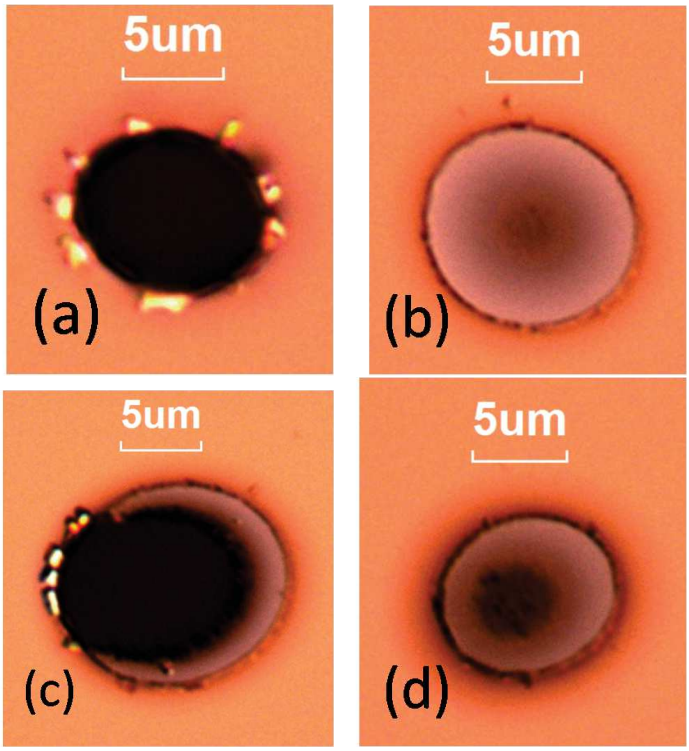

Figure D.1: Crater images by a single IR (a), UV (b) pulses and two-color pulses (c) and (d). The spatial overlap of the two pulses can be checked from the craters illuminated by both pulses. The images are obtained by a Nomarski microscope. The change in color in the images represents the variation of the phase of the interference color.

mirror to steer the UV through the hole. Once the UV propagates collinearly with the IR beam, the UV transmission should reach the maximum.

Third, the sample is placed in the sample holder. Damage craters are produced by each pulse without the other being present. The IR crater and UV crater can be identified (see Figure D.1 (a) and (b)). The crater images are different in color under a Nomarski Differential Interference Contrast microscope. This is because the craters are introducing different phase variations for the incident microscope illumination color. By observing the damage craters by both pulses, the overlap

is checked and confirmed (see Figure D.1 (c) and (d)). If the overlap needs to be adjusted, repeat the above procedures again. Figure D.1 show some microscope images of craters produced by single IR and UV pulses and two-color pulses.

Once the first two steps are finished in the spatial overlap, the next step is to align the temporal overlap. Move the sample mount along the beam propagation direction by several millimeters. This is to leave space for a holder of a sapphire plate at the position of the sample. For a coarse search of zero time delay (ZTD), a 500-μm thick sapphire plate is put close to the position of the sample. Increase the UV pulse energy to around 4 μJ but leave the IR pulse at low energy, around 0.44 μJ. Move the delay line from negative to positive end, observe the IR transmission with an oscilloscope.

For an IR pulse, when the closest UV pulse arrives at the sapphire before the IR pulse, the absorption of the IR pulse will not affected. When the UV pulse arrives at the sapphire after the IR pulse, the absorption of the IR pulse will be increased. The delay position of the IR pulse transmission change is where the two pulses overlap.

Replace the thick sapphire with a 50-μm thick fused silica, perform similar scans to find ZTD. Because the life time of CB electrons is much shorter for fused silica ($\sim$ 100 fs) [41], the transmission dip is much narrower near ZTD. A transient transmission for the IR pulses near ZTD is shown in Figure D.2. The valley of the curve is the position of ZTD. In our test, the IR pulse is placed 100 fs earlier and 100 fs later than the UV pulse. The LIDT is measured for these two cases.

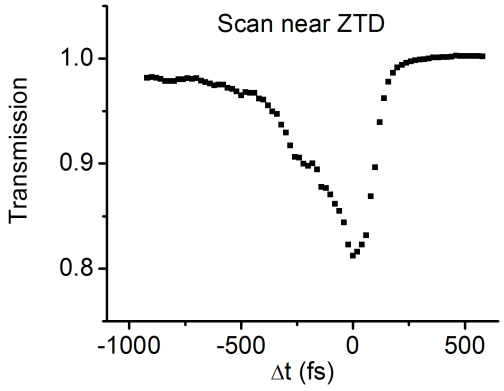

Figure D.2: The transmission of the IR pulse as a function of the delay between IR and UV pulses. The sample was a 50-μm thick fused silica plate. Positive delay means the IR pulses arrive at the sample earlier than the UV pulses. The asymmetry is a result of the laser induced defects by the UV pulses. The plot is an average over five scans.

Appendix E

Optimized film thickness for two-color damage test

Due to the small thickness and the nominal transparency of thin dielectric films, Fabry-Perot resonances occur for femtosecond laser pulses. The local intensity distribution in a single film on a substrate is given by (see Page 23 in Reference [184])

$$I_{loc}(t,z) = I_{inc}(t) \times \xi(z), \tag{E.1}$$

where

$$\xi(z) = \left| t_{12} \frac{1 + r_{23}\exp[i2k_0(z-d)]}{1 + r_{12}r_{23}\exp(-i2k_0 d)} \right|^2. \tag{E.2}$$

Here $k_0 = 2\pi n_0 \cos(\theta_p)/\lambda_p$, where λ_p is the center wavelength of the pump, θ_p is the propagation angle of the pump in the film, d is the thickness of the film, and $r_{ij}(t_{ij})$ are the amplitude reflection (transmission) coefficients for the interface from medium i to medium j. $I_{inc}(t)$ is the incident intensity.

Note that $\xi(z)$ is a periodic function of z and its maximum value can be used to calculate the maximum laser fluence inside the film from the incident fluence. For an 85-nm thick HfO_2 film on a fused silica substrate, the local intensity distribution

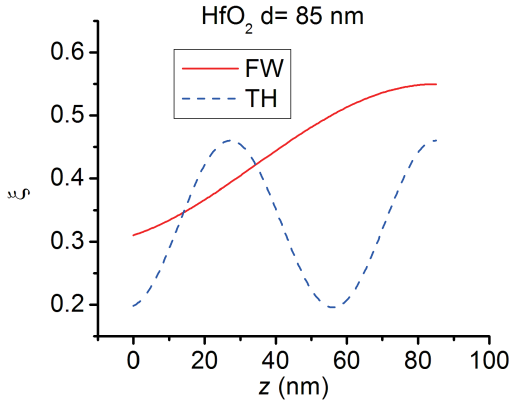

Figure E.1: $\xi(z)$ for an 85-nm thick HfO_2 film on a fused silica substrate with FW ($\lambda = 800$ nm) and TH ($\lambda = 267$ nm) pulses. $z = 0$ is the interface of air and the film. $z = 85$ nm is the interface of the film and the substrate.

of an IR and UV pulses in the film is shown in Figure E.1. The maximums of the two pulses meet at the back surface of the film.

One aspect of improving the two-color damage test is to optimize the thickness of the film so that the maximums of the two pulses happen close to the front surface (air/film) of the film. This can avoid the disturbance of nonlinear processes inside the film. Simulations were performed with HfO_2 and TiO_2 films using Equation E.2. The combinations of different colors include fundamental wave (FW) + third harmonic (TH) and FW + second harmonic (SH). Through simulation, the ranges of the film thickness were found (see Table E.1). The physical parameters used in the calculation are listed in Table E.2. The typical intensity distributions for each case are shown in Figure E.2 and E.3.

Film	Colors	d_{low}	d_{high}	Mean	Error	Rel. error (%)	ξ_1	ξ_2
HfO_2	FW + TH	400	410	405	5	1.2	0.67	0.64
HfO_2	FW + SH	186	205	195.5	9.5	4.9	0.66	0.66
TiO_2	FW + TH	158	177	167.5	9.5	5.7	0.56	0.20
TiO_2	FW + SH	499	511	505	6	1.2	0.55	0.55

Table E.1: Optimized films thickness in two-color damage tests. The unit of the films thickness is nm. The low limit (d_{low}) and the high limit (d_{high}) are set for the intensity at the front film surface being within 5% of the maximums for both colors. ξ_1 and ξ_2 are for FW and harmonics (TH or SH) respectively calculated from the optimized film thicknesses.

Color	λ (nm)	HfO_2 film	TiO_2 film	Fused silica
TH	267	2.3	2.7	1.5
SH	400	2.05	2.82	1.47
FW	800	1.98	2.39	1.45

Table E.2: Refractive indices used in the calculation of ξ. The data for HfO_2 film, TiO_2 film and fused silica are from ltschem.com, filmetrics.com and sciner.com, respectively.

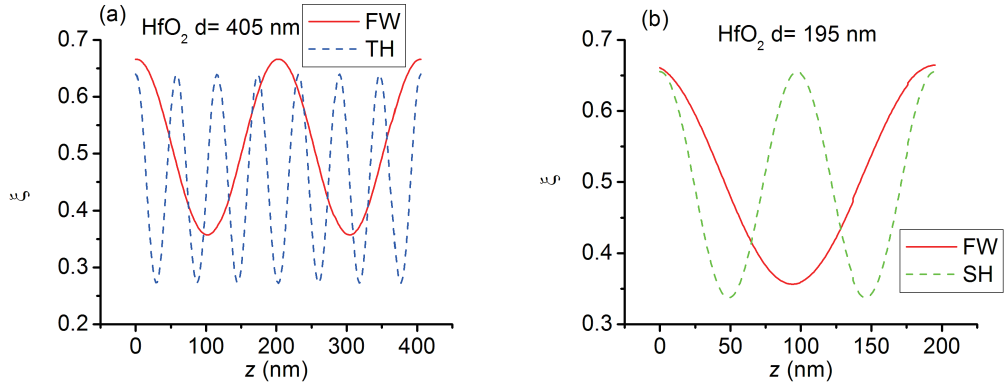

Figure E.2: (a), $\xi(z)$ for a 405-nm thick HfO_2 film on a fused silica substrate with FW and TH pulses. (b), $\xi(z)$ for a 195-nm thick HfO_2 film on a fused silica substrate with FW and SH pulses. $z = 0$ is the interface of air and the film.

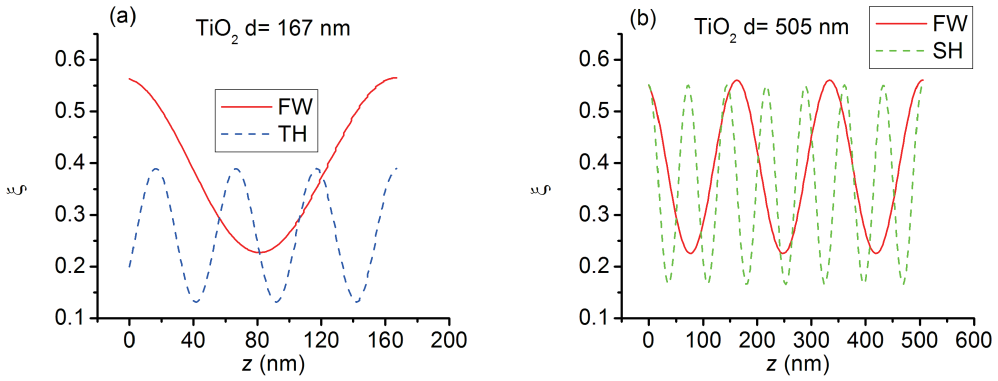

Figure E.3: (a), $\xi(z)$ for a 167-nm thick TiO_2 film on a fused silica substrate with FW and TH pulses. (b), $\xi(z)$ for a 505-nm thick TiO_2 film on a fused silica substrate with FW and SH pulses. $z = 0$ is the interface of air and the film.

Appendix F

Ripples produced by circular polarization pulses

As for the effects of circularly polarized pulses to ripple direction, there are some confusion from the published work.

The difference in ripple directions with left and right circularly polarized light was first reported in [115]. There was no clear explanation for this observation in their work [112,114,115]. It was reported that the left and right circularly polarized pulses produce ripples orthogonal in direction [111]. However, the explanation provided cannot be justified. Because the beam illuminates the sample normally, there is no preferred direction.

In [115], it mentioned for an elliptically polarized beam, the ripples are aligned perpendicularly to the elongated axis [185]. For our experimental setup, there is a 7% intensity difference for along the 45 and -45 degree. It is found that in general the ripples are perpendicular to the elongated axis if it is treated as an elliptical polarized beam (see Figure 3.35).

Appendix G

Ripples characterized by SEM and PTM

G.1 Line and ripple structures characterized by SEM

An example of structures consisting of lines and ripples was checked under a scanning electron microscope (SEM). This test was performed using a facility in Institute of Meteoritics at UNM with the help of Mike Spilde. The back scattering image shows the morphology of the crater (see Figure G.1). It shows the contrast of the components on the film surface. For larger atomic number element, the image is brighter. In the tested sample, the related elements are Hafnium (M= 72), Silicon (M=14) and Oxygen (M=8). The non-damaged area is brighter than the ripples and lines. The detail measurements on SEM show that the thickness of the film in the line and ripple region is lower than the non-damaged area (see Figure G.2 (a)). For the ripple region the film thickness is reduced by 60 nm on average. For the region close to the line structure, the film is even thinner by 80 nm. This is an indication

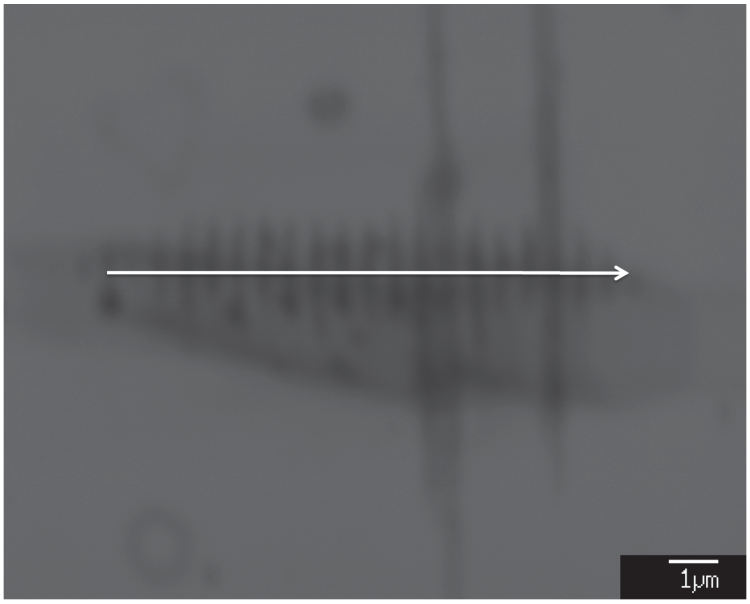

Figure G.1: SEM image of ripple structures shown in Figure 3.37. The arrow shows the trace of a detail scan performed from the left side of the ripple structure to the right side.

of film removal by laser pulses.

The component ratio of Hafnium to Oxygen is also changed. It changed from 2.0 to 1.5 for the ripples. For the region of lines, it goes to even lower to 1.2 (see Figure G.2 (b)). However, for the ripples region, the atomic weight of Silicon from the substrate is not change on average. For the line structure region, the Silicon weight is 2.6 times of the non-damaged area ($\sim$0.3%) on average (see Figure G.2 (c)).

The spatial resolution along the scan direction is on the order of 1 μm. The period of the ripples is 0.54 μm. Therefore, it can not differentiate the details of the ripples.

From the results, we can see that the line structure is quite different as the ripples.

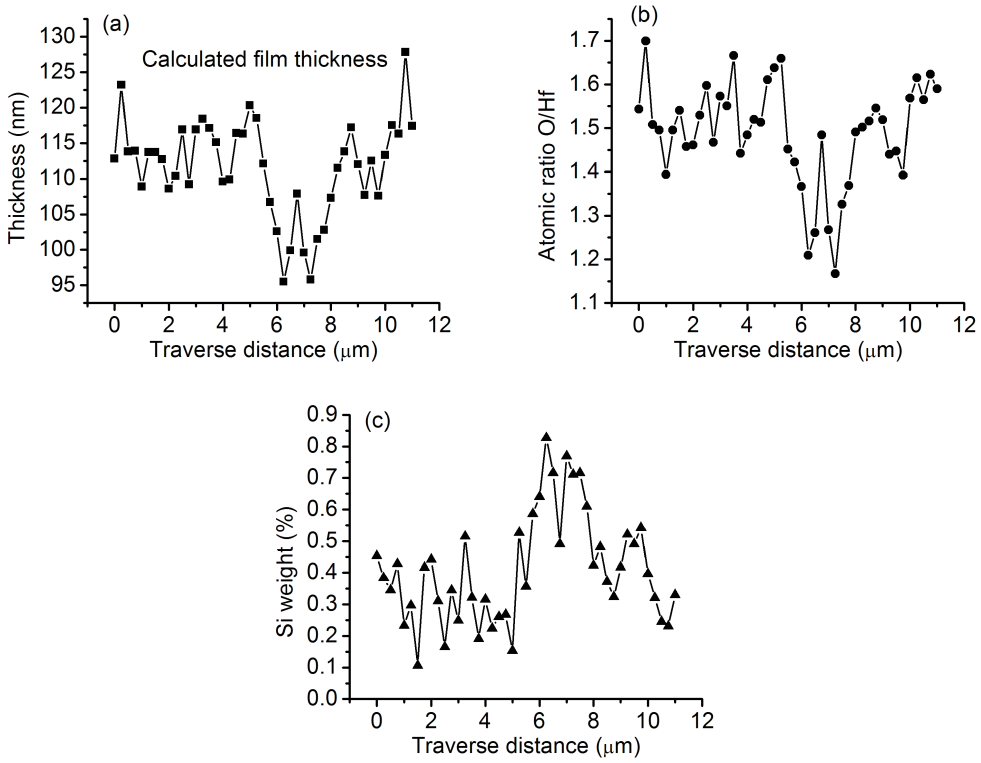

Figure G.2: Detail changes across ripple structures using SEM. A distance of 11 μm was scanned with a step of 0.25 μm. The trace of the scanning is shown in Figure G.1. (a) calculated film thickness, (b) atomic ratio between O and Hf, and (c) Si weight.

In general, the change to the line structure is more significant than the ripples.

G.2 Absorption change on the ripples

In order to check the physical properties change for the ripples, the absorption is checked under a photo-thermal microscopy (PTM) setup. A scheme of the setup is shown in Figure G.3. It is found that the best signal to noise ratio happened when the chopper is running at 1 kHz. When there is a small absorption inside the thin film, the optical thickness of the film $(n \cdot t)$ is changed, where is n is the thin film refractive index and t is the thickness. It will change the reflection as a result of Fabry-Perot interferometry effect. The reflection signal is detected by a photodiode (PD). The change of the reflection because of the small absorption is picked out by a lock-in amplifier connected with the PD. The diameter of the probe beam is about 1.1 μm. The pump beam diameter is about 0.4 μm.

The setup is sensitive to small absorption. Before the experiment, the setup is

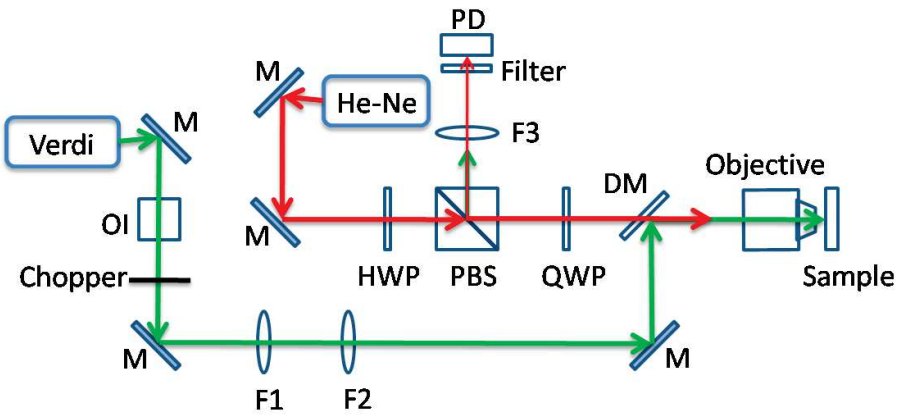

Figure G.3: Photothermal microscopy setup. Verdi: pump laser at 532 nm, maximum output power: 5 W, He-Ne: probe laser at 633 nm, output power: 1 mW, OI: optical isolator, M: mirror, F1: f=2.5 cm lens, F2: f=12.5 cm lens, DM: dichroic mirror, Objective: N.A.=0.95, HWP: half-wave plate, PBS: polarizing beam splitter, QWP: quarter-wave plate, F3: f=10 cm lens, Filter: red pass filter, PD: photodiode (Thorlabs APD110A2).

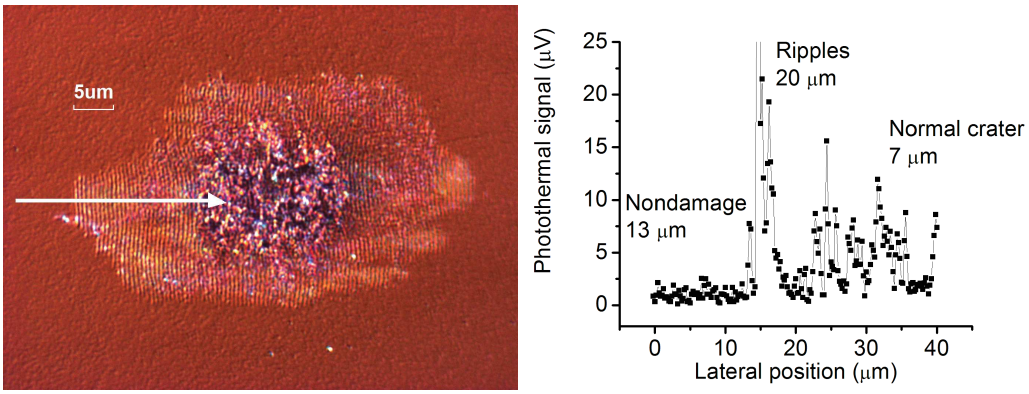

Figure G.4: PTM signal across non-damage and ripples on HfO_2 film. The left image shows the crater under microscope. The arrow indicates the scanning direction and the position of the scan. The right figure shows the change of signal along the lateral position. The length of different structure area is notified.

calibrated by a reference sample whose absorption is known. The smallest absorption that can be resolved by the setup is around 20 ppm. From the test, the spatial resolution of the signal is about 0.5 μm (FWHM) [117].

A scan for the fs laser illuminated HfO_2 film is shown in Figure G.4. The average signal of the ripples area on the crater edge is about 8 times as high as the average over the non-damage area. This is a quite significant increase.

Based on the absorption increase from the undamaged film area to the ripples, it easy to understand that damage would happen at lower fluences once the ripples were formed.

Appendix H

Crater shape dependence on the input polarization direction

In order to characterize the crater morphology dependence on the incident beam polarization, we tested the film near threshold fluence (F(S)≈1.2 F_th(S)) for dif-

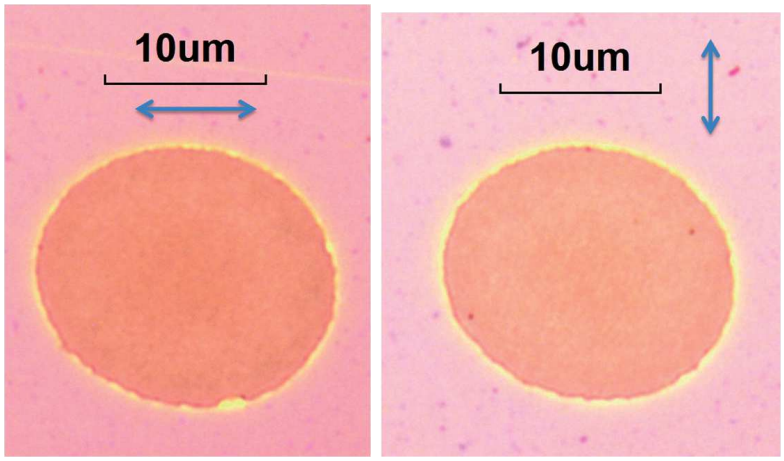

Figure H.1: Crater images ($S = 1$) on TiO_2 near threshold with different polarization directions. Input pulse fluence F=0.80 J/cm^2. The arrows show the polarization directions. There was no ripples on the edge of the craters.

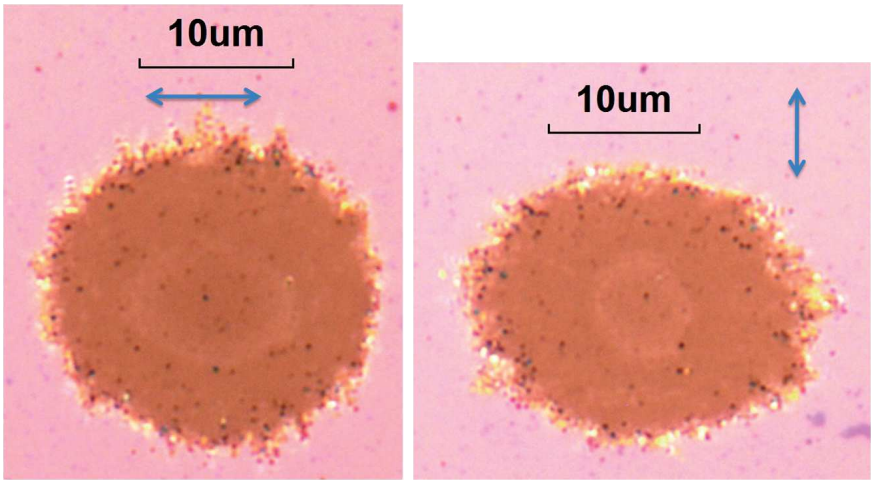

Figure H.2: Crater images ($S = 10$) on TiO_2 near threshold with different polarization directions. Input pulse fluence F=0.62 J/cm^2. The arrows show the polarization directions. The shapes of the craters already show the difference.

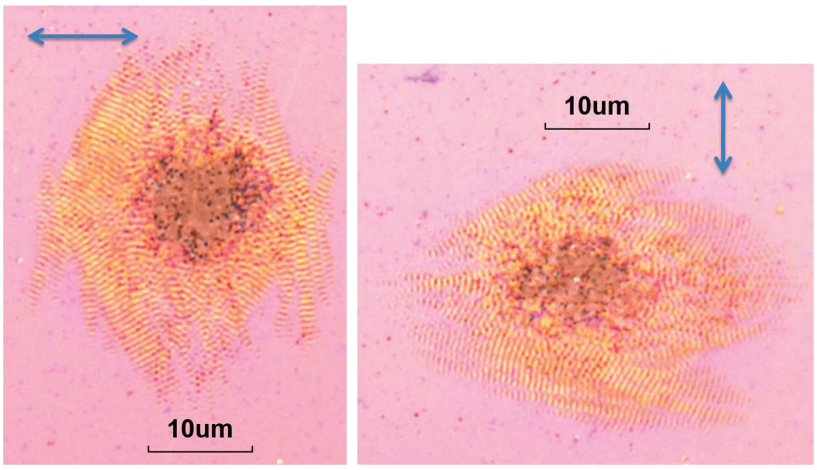

Figure H.3: Crater images (S=10k) on TiO_2 near threshold with different polarization directions. Input pulse fluence F=0.35 J/cm^2. The arrows show the polarization directions. The shape of the craters cannot simply be characterized by a simple elliptical shape.

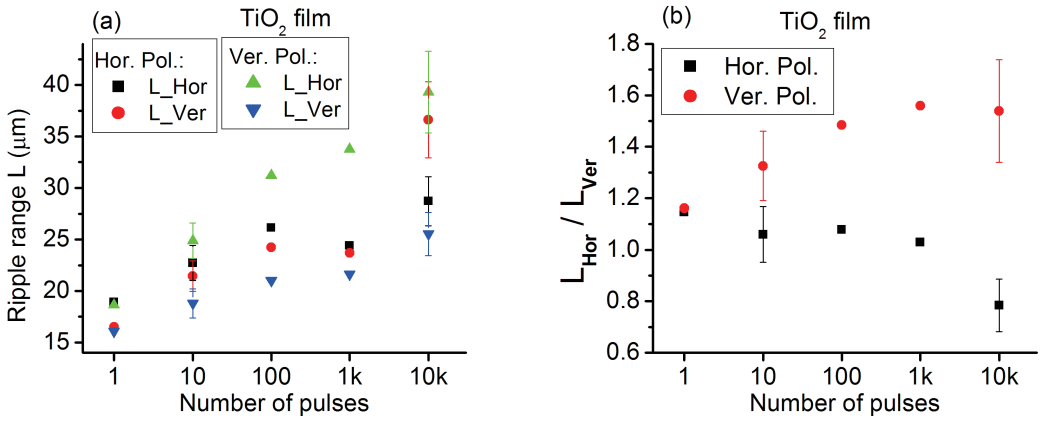

Figure H.4: The ripples ranges L_{hor} and L_{ver} for different polarization directions (a) and their ratio (b). The error bars show the 3σ by repeating the damage tests 10 times under the same conditions. σ is the standard deviation.

ferent number of pulses. The beam polarization was switched between horizontal and vertical directions using a half-wave plate. The craters were checked under a microscope. Representative crater images are shown in Figures H.1, H.2 and H.3. For large S, the craters near threshold cannot be characterized simply by a simple elliptical shape (see Figure H.3). Instead, the expanding ranges of the ripples along horizontal and vertical directions were used here to characterize the craters. The ratio of the horizontal ranges to the vertical ranges is shown in Figure H.4. From the results it is clear that the crater shape depends on the input polarization direction.

Appendix I

Hole drilling with different beam size

Except for the ablation threshold, a practical interest is the aspect ratio of holes drilled with ultrashort pulses. The aspect ratio of a hole is the ratio of its depth to its diameter.

We studied the depths of the holes dilled on different samples with three different beam sizes by changing the position of the sample. In each case, there is no air plasma observed for the energy used at the sample position before placing the sample into the beam path. A series of holes were drilled with different number of pulses.

The beam sizes were measured with the knife edge method. The depth and diameter of the holes were measured using an optical microscope. The crater depth results are shown in Figure I.1. We can see that Nickel alloy and stainless steel have similar behavior and Aluminum has a different behavior. As the beam size decreases, there is a depth limit for all the samples. For all three beam sizes, no through hole for Aluminum was produced. The probable reason for this is that the Aluminum is pure metal, while the other two are alloys.

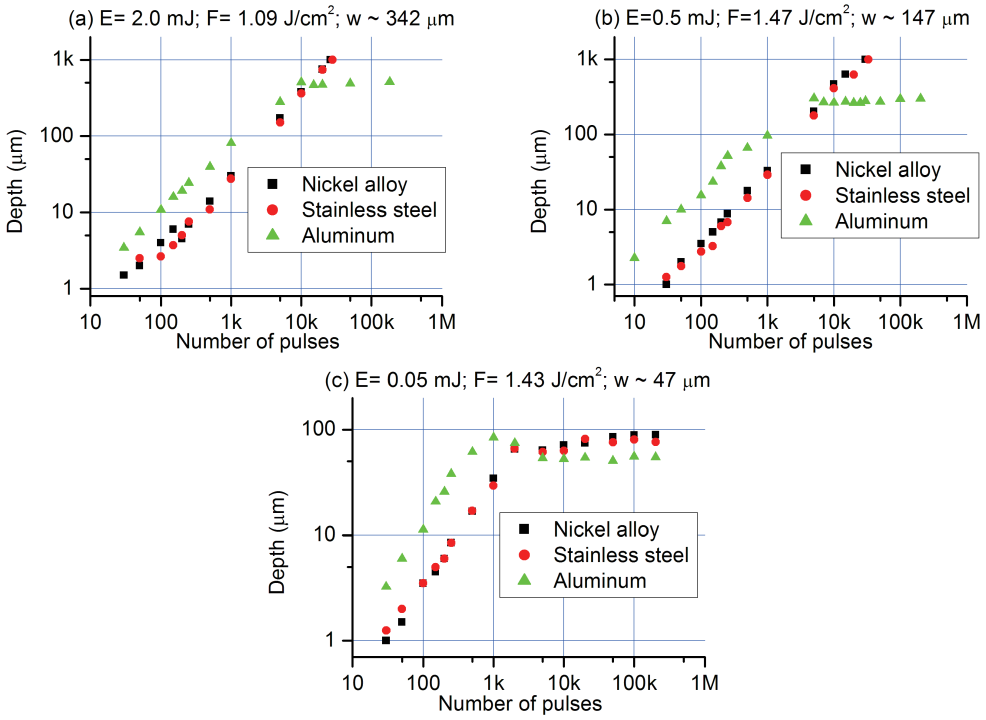

Figure I.1: The crater depth as a function of the number of pulses with different laser beam sizes. For (a) and (b), Nickel alloy and stainless steel were drilled through with large number of pulses. While in (c), the depth reaches a maximum of around 100 μm for all metals.

Appendix J

Estimation of single pulse ablation depth and threshold fluence

There is a linear relationship between the hole depth and the number of pulses S before the depth reaches plateau (see Figure I.1). By linear fitting the results, the depth for single pulse ablation can be extrapolated. For metals, the depth for single pulse is on the order of the skin depth for 800 nm light [126]. It can be estimated by (see Section 5.6)

$$\delta = \sqrt{\frac{2\rho_e}{\mu_0 \omega}} \tag{J.1}$$

where ρ_e is electrical resistivity, $\mu_0 = 4\pi \times 10^{-7}$ T-m/A is permeability of vacuum, ω [rad/s] is the angular frequency of the input laser. $\omega = 2\pi c/\lambda$, where $c = 3.0 \times 10^8$m/s

Metal	$\rho_e[\Omega \cdot \mathrm{m}]$	δ[nm]
Nickel alloy 625	1.29×10^{-6}	29.5
Stainless steel A286	9.10×10^{-7}	24.8
Aluminum 6061 T6	3.99×10^{-8}	5.5

Table J.1: Calculated skin depth for different metals with an 800 nm laser.

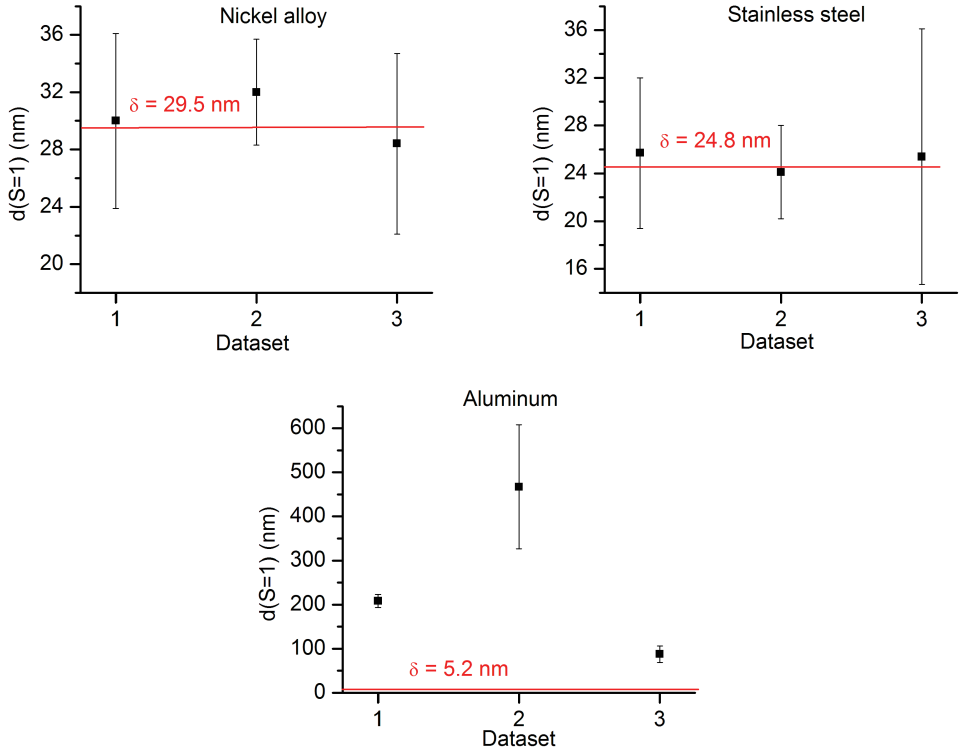

Figure J.1: The extrapolated ablation depth for single pulse, d(S=1) and the calculated skin depth δ for different metals.Dataset 1, 2 and 3 are corresponding to the results shown in Figure I.1 (a), (b) and (c) respectively. The calculated skin depth values are from Table J.1. The error bars came from the linear fit.

is the speed of light in vacuum, $\lambda = 800$nm is the input laser wavelength.

The electrical resistivity near room temperature for the metal can be obtained from the supplier's (McMaster-Carr) data sheet. The parameters and calculation results are listed in Table J.1. Figure J.1 shows the extrapolated $d(S = 1)$ and the calculated δ for different metals. There is a good agreement for Nickel alloy and stainless steel . But for Aluminum, the results fluctuates more and are off the calculated skin depth ($\delta = 5.2$ nm). One possible reason for that is that the surfaces of the Aluminum are rougher than the other two.

	Nickel alloy 625	Stainless steel A 286	Aluminum 6061-T6
Nickel	47-64	24-27	None
Iron	Max. 5	47-62	Max. 0.7
Aluminum	None	None	95.8-98.6
Chromium	20-23	13.5-16	None
Molybdenum	8-10	None	None
Columbium	1-3	None	None
Tantalum	1-3	None	None

Table J.2: The chemical composition of the metals. The composition weight is got from the McMaster-Carr online data sheet.

As for the energy needed for ablation, to first order, it is close to the energy needed to sublimate the illuminated volume [126]. If we assume the vapor has the same temperature as the solid, the heat of sublimation can simply be expressed as the sum of the heats of fusion (melting) and vaporization,

$$\Delta H_{sub} = \Delta H_{fus} + \Delta H_{vap}. \tag{J.2}$$

In this way, we can express the threshold energy for single pulse ablation by

$$E_{th}(S=1) = \Delta H_{sub} \cdot \frac{\rho V}{M} = \Delta H_{sub} \cdot \frac{\rho A \delta}{M} \tag{J.3}$$

where V is the ablation volume, ρ is the density, A is the ablation area, and M is the average molar mass. By assuming the ablation area being the same as the laser beam size on the sample on the first order, the ablation threshold fluence can be written as

$$F_{th}(S=1) = \frac{E_{th}(S=1)}{A} = \Delta H_{sub} \cdot \frac{\rho \delta}{M}. \tag{J.4}$$

For the metals used in the experiment, they are a mixture of different components. Table J.2 lists the chemical compositions of the samples and Table J.3 lists their

	ΔH_{fus} [kJ/mol]	ΔH_{vap} [kJ/mol]	ΔH_{sub} [kJ/mol]	M [g/mol]
Nickel	17.48	379	396.48	58.7
Iron	13.81	340	353.81	55.8
Aluminum	10.71	284	294.71	27.0
Chromium	21.00	347	368.00	52.0
Molybdenum	37.48	598	635.48	96.0
Columbium	30.00	690	719.90	92.9
Tantalum	36.57	753	789.57	180.9

Table J.3: Physical properties of the compositions. These data are obtained from Wikipedia.

	ΔH_{fus} [kJ/mol]	δ [nm]	ρ [kg/m^3]	M [g/mol]	F_{th} cal. [mJ/cm^2]	F_{th} exp. [mJ/cm^2]	Ratio (exp./cal.)
Ni.	425	29.5	8.58×10^3	63.8	169	168	1.00
Steel	368	24.8	8.03×10^3	56.0	131		
Al.	295	5.20	2.70×10^3	27.0	15	180	11.7

Table J.4: Calculation of $F_{th}(S = 1)$ from heat of sublimation. Ni.: Nickel alloy 625, Steel: Stainless steel A 286, Al.: Aluminum 6061-T6. F_{th} exp. values are taken from the ablation area measurements.

physical properties. Based on these we can calculate the average ΔH_{sub} and M for the samples. ρ is got from the supplier's data sheet. δ is from Table J.1.

The results of average threshold fluence are listed in Table J.4. From the results, we can see that there is good agreement between the calculation and experiment for Nickel alloy. For stainless steel, we don't have the experimental results. There is a huge discrepancy for Aluminum.

Appendix K

Additional ablation tests of Nickel alloy

K.1 Plasma emission with large fluence

For Nickel alloy, the pulse fluences should be close to the ablation threshold. For large fluences, the 633 nm emission increases nonlinearly with fluence. Figure K.1 shows the results with larger input pulse fluences for Nickel alloy.

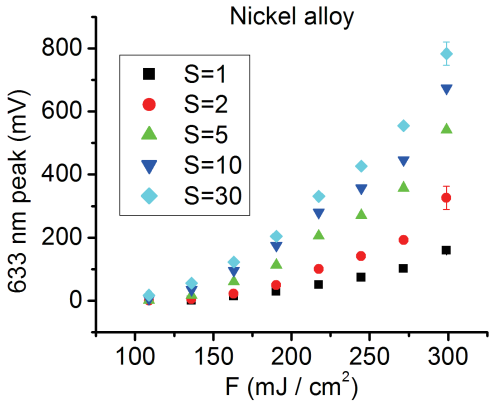

Figure K.1: Plasma emission at 633 nm versus input pulse fluence for Nickel alloy with large input pulse energy. The 633 nm peaks were collected for a burst of 30 pulses. Signals at several representative S are plotted. Each data point is an average over four spots. The error bar is the standard deviation of the measurements.

K.2 Effect of laser repetition rate

In the experiment, the laser repetition rate was 1 kHz. This means the separation between pulses is 1 ms. In order to observe the effect of laser repetition rate to

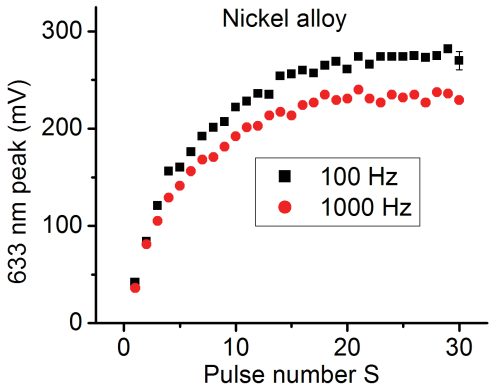

Figure K.2: Plasma emission at 633 nm as a function of the pulse number with different laser repetition rate: 100 and 1000 Hz. The test was conducted on Nickel alloy with pulse energy $E \approx 400\ \mu$J ($F \approx 217$ mJ/cm^2). Each curve is an average over four tests under the same condition.

the plasma emission, we changed it to 100 Hz using a digital delay/pulse generator (Stanford Research System DG535), see Figure K.2. There is about 20% difference between the two curves. To eliminate this effect, an exploration with lower repetition rates needs to be conducted for the future work.

K.3 Observation of an organic layer removal

Among the three metals, Nickel alloy has the smoothest surface. More experiments were therefore conducted with Nickel alloy to obtain a better overall sensitivity. When the avalanche photodiode P2 (cf. Figure 4.7) was replaced by a photomultiplier tube (PMT) (Hamamatsu H5784-01, spectral response: 300-850 nm), the sensitivity was increased about 200 times. Three narrow interference filters centered at 633 nm and two 0^o 800 nm mirrors were inserted before the PMT to suppress scattered light. The PMT signal was much longer (FWHM $\approx$15 μs) compared to the APD.

Using this setup, the emission was observed during bursts of 80 pulses at 4 fluences below the single-pulse threshold ($F_{th} = 155$ mJ/cm^2). The data are shown in Figure K.3. At the highest fluence ($F = 108$ mJ/cm^2), plasma emission was observed from the very first pulse (see Figure K.3 (a)) unlike the same test using the APD. The emission increased with successive pulses before decreasing in the second half of the pulse train. At the next highest fluence ($F = 82$ mJ/cm^2), the behavior was more complicated (see Figure K.3 (b)). The plasma emission occurred with the first pulse, but instead of increasing, it dropped during the first 13 pulses. Afterwards, the emission increased marginally before dropping again near the end of the pulse train. Figure K.3 (c) shows that at $F = 54$ mJ/cm^2, the plasma emission drops with each successive pulse and is gone before the end of the pulse train. At the lowest fluence ($F = 15$ mJ/cm^2) only noise was observed (see Figure K.3 (d)).

The observation in Figure K.3 cannot be simply explained by incubation effect

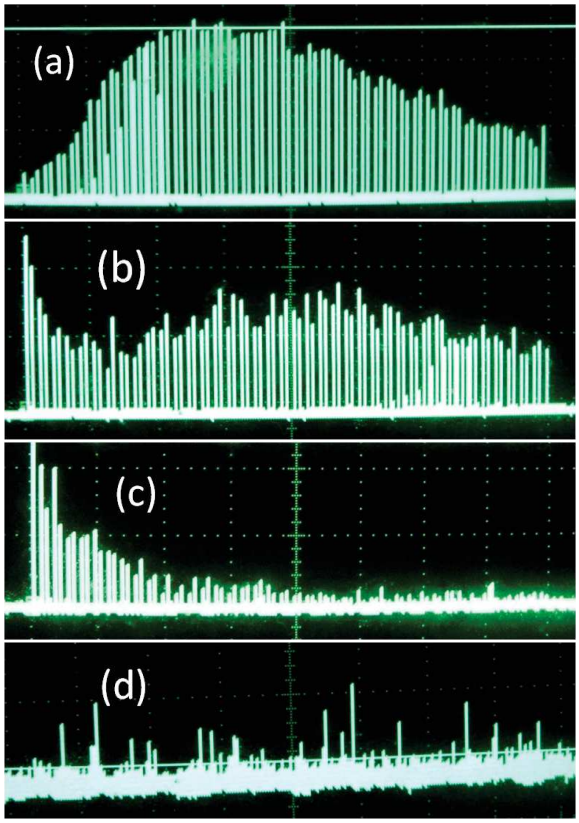

Figure K.3: Plasma emission of Nickel alloy detected by a PMT at different fluences: (a) $F = 108$ mJ/cm^2, (b) $F = 82$ mJ/cm^2, (c) $F = 54$ mJ/cm^2) and (d) $F = 15$ mJ/cm^2. The signals were collected for a burst of 80 pulses.

related to the initiation of metal ablation. If the plasma emission was from the ablation of metals, we would expect to observe the emission start to increase from zero after a certain pulse. Instead, there was always plasma emission observed for the early pulses above $F = 27$ mJ/cm^2). Surprisingly, we observed a decreasing trend with the early pulses.

Such signals may come from the ablation of an organic layer left after the cleaning with acetone. The ablation threshold of this organic layer is much lower than that of the metal. The decrease of the signal in Figure K.3 (c) as the pulse number increases

represents the removal process of this layer with laser pulses. If the fluence is close to a multipulse ablation threshold of the metal, we would see the emission increases again after the organic layer was removed, which represents the ablation of metal (see Figure K.3 (b)). In Figure K.3 (a), there were two group of signals overlapped together for the early pulses: the decreasing signal from the organic layer removal and the increasing signal from the metal ablation. That is why the signal was not zero for the early pulse in Figure K.3 (a).

For the observation with the APD, because the signal from the organic layer was lower than the noise level, it did not affect the calculation of the metal ablation threshold shown in Figure 4.16 (b). That is why we see the good agreement from the two methods.

Appendix L

Derivation of absorption coefficient and specific energy

To describe the incubation effect, a phenomenological model is built. The model includes two basic assumptions: incubation is controlled by an increase of the energy deposition per pulses (absorption) and a decrease in the critical energy H needed to damage (ablate) the material over the pulse train. The latter one is also called material fatigue.

For the absorption coefficient α change during the pulse train, we make the following ansatz

$$\frac{d}{dS}\alpha(S,F) = -\beta(\alpha - \alpha_{max})F - (\alpha - \alpha_0)n \tag{L.1}$$

where S is the pulse number, F is the fluence of the incident pulse, β is a material parameter describing the efficiency with which a pulse of fluence F changes the absorption coefficient toward a maximum α_{max}, α_0 is the initial absorption coefficient, and $n = T/\tau$, is the ration of the pulse period T and recovery time τ of the ablation change.

The solution of Equation L.1 can be expressed as

$$\alpha(S,F) = \alpha_0 e^{-(\beta F+n)S} + \frac{\beta\alpha_{max}F + \alpha_0 n}{\beta F + n}[1 - e^{-(\beta F+n)S}]. \tag{L.2}$$

It describes the absorption coefficient after the excitation of S equally spaced pulses of fluence F. In the absence of relaxation $\tau \to +\infty$, $n = 0$ and we find

$$\alpha(S,F) = \alpha_0 + \Delta\alpha(1 - e^{-\beta FS}) \tag{L.3}$$

where $\Delta\alpha = \alpha_{max} - \alpha_0$.

A similar ansatz to Equation L.1 can be made for the change in specific energy H with the solution

$$H(S,F) = H_0 - \Delta H(1 - e^{-\gamma FS}) \tag{L.4}$$

where H_0 is the energy needed for single pulse exposure, γ is a coefficient for the induced change by a pulse of fluence F, and $\Delta H = H_0 - H_{min}$. H_{min} is the minimum energy needed to reach threshold. Similarly, it is assumed that $n = 0$. Note that both α and γ depend on the radius coordinate r through the fluence $F(r)$.

Let us define the threshold fluence for a burst of pulses as

$$F_{th}(S) = \frac{H(S-1)}{\alpha(S-1)}. \tag{L.5}$$

From the measured $F_{th}(S)$, one can usually determine the single pulse (1-on-1) threshold $F_1 = F_{th}(1) = H_0/\alpha_0$ and the multiple pulse threshold $F_\infty = F_{th}(\infty)$. In terms of these quantities, assuming $n = 0$, we can write Equation L.5 as

$$F_{th}(S) = \frac{F_1 - [F_1 - F_\infty(1 + \frac{\Delta\alpha}{\alpha_0})][1 - e^{-\gamma F(r)(S-1)}]}{1 + \frac{\Delta\alpha}{\alpha_0}[1 - e^{-\beta F(r)(S-1)}]}. \tag{L.6}$$

Using Equation L.6, we can fit the experimental data with the free parameters $\Delta\alpha/\alpha_0$, β and γ.

Appendix M

Absorption and diffraction signal near zero time delay

The measurement near zero delay has contribution from pulse overlap and non-equilibrium electron distributions. It cannot be explained with the Drude model. Figure M.1 shows the absorption near zero time delay (ZTD). Figure x shows the

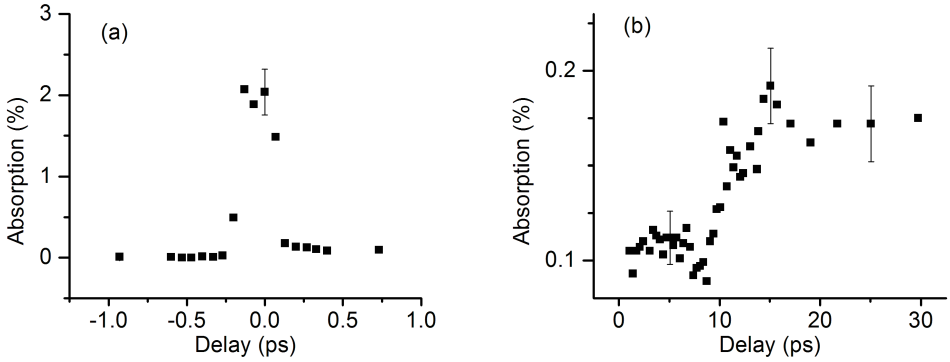

Figure M.1: Measured plasma absorption as a function of the delay near zero time delay (ZTD). (a): Delay from -1 ps to 1 ps. (b): Delay from 1 ps to 30 ps.

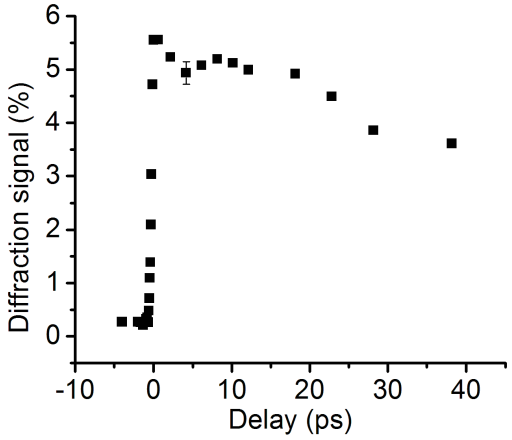

Figure M.2: Measured diffraction signal $|\Delta S|$ as a function of the delay near ZTD. The delay is from -4 ps to 38 ps.

diffraction signal near ZTD. For the modeling, all results are plotted for delays $\tau > 35$ ps to avoid complications in the data interpretation.

Appendix N

Publications

Here is a list of my publications related to the work during my Ph.D. study.

1. Z. Sun, J. Chen, and W. Rudolph, "Determination of the transient electron temperature in a femtosecond-laser-induced air plasma filament," *Physical Review E*, vol. 83, p. 046408, Apr. 2011

2. C. Karras, Z. Sun, D. N. Nguyen, L. A. Emmert, and W. Rudolph, "The impact ionization coefficient in dielectric materials revisited," in *Proc. SPIE*, p. 819028, Oct. 2011

3. W. Rudolph, L. A. Emmert, D. Nguyen, C. Karras, Z. Sun, and R. Weber, "Subpicosecond laser breakdown in optical thin films," in *Proc. SPIE*, vol. 8206, p. 82060D, 2011

4. C. Rodriguez, Z. Sun, Z. Wang, and W. Rudolph, "Characterization of laser-induced air plasmas by third harmonic generation," *Optics Express*, vol. 19, pp. 16115–16125, Aug. 2011

5. C. S. Menoni, P. F. Langston, E. Krous, D. Patel, L. Emmert, A. Markosyan, B. Reagan, K. Wernsing, Y. Xu, Z. Sun, R. Route, M. M. Fejer, J. J. Rocca, and W. Rudolph, "What role do defects play in the laser damage behavior of metal oxides?," in *Proc. SPIE*, vol. 8530, p. 85300J, 2012

6. Z. Sun, A. Mansoori, X. Zhang, L. A. Emmert, D. Patel, C. S. Menoni, and W. Rudolph, "Confocal photothermal microscopy of thin films based on etalon and thermal lensing effects," in *Proc. SPIE*, vol. 8885, p. 88851Y, 2013

7. W. Rudolph, L. Emmert, Z. Sun, D. Patel, and C. Menoni, "Laser damage in dielectric films: What we know and what we don't," in *Proc. SPIE*, vol. 8885, p. 888516, 2013

8. M. Lenzner, Z. Sun, and W. Rudolph, "Determination of multi-pulse damage thresholds from crater size measurements," in *Proc. SPIE*, vol. 9237, p. 923714, 2014

9. Z. Sun, M. Lenzner, and W. Rudolph, "Generic incubation law for laser damage and ablation thresholds," *Journal of Applied Physics*, vol. 117, p. 073102, Feb. 2015

References

[1] M. S. Bruma, "Mechanism for energy transfer between a focused laser beam and a transparent medium involving electromagnetic-field gradients," *Journal of the Optical Society of America*, vol. 54, p. 563, Apr. 1964.

[2] M. Hercher, "Laser-induced damage in transparent media,," *Journal of the Optical Society of America*, vol. 54, p. 563, Apr. 1964.

[3] C. R. Giuliano, "Laser-induced damage to transparent dielectric materials," *Applied Physics Letters*, vol. 5, pp. 137–139, Oct. 1964.

[4] J. H. Cullom and R. W. Waynant, "Determination of laser damage threshold for various glasses," *Applied Optics*, vol. 3, pp. 989–990, Aug. 1964.

[5] M. J. Soileau, W. E. Williams, N. Mansour, and E. W. Van Stryland, "Laser-induced damage and the role of self-focusing," *Optical Engineering*, vol. 28, no. 10, p. 1133, 1989.

[6] S. Backus, C. G. Durfee, M. M. Murnane, and H. C. Kapteyn, "High power ultrafast lasers," *Review of Scientific Instruments*, vol. 69, p. 1207, 1998.

[7] R. Osellame, G. Cerullo, and R. Ramponi, *Femtosecond Laser Micromachining: Photonic and Microfluidic Devices in Transparent Materials*. Springer, Mar. 2012.

[8] K. Sugioka, M. Meunier, and A. Piqu, *Laser Precision Microfabrication*. Springer-Verlag, Aug. 2010.

[9] M. Okoshi, K. Higashikawa, and M. Hanabusa, "Pulsed laser deposition of ZnO thin films using a femtosecond laser," *Applied Surface Science*, vol. 154155, pp. 424–427, Feb. 2000.

[10] E. Millon, O. Albert, J. C. Loulergue, J. Etchepare, D. Hulin, W. Seiler, and J. Perriere, "Growth of heteroepitaxial ZnO thin films by femtosecond pulsed-laser deposition," *Journal of Applied Physics*, vol. 88, pp. 6937–6939, Dec. 2000.

[11] P. Balling and J. Schou, "Femtosecond-laser ablation dynamics of dielectrics: basics and applications for thin films," *Reports on Progress in Physics*, vol. 76, p. 036502, Mar. 2013.

[12] C. J. Stolz, M. D. Thomas, and A. J. Griffin, "BDS thin film damage competition," in *Proc. SPIE*, vol. 7132, p. 71320, 2008.

[13] C. J. Stolz, D. Ristau, M. Turowski, and H. Blaschke, "Thin film femtosecond laser damage competition," in *Proc. SPIE*, vol. 7504, p. 75040, 2009.

[14] C. J. Stolz, M. Caputo, A. J. Griffin, and M. D. Thomas, "BDS thin film UV antireflection laser damage competition," in *Proc. SPIE*, vol. 7842, p. 784206, 2010.

[15] C. J. Stolz, H. Blaschke, L. Jensen, H. Mdebach, and D. Ristau, "Excimer mirror thin film laser damage competition," in *Proc. SPIE*, vol. 8190, p. 819007, 2011.

[16] C. J. Stolz, "Boulder damage symposium annual thin-film laser damage competition," *Optical Engineering*, vol. 51, no. 12, p. 121818, 2012.

[17] C. J. Stolz and J. Runkel, "Brewster angle polarizing beamsplitter laser damage competition: P polarization," in *Proc. SPIE*, vol. 8530, p. 85300, 2012.

[18] C. J. Stolz and J. Runkel, "Brewster angle thin film polarizing beamsplitter laser damage competition: "S" polarization," in *Proc. SPIE*, vol. 8885, p. 888509, 2013.

[19] A. V. Smith and B. T. Do, "Bulk and surface laser damage of silica by picosecond and nanosecond pulses at 1064 nm," *Applied Optics*, vol. 47, no. 26, pp. 4812–4832, 2008.

[20] A. Braun, G. Korn, X. Liu, D. Du, J. Squier, and G. Mourou, "Self-channeling of high-peak-power femtosecond laser pulses in air," *Optics Letters*, vol. 20, no. 1, pp. 73–75, 1995.

[21] L. Bergé, S. Skupin, R. Nuter, J. Kasparian, and J. Wolf, "Ultrashort filaments of light in weakly ionized, optically transparent media," *Reports on Progress in Physics*, vol. 70, pp. 1633–1713, 2007.

[22] A. Couairon and A. Mysyrowicz, "Femtosecond filamentation in transparent media," *Physics Reports*, vol. 441, no. 2-4, pp. 47–189, 2007.

[23] V. P. Kandidov, S. A. Shlenov, and O. G. Kosareva, "Filamentation of high-power femtosecond laser radiation," *Quantum Electronics*, vol. 39, no. 3, pp. 205–228, 2009.

[24] X. M. Zhao, J. Diels, C. Y. Wang, and J. Elizondo, "Femtosecond ultraviolet laser pulse induced lightning discharges in gases," *IEEE Journal of Quantum Electronics*, vol. 31, no. 3, pp. 599–612, 1995.

[25] J. Kasparian, M. Rodriguez, G. Mejean, J. Yu, E. Salmon, H. Wille, R. Bourayou, S. Frey, Y. Andre, A. Mysyrowicz, R. Sauerbrey, J. Wolf, and L. Woste, "White-Light filaments for atmospheric analysis," *Science*, vol. 301, no. 5629, pp. 61–64, 2003.

[26] N. L. Wagner, E. A. Gibson, T. Popmintchev, I. P. Christov, M. M. Murnane, and H. C. Kapteyn, "Self-Compression of ultrashort pulses through Ionization-Induced spatiotemporal reshaping," *Physical Review Letters*, vol. 93, p. 173902, 2004.

[27] A. Couairon, J. Biegert, C. P. Hauri, W. Kornelis, F. W. Helbing, U. Keller, and A. Mysyrowicz, "Self-compression of ultra-short laser pulses down to one optical cycle by filamentation," *Journal of Modern Optics*, vol. 53, pp. 75–85, 2006.

[28] C. Schaffer, A. Brodeur, and E. Mazur, "Laser-induced breakdown and damage in bulk transparent materials induced by tightly focused femtosecond laser pulses," *Measurement Science & Technology*, vol. 12, pp. 1784–1794, NOV 2001.

[29] S. Mao, F. Qur, S. Guizard, X. Mao, R. Russo, G. Petite, and P. Martin, "Dynamics of femtosecond laser interactions with dielectrics," *Applied Physics A*, vol. 79, no. 7, pp. 1695–1709, 2004.

[30] L. V. Keldysh, "Ionization in the field of a strong electromagnetic wave," *Soviet Physics JETP-USSR*, vol. 20, pp. 1307–1314, 1965.

[31] N. Bloembergen, "Laser-induced electric breakdown in solids," *IEEE Journal of Quantum Electronics*, vol. 10, pp. 375– 386, Mar. 1974.

[32] S. C. Jones, P. Braunlich, R. T. Casper, X.-A. Shen, and P. Kelly, "Recent progress on laser-induced modifications and intrinsic bulk damage of wide-gap optical materials," *Optical Engineering*, vol. 28, pp. 1039–1068, Oct. 1989.

[33] M. Mero, J. Liu, W. Rudolph, D. Ristau, and K. Starke, "Scaling laws of femtosecond laser pulse induced breakdown in oxide films," *Physical Review B*, vol. 71, p. 115109, Mar. 2005.

[34] L. A. Emmert, M. Mero, and W. Rudolph, "Modeling the effect of native and laser-induced states on the dielectric breakdown of wide band gap optical materials by multiple subpicosecond laser pulses," *Journal of Applied Physics*, vol. 108, p. 043523, 2010.

[35] M. Lenzner, J. Krüger, S. Sartania, Z. Cheng, C. Spielmann, G. Mourou, W. Kautek, and F. Krausz, "Femtosecond optical breakdown in dielectrics," *Physical Review Letters*, vol. 80, pp. 4076–4079, May 1998.

[36] L. Sudrie, A. Couairon, M. Franco, B. Lamouroux, B. Prade, S. Tzortzakis, and A. Mysyrowicz, "Femtosecond laser-induced damage and filamentary propagation in fused silica," *Physical Review Letters*, vol. 89, p. 186601, Oct. 2002.

[37] A. Q. Wu, I. H. Chowdhury, and X. Xu, "Femtosecond laser absorption in fused silica: Numerical and experimental investigation," *Physical Review B*, vol. 72, p. 085128, Aug. 2005.

[38] P. P. Rajeev, M. Gertsvolf, E. Simova, C. Hnatovsky, R. S. Taylor, V. R. Bhardwaj, D. M. Rayner, and P. B. Corkum, "Memory in nonlinear ionization of transparent solids," *Physical Review Letters*, vol. 97, p. 253001, Dec. 2006.

[39] P. P. Rajeev, M. Gertsvolf, P. B. Corkum, and D. M. Rayner, "Field dependent avalanche ionization rates in dielectrics," *Physical Review Letters*, vol. 102, p. 083001, Feb. 2009.

[40] S. Guizard, N. Fedorov, A. Mouskeftaras, and S. Klimentov, "Femtosecond laser ablation of dielectrics: Experimental studies of fundamental processes," in *AIP Conference Proceedings*, vol. 1278, pp. 336–346, AIP Publishing, Oct. 2010.

[41] C. Karras, Z. Sun, D. N. Nguyen, L. A. Emmert, and W. Rudolph, "The impact ionization coefficient in dielectric materials revisited," in *Proc. SPIE*, p. 819028, Oct. 2011.

[42] V. V. Temnov, K. Sokolowski-Tinten, P. Zhou, A. El-Khamhawy, and D. von der Linde, "Multiphoton ionization in dielectrics: Comparison of circular and linear polarization," *Physical Review Letters*, vol. 97, p. 237403, Dec. 2006.

[43] B. E. Newnam, D. H. Gill, and G. Faulkner, "Influence of standing-wave fields on the laser damage resistance of dielectric films," in *Laser-Induced Damage in Optical Materials*, vol. Spectial Publication 435, (Boulder, Colorado, USA), pp. 254–271, National Bureau of Standards, United States, July 1975.

[44] A. Joglekar, H. Liu, G. Spooner, E. Meyhfer, G. Mourou, and A. Hunt, "A study of the deterministic character of optical damage by femtosecond laser pulses and applications to nanomachining," *Applied Physics B: Lasers and Optics*, vol. 77, pp. 25–30, Aug. 2003.

[45] J. Bonse, J. Krüger, S. Höhm, and A. Rosenfeld, "Femtosecond laser-induced periodic surface structures," *Journal of Laser Applications*, vol. 24, p. 042006, July 2012.

[46] R. Buividas, M. Mikutis, and S. Juodkazis, "Surface and bulk structuring of materials by ripples with long and short laser pulses: Recent advances," *Progress in Quantum Electronics*, vol. 38, pp. 119–156, May 2014.

[47] J. E. Sipe, J. F. Young, J. S. Preston, and H. M. van Driel, "Laser-induced periodic surface structure. i. theory," *Physical Review B*, vol. 27, pp. 1141–1154, Jan. 1983.

[48] J. M. Liu, "Simple technique for measurements of pulsed gaussian-beam spot sizes," *Optics Letters*, vol. 7, pp. 196–198, May 1982.

[49] L. A. Emmert and W. Rudolph, "Femtosecond laser-induced damage in dielectric materials," in *Laser-Induced Damage in Optical Materials* (D. Ristau, ed.), CRC Press, Nov. 2014.

[50] Y. Jee, M. F. Becker, and R. M. Walser, "Laser-induced damage on single-crystal metal surfaces," *Journal of the Optical Society of America B*, vol. 5, no. 3, pp. 648–659, 1988.

[51] D. Ashkenasi, M. Lorenz, R. Stoian, and A. Rosenfeld, "Surface damage threshold and structuring of dielectrics using femtosecond laser pulses: the role of incubation," *Applied Surface Science*, vol. 150, pp. 101–106, 1999.

[52] M. Mero, B. Clapp, J. Jasapara, W. Rudolph, D. Ristau, K. Starke, J. Krüger, S. Martin, and W. Kautek, "On the damage behavior of dielectric films when illuminated with multiple femtosecond laser pulses," *Optical Engineering*, vol. 44, p. 051107, 2005.

[53] M. Chateauneuf, S. Payeur, J. Dubois, and J. Kieffer, "Microwave guiding in air by a cylindrical filament array waveguide," *Applied Physics Letters*, vol. 92, Mar. 2008.

[54] J. Yu, D. Mondelain, G. Ange, R. Volk, S. Niedermeier, J. P. Wolf, J. Kasparian, and R. Sauerbrey, "Backward supercontinuum emission from a filament generated by ultrashort laser pulses in air," *Optics Letters*, vol. 26, pp. 533–535, Apr. 2001.

[55] S. Tzortzakis, B. Prade, M. Franco, and A. Mysyrowicz, "Time-evolution of the plasma channel at the trail of a self-guided IR femtosecond laser pulse in air," *Optics Communications*, vol. 181, pp. 123–127, July 2000.

[56] J. Jasapara, A. V. V. Nampoothiri, W. Rudolph, D. Ristau, and K. Starke, "Femtosecond laser pulse induced breakdown in dielectric thin films," *Physical Review B*, vol. 63, p. 045117, Jan. 2001.

[57] P. F. Moulton, "Spectroscopic and laser characteristics of Ti:Al_2O_3," *Journal of the Optical Society of America B*, vol. 3, pp. 125–133, Jan. 1986.

[58] H. Enqvist, "A setup for efficient frequency tripling of high-power femtosecond laser pulses," Master's thesis, Lund University, Oct. 2004.

[59] Y. Q. Liu, J. Zhang, W. X. Liang, and Z. H. Wang, "Theoretical and experimental studies on third harmonic generation of femtosecond ti:sapphire laser," *Acta Physica Sinica*, vol. 54, no. 4, pp. 1593–1598, 2005.

[60] J. Vetterlein, "Pump & probe controller users manual," tech. rep., The University of New Mexico, Albuquerque, New Mexico (USA), Sept. 2010.

[61] R. Trebino, K. W. DeLong, D. N. Fittinghoff, J. N. Sweetser, M. A. Krumbügel, B. A. Richman, and D. J. Kane, "Measuring ultrashort laser pulses in the time-frequency domain using frequency-resolved optical gating," *Review of Scientific Instruments*, vol. 68, pp. 3277–3295, Sept. 1997.

[62] G. Veshapidze, M. L. Trachy, M. H. Shah, and B. D. DePaola, "Reducing the uncertainty in laser beam size measurement with a scanning edge method," *Applied Optics*, vol. 45, pp. 8197–8199, Nov. 2006.

[63] W. Rudolph, L. Emmert, Z. Sun, D. Patel, and C. Menoni, "Laser damage in dielectric films: What we know and what we don't," in *Proc. SPIE*, vol. 8885, p. 888516, 2013.

[64] D. N. Nguyen, L. A. Emmert, D. Patel, C. S. Menoni, and W. Rudolph, "Transient phenomena in the dielectric breakdown of HfO2 optical films probed by ultrafast laser pulse pairs," *Applied Physics Letters*, vol. 97, p. 191909, 2010.

[65] S. Klarsfeld and A. Maquet, "Circular versus linear polarization in multiphoton ionization," *Physical Review Letters*, vol. 29, pp. 79–81, July 1972.

[66] H. R. Reiss, "Polarization effects in high-order multiphoton ionization," *Physical Review Letters*, vol. 29, pp. 1129–1131, Oct. 1972.

[67] R. A. Fox, R. M. Kogan, and E. J. Robinson, "Laser triple-quantum photoionization of cesium," *Physical Review Letters*, vol. 26, pp. 1416–1417, June 1971.

[68] H. S. Carman and R. N. Compton, "High-order multiphoton ionization photoelectron spectroscopy of nitric oxide," *The Journal of Chemical Physics*, vol. 90, pp. 1307–1312, Feb. 1989.

[69] D. D. Venable and R. B. Kay, "Polarization effects in four-photon conductivity in quartz," *Applied Physics Letters*, vol. 27, pp. 48–49, July 1975.

[70] D. Grosso and P. A. Sermon, "Scandia optical coatings for application at 351 nm," *Thin Solid Films*, vol. 368, pp. 116–124, June 2000.

[71] E. M. Krous, *Characterization of scandium oxide thin films for use in interference coatings for high-power lasers operating in the near-infrared*. PhD thesis, Colorado State University, Fort Collins, Colorado, July 2010.

[72] A. A. Fridman and L. A. Kennedy, *Plasma physics and engineering*. Taylor & Francis, 2004.

[73] A. S. Foster, F. Lopez Gejo, A. L. Shluger, and R. M. Nieminen, "Vacancy and interstitial defects in hafnia," *Physical Review B*, vol. 65, p. 174117, May 2002.

[74] B. Langdon, D. Patel, E. Krous, P. Langston, C. S. Menoni, and M. Shinn, "Electron spin resonance spectroscopy investigation of ion beam sputtered HfO2 and SiO2 thin films," in *Proc. SPIE*, vol. 7132, p. 71320M, 2008.

[75] R. D. Doherty, D. A. Hughes, F. J. Humphreys, J. J. Jonas, D. J. Jensen, M. E. Kassner, W. E. King, T. R. McNelley, H. J. McQueen, and A. D. Rollett, "Current issues in recrystallization: a review," *Materials Science and Engineering: A*, vol. 238, pp. 219–274, Nov. 1997.

[76] D. Muñoz Ramo, A. L. Shluger, J. L. Gavartin, and G. Bersuker, "Theoretical prediction of intrinsic self-trapping of electrons and holes in monoclinic HfO2," *Physical Review Letters*, vol. 99, p. 155504, Oct. 2007.

[77] A. Shluger, M. Georgiev, and N. Itoh, "Self-trapped excitons and interstitial-vacancy pairs in oxides," *Philosophical Magazine Part B*, vol. 63, pp. 955–964, Apr. 1991.

[78] X. Luo, *Structural phase transitions in hafnia and zirconia at ambient pressure*. PhD thesis, University of Texas at Austin, Aug. 2010.

[79] P. Audebert, P. Daguzan, A. Dos Santos, J. C. Gauthier, J. P. Geindre, S. Guizard, G. Hamoniaux, K. Krastev, P. Martin, G. Petite, and A. Antonetti, "Space-time observation of an electron gas in SiO_{2}," *Physical Review Letters*, vol. 73, p. 1990, Oct. 1994.

[80] W. Rudolph, L. A. Emmert, D. Nguyen, C. Karras, Z. Sun, and R. Weber, "Subpicosecond laser breakdown in optical thin films," in *Proc. SPIE*, vol. 8206, p. 82060D, 2011.

[81] C. S. Menoni, P. F. Langston, E. Krous, D. Patel, L. Emmert, A. Markosyan, B. Reagan, K. Wernsing, Y. Xu, Z. Sun, R. Route, M. M. Fejer, J. J. Rocca, and W. Rudolph, "What role do defects play in the laser damage behavior of metal oxides?," in *Proc. SPIE*, vol. 8530, p. 85300J, 2012.

[82] A. V. Smith and B. T. Do, "Picosecond-nanosecond bulk damage of fused silica at 1064nm," in *Proc. SPIE*, vol. 7132, p. 71321E, 2008.

[83] J. Jasapara, M. Mero, and W. Rudolph, "Retrieval of the dielectric function of thin films from femtosecond pump-probe experiments," *Applied Physics Letters*, vol. 80, pp. 2637–2639, Apr. 2002.

[84] M. Mero, A. J. Sabbah, J. Zeller, and W. Rudolph, "Femtosecond dynamics of dielectric films in the pre-ablation regime," *Applied Physics A*, vol. 81, pp. 317–324, July 2005.

[85] A. Mouskeftaras, S. Guizard, N. Fedorov, and S. Klimentov, "Mechanisms of femtosecond laser ablation of dielectrics revealed by double pumpprobe experiment," *Applied Physics A*, vol. 110, pp. 709–715, Mar. 2013.

[86] L. Englert, B. Rethfeld, L. Haag, M. Wollenhaupt, C. Sarpe-Tudoran, and T. Baumert, "Control of ionization processes in high band gap materials via tailored femtosecond pulses," *Optics Express*, vol. 15, pp. 17855–17862, Dec. 2007.

[87] I. N. Zavestovskaya, P. G. Eliseev, O. N. Krokhin, and N. A. Menkova, "Analysis of the nonlinear absorption mechanisms in ablation of transparent materials by high-intensity and ultrashort laser pulses," *Applied Physics A*, vol. 92, pp. 903–906, Sept. 2008.

[88] B. Chimier, O. Utéza, N. Sanner, M. Sentis, T. Itina, P. Lassonde, F. Légaré, F. Vidal, and J. C. Kieffer, "Damage and ablation thresholds of fused-silica in femtosecond regime," *Physical Review B*, vol. 84, p. 094104, Sept. 2011.

[89] M. Li, S. Menon, J. P. Nibarger, and G. N. Gibson, "Ultrafast electron dynamics in femtosecond optical breakdown of dielectrics," *Physical Review Letters*, vol. 82, pp. 2394–2397, Mar. 1999.

[90] B. C. Stuart, M. D. Feit, S. Herman, A. M. Rubenchik, B. W. Shore, and M. D. Perry, "Nanosecond-to-femtosecond laser-induced breakdown in dielectrics," *Physical Review B*, vol. 53, pp. 1749–1761, Jan. 1996.

[91] G. Dresselhaus and M. S. Dresselhaus, *The Optical Properties of Solids edited by J. Tauc.* New York: Academic Press, 1966.

[92] R. Parzyński, "Effect of light polarization on multi-photon ionization of the one-electron atom," *Optics Communications*, vol. 8, pp. 79–81, May 1973.

[93] E. L. Ivchenko and E. Y. Perlin *Soviet Physics-Solid State*, vol. 15, p. 1850, 1974.

[94] P.-J. Wang and F. He, "Multiphoton ionization of the hydrogen atom exposed to circularly or linearly polarized laser pulses," *Chinese Physics B*, vol. 18, pp. 5291–5295, Dec. 2009.

[95] S. Höhm, A. Rosenfeld, J. Krüger, and J. Bonse, "Femtosecond laser-induced periodic surface structures on silica," *Journal of Applied Physics*, vol. 112, p. 014901, July 2012.

[96] H. Lee, "Picosecond mid-IR laser induced surface damage on gallium phosphate (GaP) and calcium fluoride(CaF_2," *Journal of Mechanical Science and Technology*, vol. 21, pp. 1077–1082, July 2007.

[97] M. S. Trtica, B. M. Gakovic, B. B. Radak, D. Batani, T. Desai, and M. Bussoli, "Periodic surface structures on crystalline silicon created by 532nm picosecond nd:YAG laser pulses," *Applied Surface Science*, vol. 254, pp. 1377–1381, Dec. 2007.

[98] J. Eichstädt, G. R. B. E. Römer, and A. J. Huis in t Veld, "Determination of irradiation parameters for laser-induced periodic surface structures," *Applied Surface Science*, vol. 264, pp. 79–87, Jan. 2013.

[99] E. Rebollar, S. Pérez, J. J. Hernández, I. Martín-Fabiani, D. R. Rueda, T. A. Ezquerra, and M. Castillejo, "Assessment and formation mechanism of laser-induced periodic surface structures on polymer spin-coated films in real and reciprocal space," *Langmuir*, vol. 27, pp. 5596–5606, May 2011.

[100] J. Bonse, M. Munz, and H. Sturm, "Structure formation on the surface of indium phosphide irradiated by femtosecond laser pulses," *Journal of Applied Physics*, vol. 97, p. 013538, Dec. 2004.

[101] J. Bonse, A. Rosenfeld, and J. Krüger, "On the role of surface plasmon polaritons in the formation of laser-induced periodic surface structures upon irradiation of silicon by femtosecond-laser pulses," *Journal of Applied Physics*, vol. 106, no. 10, p. 104910, 2009.

[102] J. Bonse and J. Krüger, "Pulse number dependence of laser-induced periodic surface structures for femtosecond laser irradiation of silicon," *Journal of Applied Physics*, vol. 108, p. 034903, Aug. 2010.

[103] M. Zamfirescu, M. Ulmeanu, F. Jipa, O. Cretu, A. Moldovan, G. Epurescu, M. Dinescu, and R. Dabu, "Femtosecond laser induced periodic surface structures on ZnO thin films," *Journal of Laser Micro/ Nanoengineering*, vol. 4, no. 1, pp. 7–10, 2009.

[104] M. Zamfirescu, A. Dinescu, M. Danila, G. Socol, and C. Radu, "The role of the substrate material type in formation of laser induced periodical surface structures on ZnO thin films," *Applied Surface Science*, vol. 258, pp. 9385–9388, Sept. 2012.

[105] Y. Dai, M. He, H. Bian, B. Lu, X. Yan, and G. Ma, "Femtosecond laser nanostructuring of silver film," *Applied Physics A: Materials Science & Processing*, vol. 106, pp. 567–574, Mar. 2012.

[106] N. Wu, Z. Wang, X. Wang, Y. Shimotsuma, M. Nishi, K. Miura, and K. Hirao, "Nano-periodic structure formation on titanium thin film with a femtosecond laser," *Journal of the Ceramic Society of Japan*, vol. 119, no. 1395, pp. 898–901, 2011.

[107] F. Garrelie, J.-P. Colombier, F. Pigeon, S. Tonchev, N. Faure, M. Bounhalli, S. Reynaud, and O. Parriaux, "Evidence of surface plasmon resonance in ultrafast laser-induced ripples," *Optics Express*, vol. 19, pp. 9035–9043, May 2011.

[108] M. Afshar, M. Straub, H. Voellm, D. Feili, K. Koenig, and H. Seidel, "Sub-100 nm structuring of indium-tin-oxide thin films by sub-15 femtosecond pulsed near-infrared laser light," *Optics Letters*, vol. 37, pp. 563–565, Feb. 2012.

[109] B. Gakovic, C. Radu, M. Zamfirescu, B. Radak, M. Trtica, S. Petrovic, P. Panjan, F. Zupanic, C. Ristoscu, and I. N. Mihailescu, "Femtosecond laser modification of multilayered TiAlN/TiN coating," *Surface and Coatings Technology*, vol. 206, pp. 411–416, Oct. 2011.

[110] G. Miyaji and K. Miyazaki, "Origin of periodicity in nanostructuring on thin film surfaces ablated with femtosecond laser pulses," *Optics Express*, vol. 16, p. 16265, Sept. 2008.

[111] C. W. Luo, W. T. Tang, H. I. Wang, L. W. Liao, H. P. Lo, K. H. Wu, J.-Y. Lin, J. Y. Juang, T. M. Uen, and T. Kobayashi, "Controllable subwavelength-ripple and -dot structures on $YBa_2Cu_3O_7$ induced by ultrashort laser pulses," *Superconductor Science and Technology*, vol. 25, p. 115008, Nov. 2012.

[112] J. Yang, R. Wang, W. Liu, Y. Sun, and X. Zhu, "Investigation of microstructuring $CuInGaSe_2$ thin films with ultrashort laser pulses," *Journal of Physics D: Applied Physics*, vol. 42, p. 215305, Nov. 2009.

[113] U. Chakravarty, R. A. Ganeev, P. A. Naik, J. A. Chakera, M. Babu, and P. Gupta, "Nano-ripple formation on different band-gap semiconductor surfaces using femtosecond pulses," *Journal of Applied Physics*, vol. 109, no. 8, p. 084347, 2011.

[114] Q.-Z. Zhao, S. Malzer, and L.-J. Wang, "Self-organized tungsten nanospikes grown on subwavelength ripples induced by femtosecond laser pulses," *Optics Express*, vol. 15, pp. 15741–15746, Nov. 2007.

[115] Q. Z. Zhao, S. Malzer, and L. J. Wang, "Formation of subwavelength periodic structures on tungsten induced by ultrashort laser pulses," *Optics Letters*, vol. 32, pp. 1932–1934, July 2007.

[116] G. D. Tsibidis, M. Barberoglou, P. A. Loukakos, E. Stratakis, and C. Fotakis, "Dynamics of ripple formation on silicon surfaces by ultrashort laser pulses in subablation conditions," *Physical Review B*, vol. 86, p. 115316, Sept. 2012.

[117] Z. Sun, A. Mansoori, X. Zhang, L. A. Emmert, D. Patel, C. S. Menoni, and W. Rudolph, "Confocal photothermal microscopy of thin films based on etalon and thermal lensing effects," in *Proc. SPIE*, vol. 8885, p. 88851Y, 2013.

[118] M. D. Shirk and P. A. Molian, "A review of ultrashort pulsed laser ablation of materials," *Journal of Laser Applications*, vol. 10, pp. 18–28, Feb. 1998.

[119] K. Sugioka and Y. Cheng, "Ultrafast lasersreliable tools for advanced materials processing," *Light: Science & Applications*, vol. 3, p. e149, Apr. 2014.

[120] A. A. Manenkov, "Fundamental mechanisms of laser-induced damage in optical materials: today's state of understanding and problems," *Optical Engineering*, vol. 53, p. 010901, JAN 2014.

[121] N. Sanner, O. Utza, B. Bussiere, G. Coustillier, A. Leray, T. Itina, and M. Sentis, "Measurement of femtosecond laser-induced damage and ablation thresholds in dielectrics," *Applied Physics A*, vol. 94, pp. 889–897, Mar. 2009.

[122] S. Nolte, C. Momma, H. Jacobs, A. Tünnermann, B. N. Chichkov, B. Wellegehausen, and H. Welling, "Ablation of metals by ultrashort laser pulses," *Journal of the Optical Society of America B*, vol. 14, pp. 2716–2722, Oct. 1997.

[123] J. K. Chen, D. Y. Tzou, and J. E. Beraun, "Numerical investigation of ultrashort laser damage in semiconductors," *International Journal of Heat and Mass Transfer*, vol. 48, pp. 501–509, Jan. 2005.

[124] C. W. Carr, H. B. Radousky, and S. G. Demos, "Wavelength dependence of laser-induced damage: Determining the damage initiation mechanisms," *Physical Review Letters*, vol. 91, p. 127402, Sept. 2003.

[125] B. N. Chichkov, C. Momma, S. Nolte, F. v. Alvensleben, and A. Tünnermann, "Femtosecond, picosecond and nanosecond laser ablation of solids," *Applied Physics A*, vol. 63, pp. 109–115, Aug. 1996.

[126] E. G. Gamaly, A. V. Rode, B. Luther-Davies, and V. T. Tikhonchuk, "Ablation of solids by femtosecond lasers: Ablation mechanism and ablation thresholds for metals and dielectrics," *Physics of Plasmas*, vol. 9, pp. 949–957, Mar. 2002.

[127] J. Bonse, P. Rudolph, J. Krüger, S. Baudach, and W. Kautek, "Femtosecond pulse laser processing of tin on silicon," *Applied Surface Science*, vol. 154-155, p. 659663, 2000.

[128] F. Costache, S. Eckert, and J. Reif, "Near-damage threshold femtosecond laser irradiation of dielectric surfaces: desorbed ion kinetics and defect dynamics," *Applied Physics A*, vol. 92, p. 897902, 2008.

[129] L. M. Machado, R. E. Samad, W. de Rossi, and N. D. V. Jr., "D-scan measurement of ablation threshold incubation effects for ultrashort laser pulses," *Optics Express*, vol. 20, p. 4114, 2012.

[130] D. Gómez and I. Goenaga, "On the incubation effect on two thermoplastics when irradiated with ultrashort laser pulses: Broadening effects when machining microchannels," *Applied Surface Science*, vol. 253, p. 22302236, 2006.

[131] B. Neuenschwander, B. Jaeggi, M. Schmid, A. Dommann, A. Neels, T. Bandi, and G. Hennig, "Factors controlling the incubation in the application of ps laser pulses on copper and iron surfaces," in *Laser Applications in Microelectronic and Optoelectronic Manufacturing (LAMOM) XVIII* (X. Xu, G. Hennig, Y. Nakata, and S. W. Roth, eds.), vol. 8607 of *Proc. of SPIE*, p. 86070D, 2013.

[132] G. Raciukaitis, M. Brikas, P. Gecys, and M. Gedvilas, "Accumulation effects in laser ablation of metals with high-repetition-rate lasers," in *High Power Laser Ablation VII* (C. R. Phipps, ed.), vol. 7005 of *Proc. of SPIE*, p. 70052L, 2008.

[133] P. Mannion, J. Magee, E. Coyne, G. O'Connor, and T. Glynn, "The effect of damage accumulation behaviour on ablation thresholds and damage morphology in ultrafast laser micro-machining of common metals in air," *Applied Surface Science*, vol. 233, p. 275287, 2004.

[134] S. Baudach, J. Bonse, J. Krüger, and W. Kautek, "Ultrashort pulse laser ablation of polycarbonate and polymethylmethacrylate," *Applied Surface Science*, vol. 154-155, pp. 555–560, 2000.

[135] M. Lenzner, Z. Sun, and W. Rudolph, "Determination of multi-pulse damage thresholds from crater size measurements," in *Proc. SPIE*, vol. 9237, p. 923714, 2014.

[136] Z. Sun, M. Lenzner, and W. Rudolph, "Generic incubation law for laser damage and ablation thresholds," *Journal of Applied Physics*, vol. 117, p. 073102, Feb. 2015.

[137] B. S. Luk'yanchuk and V. Zafiropulos, "Model for discoloration effect in pigments in laser cleaning of artworks by laser ablation," in *Proc. SPIE*, vol. 4426, pp. 326–333, 2002.

[138] K. Pallav, I. Saxena, and K. F. Ehmann, "Comparative assessment of the laser-induced plasma micromachining and the ultrashort pulsed laser ablation processes," *Journal of Micro and Nano-Manufacturing*, vol. 2, p. 031001, July 2014.

[139] C. B. Li, T. Q. Jia, H. Y. Sun, X. X. Li, S. Z. Xu, D. H. Feng, X. F. Wang, X. C. Ge, and Z. Z. Xu, "Theoretical and experimental study on femtosecond laser-induced damage in MgF_2 crystals," in *Proc. SPIE* (Y. C. Chen, D. Fan, C. Gao, and S. Zhou, eds.), vol. 6028, p. 60281L, Dec. 2005.

[140] S. Babu, "Surface roughness dependence of laser induced damage threshold," *IEEE Journal of Quantum Electronics*, vol. 15, pp. 533–535, July 1979.

[141] M. Grehn, T. Seuthe, M. Hfner, N. Griga, C. Theiss, A. Mermillod-Blondin, M. Eberstein, H. Eichler, and J. Bonse, "Femtosecond-laser induced ablation of silicate glasses and the intrinsic dissociation energy," *Optical Materials Express*, vol. 4, pp. 689–700, Apr. 2014.

[142] K.-H. Sun and M. L. Huggins, "Energy additivity in oxygen-containing crystals and glasses.," *The Journal of Physical and Colloid Chemistry*, vol. 51, pp. 438–443, Feb. 1947.

[143] F. Di Niso, C. Gaudiuso, T. Sibillano, F. P. Mezzapesa, A. Ancona, and P. M. Lugarà, "Role of heat accumulation on the incubation effect in multi-shot laser ablation of stainless steel at high repetition rates," *Optics Express*, vol. 22, no. 17, pp. 12200–12210, 2014.

[144] E. T. J. Nibbering, P. F. Curley, G. Grillon, B. S. Prade, M. A. Franco, F. Salin, and A. Mysyrowicz, "Conical emission from self-guided femtosecond pulses in air," *Optics Letters*, vol. 21, pp. 62–64, Jan. 1996.

[145] B. La Fontaine, F. Vidal, Z. Jiang, C. Y. Chien, D. Comtois, A. Desparois, T. W. Johnston, J.-C. Kieffer, H. Pépin, and H. P. Mercure, "Filamentation of ultrashort pulse laser beams resulting from their propagation over long distances in air," *Physics of Plasmas*, vol. 6, pp. 1615–1621, May 1999.

[146] G. Méchain, A. Couairon, Y.-B. André, C. DAmico, M. Franco, B. Prade, S. Tzortzakis, A. Mysyrowicz, and R. Sauerbrey, "Long-range self-channeling of infrared laser pulses in air: a new propagation regime without ionization," *Applied Physics B*, vol. 79, pp. 379–382, June 2004.

[147] G. Méchain, C. DAmico, Y. B. André, S. Tzortzakis, M. Franco, B. Prade, A. Mysyrowicz, A. Couairon, E. Salmon, and R. Sauerbrey, "Range of plasma filaments created in air by a multi-terawatt femtosecond laser," *Optics Communications*, vol. 247, pp. 171–180, Mar. 2005.

[148] X. M. Zhao, J. Diels, C. Y. Wang, and J. Elizondo, "Femtosecond ultraviolet laser pulse induced lightning discharges in gases," *IEEE Journal of Quantum Electronics*, vol. 31, no. 3, pp. 599–612, 1995.

[149] R. R. Musin, M. N. Shneider, A. M. Zheltikov, and R. B. Miles, "Guiding radar signals by arrays of laser-induced filaments: finite-difference analysis," *Applied Optics*, vol. 46, no. 23, pp. 5593–5597, 2007.

[150] A. E. Dormidonov, V. V. Valuev, V. L. Dmitriev, S. A. Shlenov, and V. P. Kandidov, "Laser filament induced microwave waveguide in air," in *Proc. SPIE*, (Minsk, Belarus), p. 67332S, 2007.

[151] V. Valuev, A. Dormidonov, V. Kandidov, S. Shlenov, V. Kornienko, and V. Cherepenin, "Plasma channels formed by a set of filaments as a guiding system for microwave radiation," *Journal of Communications Technology and Electronics*, vol. 55, pp. 208–214, Feb. 2010.

[152] H. Schillinger and R. Sauerbrey, "Electrical conductivity of long plasma channels in air generated by self-guided femtosecond laser pulses," *Applied Physics B: Lasers and Optics*, vol. 68, no. 4, pp. 753–756, 1999.

[153] H. Yang, J. Zhang, Y. Li, J. Zhang, Y. Li, Z. Chen, H. Teng, Z. Wei, and Z. Sheng, "Characteristics of self-guided laser plasma channels generated by femtosecond laser pulses in air," *Physical Review E*, vol. 66, no. 1, p. 016406, 2002.

[154] F. Théberge, W. Liu, P. T. Simard, A. Becker, and S. L. Chin, "Plasma density inside a femtosecond laser filament in air: Strong dependence on external focusing," *Physical Review E*, vol. 74, no. 3, pp. 036406–7, 2006.

[155] A. Ting, I. Alexeev, D. Gordon, R. Fischer, D. Kaganovich, T. Jones, E. Briscoe, J. Penano, R. Hubbard, and P. Sprangle, "Measurements of intense femtosecond laser pulse propagation in air," *Physics of Plasmas*, vol. 12, no. 5, p. 056705, 2005.

[156] J. Liu, Z. Duan, Z. Zeng, X. Xie, Y. Deng, R. Li, Z. Xu, and S. L. Chin, "Time-resolved investigation of low-density plasma channels produced by a kilohertz femtosecond laser in air," *Physical Review E*, vol. 72, no. 2, p. 026412, 2005.

[157] G. Rodriguez, A. R. Valenzuela, B. Yellampalle, M. J. Schmitt, and K. Kim, "In-line holographic imaging and electron density extraction of ultrafast ionized air filaments," *Journal of the Optical Society of America B*, vol. 25, no. 12, pp. 1988–1997, 2008.

[158] C. Rodriguez, Z. Sun, Z. Wang, and W. Rudolph, "Characterization of laser-induced air plasmas by third harmonic generation," *Optics Express*, vol. 19, pp. 16115–16125, Aug. 2011.

[159] W. Liu, J. Bernhardt, F. Théberge, S. L. Chin, M. Chateauneuf, and J. Dubois, "Spectroscopic characterization of femtosecond laser filament in argon gas," *Journal of Applied Physics*, vol. 102, no. 3, pp. 033111–4, 2007.

[160] J. Bernhardt, W. Liu, F. Théberge, H. Xu, J. Daigle, M. Chteauneuf, J. Dubois, and S. Chin, "Spectroscopic analysis of femtosecond laser plasma filament in air," *Optics Communications*, vol. 281, no. 5, pp. 1268–1274, 2008.

[161] F. Vidal, D. Comtois, C. Chien, A. Desparois, B. L. Fontaine, T. Johnston, J. Kieffer, H. Mercure, H. Pepin, and F. Rizk, "Modeling the triggering of streamers in air by ultrashort laser pulses," *IEEE Transactions on Plasma Science*, vol. 28, no. 2, pp. 418–433, 2000.

[162] Z. Sun, J. Chen, and W. Rudolph, "Determination of the transient electron temperature in a femtosecond-laser-induced air plasma filament," *Physical Review E*, vol. 83, p. 046408, Apr. 2011.

[163] S. Varma, Y. Chen, and H. M. Milchberg, "Trapping and destruction of Long-Range High-Intensity optical filaments by molecular quantum wakes in air," *Physical Review Letters*, vol. 101, no. 20, p. 205001, 2008.

[164] R. W. Lewis, P. Nithiarasu, and K. N. Seetharamu, *Fundamentals of the finite element method for heat and fluid flow*. John Wiley and Sons, 2004.

[165] J. D. Huba, *2009 NRL plasma formulary*. Washington, DC, 2009.

[166] C. Guo, M. Li, J. P. Nibarger, and G. N. Gibson, "Single and double ionization of diatomic molecules in strong laser fields," *Physical Review A*, vol. 58, no. 6, p. R4271, 1998.

[167] J. Kasparian, R. Sauerbrey, and S. Chin, "The critical laser intensity of self-guided light filaments in air," *Applied Physics B*, vol. 71, no. 6, pp. 877–879, 2000.

[168] P. M. Mul and J. W. McGowan, "Merged electron-ion beam experiments. III. temperature dependence of dissociative recombination for atmospheric ions NO^+, O_2^+ and N_2^+," *Journal of Physics B*, vol. 12, no. 9, pp. 1591–1601, 1979.

[169] M. Capitelli, *Plasma kinetics in atmospheric gases*. Springer, 2000.

[170] G. D. Billing and E. R. Fisher, "VV and VT rate coefficients in N_2 by a quantum-classical model," *Chemical Physics*, vol. 43, no. 3, pp. 395–401, 1979.

[171] I. E. Zabelinskii, O. E. Krivonosova, and O. V. Shatalov, "Vibrational excitation of molecular oxygen in collisions O_2-O_2," *Chemical Physics*, vol. 4, pp. 42–45, 1985.

[172] B. Wolf, *Handbook of ion sources*. CRC Press, 1995.

[173] C. Weitkamp, *Lidar: Range-Resolved Optical Remote Sensing of the Atmosphere*. Springer Science & Business Media, July 2005.

[174] F. Calegari, C. Vozzi, S. Gasilov, E. Benedetti, G. Sansone, M. Nisoli, S. De Silvestri, and S. Stagira, "Rotational raman effects in the wake of optical filamentation," *Physical Review Letters*, vol. 100, p. 123006, Mar. 2008.

[175] F. Calegari, C. Vozzi, and S. Stagira, "Optical propagation in molecular gases undergoing filamentation-assisted field-free alignment," *Physical Review A*, vol. 79, p. 023827, Feb. 2009.

[176] A. Schwarz and W. Rudolph, "Dispersion-compensating beam shaper for femtosecond optical vortex beams," *Optics Letters*, vol. 33, pp. 2970–2972, Dec. 2008.

[177] L. T. Vuong, T. D. Grow, A. Ishaaya, A. L. Gaeta, G. W. 'tnbspHooft, E. R. Eliel, and G. Fibich, "Collapse of optical vortices," *Physical Review Letters*, vol. 96, p. 133901, Apr. 2006.

[178] T. D. Grow, A. A. Ishaaya, L. T. Vuong, and A. L. Gaeta, "Collapse and stability of necklace beams in kerr media," *Physical Review Letters*, vol. 99, no. 13, p. 133902, 2007.

[179] H. Cai, J. Wu, P. Lu, X. Bai, L. Ding, and H. Zeng, "Attraction and repulsion of parallel femtosecond filaments in air," *Physical Review A*, vol. 80, p. 051802, Nov. 2009.

[180] Y. P. Deng, J. B. Zhu, Z. G. Ji, J. S. Liu, B. Shuai, R. X. Li, Z. Z. Xu, F. Théberge, and S. L. Chin, "Transverse evolution of a plasma channel in air induced by a femtosecond laser," *Optics Letters*, vol. 31, pp. 546–548, Feb. 2006.

[181] J.-C. Diels and W. Rudolph, *Ultrashort laser pulse phenomena*. Academic Press, 2006.

[182] P. F. Langston, E. Krous, D. Schiltz, D. Patel, L. Emmert, A. Markosyan, B. Reagan, K. Wernsing, Y. Xu, Z. Sun, R. Route, M. M. Fejer, J. J. Rocca, W. Rudolph, and C. S. Menoni, "Point defects in Sc_2O_3 thin films by ion beam sputtering," *Applied Optics*, vol. 53, pp. A276–A280, Feb. 2014.

[183] X. Zhang, L. A. Emmert, and W. Rudolph, "Time-dependent absorption of TiO_2 optical thin films under pulsed and continuous wave 790nm laser irradiation," *Applied Optics*, vol. 52, pp. 8245–8251, Dec. 2013.

[184] M. Mero, *Femtosecond laser induced electron-lattice dynamics and breakdown in dielectric oxide films*. PhD thesis, The University of New Mexico, Albuquerque, New Mexico (USA), July 2005.

[185] F. Keilmann and Y. H. Bai, "Periodic surface structures frozen into CO_2 laser-melted quartz," *Applied Physics A*, vol. 29, pp. 9–18, Sept. 1982.